UiO : Department of Chemistry
University of Oslo

Extrapolating the Electric Dipole Moment

Improving the Resolution of Absorption Spectra from Real-Time Time Dependent Coupled Cluster Theory

Eirill Hauge

Thesis submitted for the degree of Master of Science in Computational Chemistry, Autumn 2021

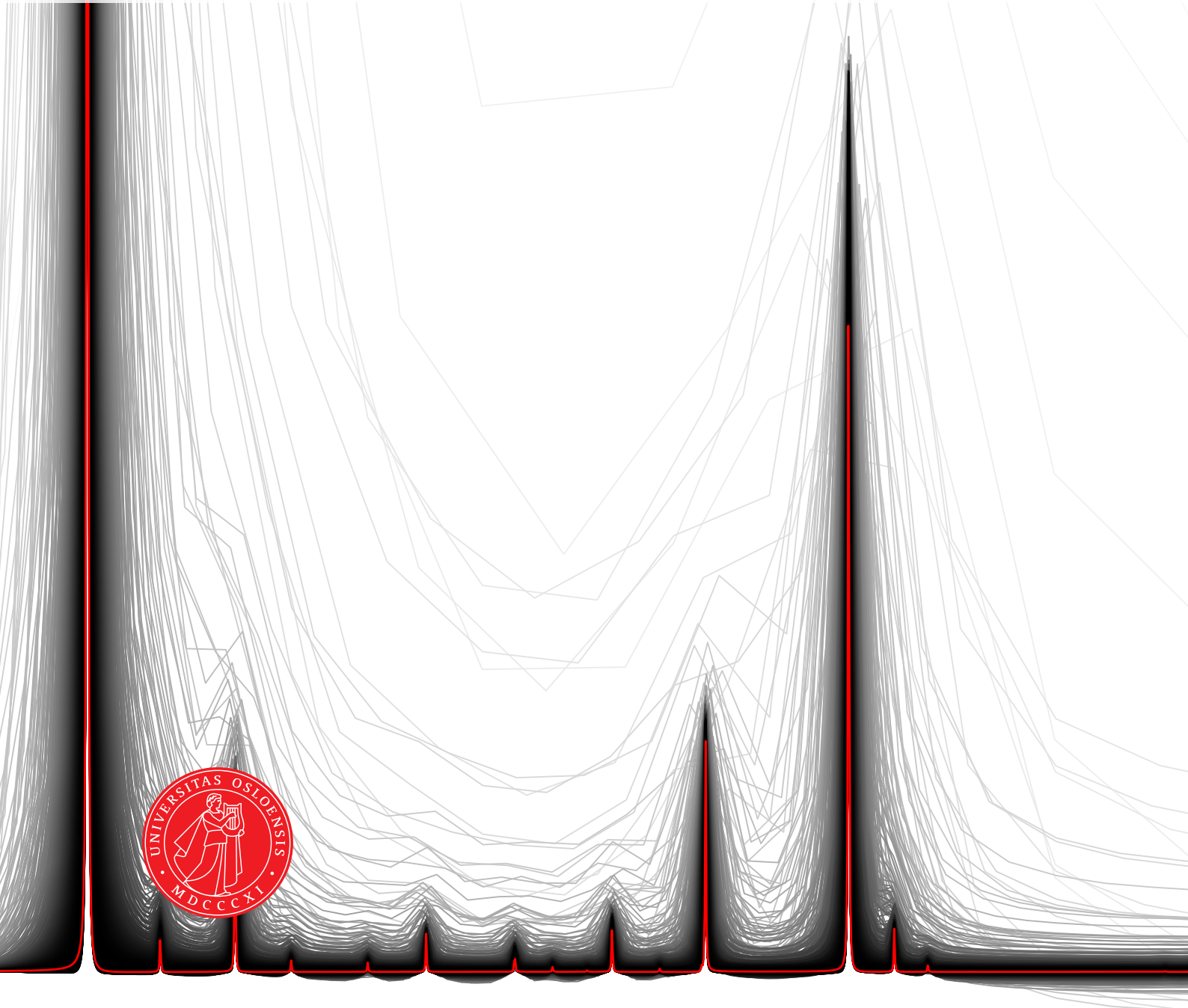

This master's thesis is submitted under the master's programme *Computational Science*, with programme option *Chemistry*, at the Department of Chemistry, University of Oslo. The scope of the thesis is 60 credits.

Abstract

This master project presents a fitting model developed to extrapolate the electric dipole moment obtained from real-time time-dependent molecular electronic structure simulations. Exact quantum theory shows that the dipole moment evolves like a multi-sinusoidal signal, and the fitting model aims to determine the unknown frequencies and sine and cosine linear coefficients. Extrapolating the dipole moment is used to achieve high resolution absorption spectra from shorter dipole trajectories, reducing the duration of computationally heavy real-time simulations. The fitting model is tested on the z-component of the dipole moment of some atoms and small molecules, calculated using real-time time-dependent coupled cluster theory. A broadband laser is used to populate excited states. Extrapolation of short trajectories of the dipole moment gave spectra indistinguishable from the spectra obtained from simulations of 6000 a.u. or longer for He (extrapolated from 20 a.u.), H_2 (100 a.u.) and Be (150 a.u.), all using the aug-cc-pVTZ basis set. The difficulty of extrapolating the dipole moment was seen to increase with the spectral density. A trajectory of 1250 a.u. was needed to achieve a perfect extrapolation to 8000 a.u. of the LiH dipole moment using the aug-cc-pVDZ basis, although trajectories down to 300 a.u. gave decent approximations. The fitting model was unable to perfectly reproduce the high resolution spectrum (8000 a.u.) for H_2O using the aug-cc-pVDZ basis. A more restricted form of the electric dipole was also implemented, using the linear response theory to determine the sign of the coefficients. The implementation enforcing the expected sign of the coefficients gave either the same or better results for all systems. This greatly improved the accuracy of the approximated spectra of H_2O, giving decent extrapolations of trajectories down to 300 a.u..

Acknowledgments

First and foremost, I would like to thank my supervisor, Prof. Thomas Bondo Pedersen, for pushing me up a steep learning curve of quantum chemistry throughout this work. Our regular discussions and his willingness to answer my (many) questions have been critically important during the process of developing the fitting model for the electric dipole moment.

Thank you to my co-supervisor Prof. Trygve Helgaker, and the entire coupled cluster group at the Hylleraas Centre for Quantum Molecular Sciences at UiO for helpful scientific discussions. I have much appreciated the friendly and collaborative work environment. A special thanks to Håkon Emil Kristiansen and Øyvind Sigmundson Schøyen for helping me set up the code for the real-time coupled cluster simulations to obtain the dipole data. I would also like to thank Dr. Lukáš Konečný from the Hylleraas Centre at the University of Tromsø for useful discussions on the Fourier-Padé approximant.

A big thank you to my grandfather, Prof. Eivind Hiis Hauge, for motivational words and invaluable feedback on my thesis. Lastly, I would like to thank my husband, Branislav Jenčo, for emotional support and tedious proof-reading.

Contents

List of Figures

List of Tables

CHAPTER 1

Introduction

Real-time time-dependent molecular electronic structure simulations are used to study spectroscopic properties of molecules. The property of interest in this project is the electronic absorption spectrum. A short laser pulse is added as a perturbation to the molecular system in order to populate excited states, creating oscillations in the time-dependent electric dipole moment. Obtaining the absorption spectrum requires the imaginary part of the Fourier transform

$$\mathcal{F}[\mu(t)] = \frac{1}{2\pi}\int_{-\infty}^{\infty} \mu(t) e^{\mathrm{i}\omega t}\ \mathrm{d}t \tag{1.1}$$

of the time-dependent electric dipole moment $\mu(t)$. The calculated dipole moment is known on a discrete, evenly spaced time domain $\{t_n\}$, with $t_n = n\Delta t + t_0$ for $n = 0, 1, \ldots, N_t - 1$ with time step Δt. The Fourier transform must therefore be approximated using a discrete algorithm. The discrete Fourier transform yields a discrete function, given by

$$\mu(\omega_k) = \frac{1}{N_t}\sum_{n=0}^{N_t-1} \mu(t_n) e^{\mathrm{i}\omega_k n\Delta t}, \tag{1.2}$$

where $\omega_k = k\Delta\omega$, with $\Delta\omega = \frac{2\pi}{N_t\Delta t}$ for $k = 0, 1, \ldots, N_t/2 - 1$. The resolution of the discrete Fourier transform is determined by the length of the dipole trajectory $N_t\Delta t$, requiring long simulations in order to achieve decent looking spectra. Low spectral resolution, meaning a large value for $\Delta\omega$, can cause adjacent peaks in the spectrum to merge into a single wider peak. This is illustrated in Fig. 1.1, where the details in the Fourier spectrum become visible as $N_t\Delta t$ increases.

This poses a challenge, as the N-electron problem must be solved before evaluation of each $\mu(t_n)$. For accurate methods, these long simulations become prohibitively expensive for anything but small molecules.

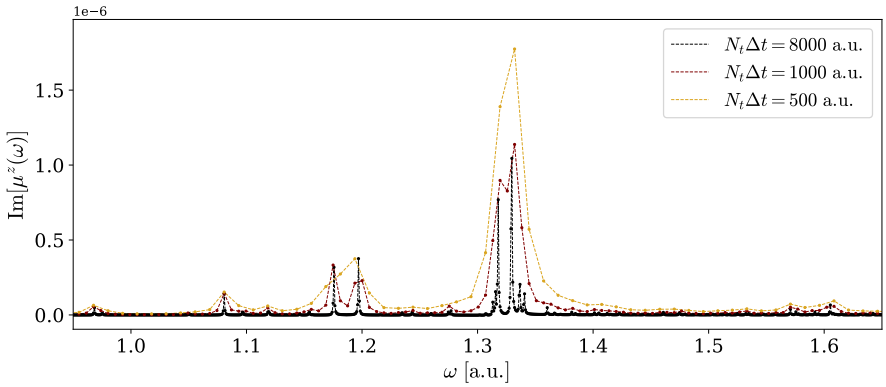

Figure 1.1: Illustration of the spectral resolution for different trajectory lengths $N_t\Delta t$, using $\Delta t = 0.01$ a.u.. The example shows the z-component of the dipole moment of H_2O, computational details may be found in Section 10.1.

There is a long history of using signal processing to speed up simulations in both classical and quantum dynamics, including calculations of electronic absorption spectra. A class of methods, called *harmonic inversion*, aims to improve the spectral analysis of discrete time signals.[1] Harmonic inversion methods have been continuously developed and used for fitting discrete signals in computational chemistry over the past decades.

In the 80's, new harmonic inversion methods like *multiple signal classification (MUSIC)* proposed by Schmidt[2] and *estimation of signal parameters via rotational invariance technique (ESPRIT)* by Roy and Kailath[3] were developed and studied in relation to molecular dynamics and spectral analysis.[4,5] Later, the *filter-diagonalization* method was developed in the 90's by Wall and Neuhauser[6,7] to determine eigenvalues and eigenstates of an operator in a given energy range, and has later also been used in spectroscopy.[8–11] In recent years, the Fourier-Padé approximant was introduced by Bruner et al.[12] to accelerate real-time simulations of the absorption spectrum. The use of the Fourier-Padé approximant was known long before the publication of Bruner et al., but the work combined the method with an occupied-virtual molecular orbital decomposition of the dipole moment, as originally proposed by Repisky et al.[13,14]. This made it possible to improve more than only sparse spectra. The Fourier-Padé has gained popularity among researchers calculating absorption spectra using real-time methods.[15–17]

The methods of harmonic inversion have been widely used and studied, though signals with large numbers of frequencies cause problems for all the methods mentioned above. All methods for harmonic inversion requires solving large linear systems prone to near-degeneracy.[1,18]

Harmonic inversion methods improve the resolution of the spectrum directly in the frequency domain. To the best of my knowledge, there are no publications on improving the resolution by extrapolating the electric dipole moment in the time domain. Such an extrapolation will be the main goal of this master project.

As will be shown later, the time-dependent dipole moment should evolve like a multi-sinusoidal signal. The regular harmonic form of the molecular property leads to the central question of this thesis:

Can we reduce the computational cost of the real-time simulated absorption spectrum by forecasting the time-dependent electric dipole moment?

By exploiting the periodic property of the time-dependent dipole moment, the goal is to achieve high resolution spectra from shorter real-time simulations.

This master thesis will propose a method for extrapolating the time-dependent electric dipole moment from real-time coupled cluster theory. A possible advantage of an extrapolation over the methods for harmonic inversion is that the error in the extrapolation might be easier to quantify. An important part of this thesis will therefore be to create and study a measure of error for the approximated dipole moment. Finding a reliable convergence criterion would enable automatic termination of the real-time simulations once the fitting-criterion is reached.

A decomposition of the dipole moment will be used, to see if it can simplify the extrapolation in the time domain. Such decomposition simplified the interpolation in the frequency domain when using the Fourier-Padé approximant in the work of Bruner et al.[12]. To the best of my knowledge, there currently exists no published work on a molecular orbital pair decomposition of the coupled cluster dipole moment. Some attention to dipole moment molecular orbital decomposition in coupled cluster theory will therefore be given in this project.

The thesis is divided into three main components. The first part aims to provide background on both the exact theory on electronic transition spectra, and some introduction to the coupled-cluster method. The true form of the exact dipole moment motivates the choices of the extrapolation method. Next, the proposed method for the dipole moment extrapolation is presented, along with a few implementation details. In the third part the results are presented and discussed, and the end provides a conclusion for the project.

PART I

Theoretical Background

CHAPTER 2

The Dipole Moment in Exact Quantum Theory

To obtain the electronic transition spectrum, the targeted molecule is subjected to a short laser pulse. The energy added to the system by the external field causes electron excitations, forcing the molecule out of its ground state. As will be shown in Chapter 4, the calculated absorption spectrum from a real-time simulation uses the Fourier-transform $\mathcal{F}[\mu(t)]$ of the time-dependent dipole moment, $\mu(t)$. The *dipole moment* will in this thesis always refer to the *electric* dipole moment. The dipole moment is given by

$$\boldsymbol{\mu}(t) = \langle \Psi(t) | \, \hat{\boldsymbol{\mu}} \, | \Psi(t) \rangle \,, \tag{2.1}$$

showing that it is the expectation value of the electric dipole operator, $\hat{\boldsymbol{\mu}}$.

Before looking at the form of the electric dipole operator, it should be mentioned that discussions in this project are limited to the so-called *closed shell restricted form*, requiring orbitals to appear in pairs. All electron dynamics simulations in this project will use the restricted form, as this reduces the computational cost. The spin orbitals $\phi_{p\alpha}(\mathbf{r}, m_s) = \psi_p(\mathbf{r})\alpha(m_s)$ and $\phi_{p\beta}(\mathbf{r}, m_s) = \psi_p(\mathbf{r})\beta(m_s)$ will share the spatial orbital $\psi_p(\mathbf{r})$, differing only in the spin component, $\sigma(m_s)$.[19]

The equations will be given in second quantization, using the *creation operators* $\hat{a}^\dagger_{p\sigma}$ and *annihilation operators*, $\hat{a}_{p\sigma}$. The elementary operators add ($\hat{a}^\dagger_{p\sigma}$) and remove ($\hat{a}_{p\sigma}$) an electron from the spin-orbital $\phi_{p\sigma}$ when acting on a state. The second quantization formalism in this thesis follows that of Helgaker et al.[20,21]. All equations are given in atomic units.

The dipole operator has three components, one for each spatial coordinate. The dipole operator in direction $d \in \{x, y, z\}$ is given by

$$\hat{\mu}^d = \sum_{pq} P^d_{pq} \hat{E}_{pq}, \tag{2.2}$$

where the indexes refer to general orbitals ψ_p and ψ_q, and $\hat{E}_{pq}$ is the *singlet excitation operator*:

$$\hat{E}_{pq} = \hat{a}^\dagger_{p\alpha}\hat{a}_{q\alpha} + \hat{a}^\dagger_{p\beta}\hat{a}_{q\beta} \tag{2.3}$$

and $\mathbf{P}^d$ is the electric dipole transition matrix for spatial coordinate d. The elements of $\mathbf{P}^d$ are given by

$$P^x_{pq} = -\int \psi^*_p(\mathbf{r}) x \psi_q(\mathbf{r}) \ \mathrm{d}\mathbf{r} \tag{2.4}$$

$$P^y_{pq} = -\int \psi^*_p(\mathbf{r}) y \psi_q(\mathbf{r}) \ \mathrm{d}\mathbf{r} \tag{2.5}$$

$$P^z_{pq} = -\int \psi^*_p(\mathbf{r}) z \psi_q(\mathbf{r}) \ \mathrm{d}\mathbf{r}, \tag{2.6}$$

where the negative sign in all three equations arises from the electron charge. The electric dipole moment will then also have three components:

$$\mu^d(t) = \langle \Psi(t) | \, \hat{\mu}^d \, | \Psi(t) \rangle \,, \tag{2.7}$$

for $d \in \{x, y, z\}$.

This chapter will introduce the time-dependent Schrödinger equation. There is no analytical solution to the Schrödinger equation for many-body systems. The calculated wave function, and hence also the molecular properties, will be approximated. The exact solution to the time-dependent electric dipole moment will still be presented, as it will be used in the fitting model.

2.1 Schrödinger's Equation

The wave function $|\Psi(t)\rangle$ evolves according to Schrödinger's equation. The time-dependent non-relativistic Schrödinger equation is given by

$$\hat{H}(t) \, | \Psi(t) \rangle = \mathrm{i} \frac{\mathrm{d}}{\mathrm{d}t} \, | \Psi(t) \rangle \,, \tag{2.8}$$

where the time-dependent electronic Hamiltonian may be divided according to

$$\hat{H}(t) = \hat{H}_0 + \hat{V}(t). \tag{2.9}$$

The first term $\hat{H}_0$ is the time-independent electronic Hamiltonian within the Born-Oppenheimer approximation[22]. The Born-Oppenheimer approximation postulates that each nucleus may be treated as a point charge with fixed position, leaving only the electron dynamics to be solved. The justification for the approximation is that the displacement of the nuclei is negligible compared to that of the electrons, due to their vast difference in mass. The time-independent electronic Hamiltonian is given by

$$\hat{H}_0 = \hat{h} + \hat{g} + h_{\mathrm{nuc}}, \tag{2.10}$$

where $\hat{h}$ is the one-electron part of the Hamiltonian, describing the kinetic energy of the electrons and the attractive forces between the electrons and the stationary nuclei. Mathematically, this is described by

$$\hat{h} = \sum_{pq} h_{pq} \hat{E}_{pq} \tag{2.11}$$

$$h_{pq} = \int \psi^*_p(\mathbf{r}) \left(-\frac{1}{2} \nabla^2 - \sum_I \frac{Z_I}{r_I} \right) \psi_q(\mathbf{r}) \ \mathrm{d}\mathbf{r}, \tag{2.12}$$

where p and q denote general spatial orbitals. The sum in the integral runs over all the nuclei in the molecule, where Z_I is the charge of the nucleus and r_I is the distance between the electron and the I'th nucleus.

The second term $\hat{g}$ is the two-body part of the Hamiltonian, describing the electron-electron repulsion. This term is given by

$$\hat{g} = \frac{1}{2}\sum_{pqrs} g_{pqrs}\hat{e}_{pqrs} \tag{2.13}$$

$$g_{pqrs} = \iint \psi_p^*(\mathbf{r}_1)\psi_r^*(\mathbf{r}_2)\frac{1}{r_{12}}\psi_q(\mathbf{r}_1)\psi_s(\mathbf{r}_2)\, d\mathbf{r}_1 d\mathbf{r}_2, \tag{2.14}$$

where r_{12} is the distance between the two electrons in the integral and $\hat{e}_{pqrs}$ is the *two-electron excitation operator* given by

$$\hat{e}_{pqrs} = \hat{E}_{pq}\hat{E}_{rs} - \delta_{qr}\hat{E}_{ps}, \tag{2.15}$$

where r and s also denote general spatial orbitals

The final term in the unperturbed Hamiltonian is the constant nuclear repulsion:

$$h_{\text{nuc}} = \sum_{I>J}\frac{Z_I Z_J}{r_{IJ}}, \tag{2.16}$$

which sums over all unique nucleus pairs, where r_{IJ} is the distance between the nuclei pair.

The second term $\hat{V}(t)$ in the time-dependent Hamiltonian from Eq. (2.9), will be a time-dependent semi-classical interaction operator $\hat{V}(t)$, describing the interactions between the electrons in the system with a time-dependent external field, $\mathrm{F}(t)$ which is nonzero only for $0 < t \leq t_p$. The general form of the interaction operator, according to *the electric-dipole approximation*, is given by

$$\hat{V}(t) = -\hat{\boldsymbol{\mu}} \cdot \mathbf{u}\mathrm{F}(t), \tag{2.17}$$

where $\hat{\boldsymbol{\mu}}$ is the electric dipole operator as defined in Eq. (2.2), $\mathbf{u}$ is the unit vector determining the polarization direction of the field and $\mathrm{F}(t)$ describes a spatially uniform electric field.[23]

2.2 Time Evolution of the Exact Wave Function

The time-dependent ground state wave function can be expressed as

$$|\Psi(t)\rangle = \sum_n c_n(t)\,|n\rangle\,, \tag{2.18}$$

summing over all possible time-independent electronic states, forming a complete orthonormal basis. Each state $|n\rangle$ is a solution to the time independent Schrödinger equation, such that $\hat{H}_0\,|n\rangle = E_n\,|n\rangle$.[24,25]

The system is initially in its unperturbed ground state $|\Psi(t=0)\rangle = |0\rangle$, before the external field has been switched on. At time t_p, the laser pulse has been turned off, and the Hamiltonian is reduced to the unperturbed Hamiltonian, $\hat{H}(t > t_p) = \hat{H}_0$ for the rest of the simulation. The energy of the system will

then remain constant. The time dependent Schrödinger equation for $t > t_p$ becomes

$$\hat{H}_0 \left|\Psi(t)\right\rangle = \mathrm{i}\frac{\mathrm{d}}{\mathrm{d}t}\left|\Psi(t)\right\rangle, \tag{2.19}$$

where the corresponding wave function will evolve according to

$$\left|\Psi(t)\right\rangle = e^{-\mathrm{i}\hat{H}_0(t-t_p)}\left|\Psi(t_p)\right\rangle. \tag{2.20}$$

By expressing the evolution operator $e^{-\mathrm{i}\hat{H}_0(t-t_p)}$ as a Taylor series and allowing the Hamiltonian to act on the electronic states, the wave function may be rewritten as

$$\left|\Psi(t)\right\rangle = \sum_n c_n(t_p) e^{-\mathrm{i}E_n(t-t_p)}\left|n\right\rangle, \tag{2.21}$$

giving the final expression for the exact wave function at $t \geq t_p$. The coefficients in the exact wave function are periodic in time after the external field is switched off, evolving according to

$$c_n(t) = c_n(t_p) e^{-\mathrm{i}E_n(t-t_p)}. \tag{2.22}$$

This is an important observation, as the absorption spectra are only calculated using the time after the external field has been switched off. The reason for this will be revealed in Chapter 4, but some background on both the wave function and the dipole moment should be provided before taking on the response theory. For now, the claim is that the Fourier transform of $\boldsymbol{\mu}(t)$ for $t \geq t_p$ is the key to obtaining the absorption spectrum.

2.3 The Exact Dipole Moment

The time dependence of the electric dipole moment lies exclusively in the wave function, as the electric dipole operator $\hat{\mu}^d$ is time-independent. The expectation value of the time dependent electric dipole moment is given by

$$\mu^d(t) = \left\langle\Psi(t)\right|\hat{\mu}^d\left|\Psi(t)\right\rangle = \sum_{nm} c_n^* c_m \left\langle n\right|\hat{\mu}^d\left|m\right\rangle e^{\mathrm{i}\omega_{nm}(t-t_p)}, \tag{2.23}$$

where $\omega_{nm} = E_n - E_m$ is known as the Bohr frequency for the transition between states m and n, and the shorthand notation $c_n \equiv c_n(t_p)$ is used for simplicity.

To rewrite the expression, three observations are necessary. Firstly, since the electric dipole operator is Hermitian, then $\left\langle n\right|\hat{\mu}^d\left|m\right\rangle^* = \left\langle m\right|\hat{\mu}^d\left|n\right\rangle$. Secondly, $(c_n^* c_m)^* = c_m^* c_n$ and thirdly $e^{\mathrm{i}\omega_{mn}(t-t_p)} = (e^{\mathrm{i}\omega_{nm}(t-t_p)})^*$ because $\omega_{mn} = -\omega_{nm}$. Using these properties, it becomes apparent that

$$c_m^* c_n \left\langle m\right|\hat{\mu}^d\left|n\right\rangle e^{\mathrm{i}\omega_{mn}(t-t_p)} = \left\langle n\right|\hat{\mu}^d\left|m\right\rangle^* (c_n^* c_m e^{\mathrm{i}\omega_{nm}(t-t_p)})^*, \tag{2.24}$$

showing that the imaginary terms will be canceled out in the sum. The time dependent dipole moment may then be written as

$$\mu^d(t) = 2\sum_{n>m} \mathrm{Re}\left[\left\langle n\right|\hat{\mu}^d\left|m\right\rangle c_n^* c_m e^{\mathrm{i}\omega_{nm}(t-t_p)}\right] + \sum_n |c_n|^2 \left\langle n\right|\hat{\mu}^d\left|n\right\rangle, \tag{2.25}$$

since $\omega_{nn} = 0$. By rewriting $2 \langle n| \hat{\mu}^d |m\rangle c_n^* c_m = A_{nm} + \mathrm{i}B_{nm}$, such that

$$A_{nm} = 2\,\mathrm{Re}\left[\langle n| \hat{\mu}^d |m\rangle c_n^* c_m\right] \tag{2.26}$$

$$B_{nm} = 2\,\mathrm{Im}\left[\langle n| \hat{\mu}^d |m\rangle c_n^* c_m\right], \tag{2.27}$$

then the new formulation of time dependent dipole will be

$$\mu^d(t) = \sum_{n>m} \left[A_{nm}\cos(\omega_{nm}(t-t_p)) - B_{nm}\sin(\omega_{nm}(t-t_p))\right] + D \tag{2.28}$$

where the constant is given by

$$D = \sum_n |c_n|^2 \langle n| \hat{\mu}^d |n\rangle . \tag{2.29}$$

Using the angle subtraction theorems for trigonometric functions, the expression may be further simplified to

$$\mu^d(t) = \sum_i \left[\tilde{A}_i \cos(\omega_i t) + \tilde{B}_i \sin(\omega_i t)\right] + D, \tag{2.30}$$

where i represents a unique pair of states $i \mapsto (m, n)$. The new coefficients are given by

$$\tilde{A}_{i\mapsto(n,m)} = A_{nm}\cos(\omega_{nm}t_p) + B_{nm}\sin(\omega_{nm}t_p) \tag{2.31}$$

$$\tilde{B}_{i\mapsto(n,m)} = A_{nm}\sin(\omega_{nm}t_p) - B_{nm}\cos(\omega_{nm}t_p). \tag{2.32}$$

This shows that the exact time-dependent electric dipole moment evolves like a multi-sinusoidal signal, where the frequencies are all Bohr frequencies corresponding to electronic transition energies. The compact form in Eq. (2.30) is the motivation for this project, as the regular harmonic form of the dipole moment should make it ideal for time series forecasting.

CHAPTER 3

The Approximated Wave Function

The wave function in many-body dynamics usually uses the basis set approximation. The wave function is constructed in a molecular orbital (MO) space, $\{\phi_{p\sigma}\}$. The MOs are in turn usually expressed through an *atomic orbital (AO)* basis, $\{\chi_{\upsilon\sigma}\}$.[19] The MOs are then given by

$$\phi_{p\sigma}(\mathbf{r}, m_s) = \sum_{\upsilon} C_{\upsilon p}\chi_{\upsilon}(\mathbf{r})\sigma(m_s), \tag{3.1}$$

where the MOs are often held constant throughout time, but *adaptive* methods using time-dependent orbitals do exist.[26,27] This project will be limited to time-independent orbitals, where the expansion is given by the restricted *Hartree-Fock (HF)* ground state.

The exact wave function, within the Born-Oppenheimer approximation, can be obtained in the limit of an infinitely large basis set. Using a complete basis is not possible in computations, the finite expansion causing a *basis set error*. Basis sets exits in various sizes, giving a trade-off between the basis set size and computational expense.

This chapter will present the exact wave function within the basis set approximation, from *full configuration interaction (FCI)* theory. The method is too expensive for all but the smallest systems, with factorial scaling of the computations. The theory is still included, as it illustrates how the information about the excited states in Section 2.2 is lost in a primitive expansion using a reference state. Popular theories, like *configuration interaction (CI)* and *coupled cluster (CC)*, provide approximations to the FCI wave function. The method used to model the electron dynamics in this project is real-time time-dependent coupled cluster theory. A short introduction to coupled cluster theory will therefore be given. Since the reference state in this project will be a Hartree-Fock state, some HF theory will also be included. The theory in this chapter is based on the explanations of Helgaker et al.[24,28–30].

3.1 Hartree-Fock Theory

The HF wave function consists of either one *Slater determinant* or one *configuration state function (CSF)*. The wave function therefore only consists of a single spin orbital configuration. From an initial state of orthonormal MOs $|\Phi_0\rangle$, the HF method performs unitary rotations on the orbital space $|\mathrm{HF}\rangle = e^{-\hat{\kappa}}|\Phi_0\rangle$, minimizing the energy of the system variationally.

The appropriate rotations can be found using a set of effective one-electron Schrödinger equations, called the *Hartree-Fock equations*. The effective one-electron operator is called the *Fock operator* and is given by

$$\hat{f} = \hat{h} + \hat{V}^f, \tag{3.2}$$

where $\hat{h}$ is the true one-electron part of the Hamiltonian from Eq. (2.11), while the second term is the effective one-electron potential called the *Fock potential*. The Fock potential provides an average Coulomb repulsion among the electrons, as given by

$$\hat{V}^f = \sum_{pq} V^f_{pq} \hat{E}_{pq} = \sum_{pq} \sum_{i} (2g_{pqii} - g_{piiq}) \hat{E}_{pq}, \tag{3.3}$$

where $\hat{E}_{pq}$ and g_{pqrs} are defined in Eqs. (2.3) and (2.14), respectively. The *canonical representation* in HF theory provides optimized spin orbitals which are eigenfunctions of the Fock operator

$$\hat{f}\hat{a}^\dagger_{p\sigma} |\text{vac}\rangle = \varepsilon_p \hat{a}^\dagger_{p\sigma} |\text{vac}\rangle \,, \tag{3.4}$$

where $|\text{vac}\rangle$ is the vacuum state. The pseudo eigenvalue problem is solved iteratively, using the *self-consistent field method*.

The time-independent Hamiltonian may be written as

$$\hat{H}_0 = \hat{f} + \hat{\Phi} + h_{\text{nuc}}. \tag{3.5}$$

where one may consider the *fluctuation potential*:

$$\hat{\Phi} = \hat{g} - \hat{V}^f \tag{3.6}$$

as a perturbation to the Fock operator. The HF wave function can then be though of as the unperturbed wave function with respect to electron correlation, as the effective one-electron potential only accounts for the Fermi correlation. There are several post-Hartree-Fock methods which provide correction for the electron correlation, using the HF ground state as their reference state.

3.2 Full Configuration Interaction

The exact solution to the Schrödinger equation within a given basis set is found in FCI theory. The time-dependent FCI wave function is given by

$$|\text{FCI}(t)\rangle = \left(c_0 + \sum_{\nu} c_\nu(t) \hat{\tau}_\nu \right) |\text{HF}\rangle \,, \tag{3.7}$$

where the reference state $|\text{HF}\rangle$ in this case is the Hartree-Fock state and $\hat{\tau}_\nu$ is an excitation operator with corresponding coefficient c_ν. The excitation operator excites one ($\hat{\tau}^a_i = \hat{E}_{ia}$) or several ($\hat{\tau}^{ab\cdots}_{ij\cdots} = \hat{E}_{ia}\hat{E}_{jb}\cdots$) electrons from occupied to virtual molecular orbitals in the reference state, creating a linear combination of all N-electron Slater determinants (or CSFs) in the Fock space of a given one-electron basis. In a complete one-electron basis set, the FCI wave function would be equivalent to the exact wave function in Eq. (2.18).

The information about the excited states is lost in the primitive expansion. They can be calculated, but at an excessive computational cost. This means that the frequencies ω_{mn} in Eq. (2.23) remain unknown in any real-time simulation.

3.3 Time-Independent Coupled Cluster Theory

The CC wave function approximates the FCI wave function by the exponential reformulation

$$|\mathrm{CC}\rangle = e^{\hat{T}} |\mathrm{HF}\rangle , \tag{3.8}$$

where $\hat{T}$ is the cluster operator and $e^{\hat{T}}$ is acting on the reference state, which in this case is the Hartree-Fock state. The cluster operator sums over all excitations ν:

$$\hat{T} = \sum_{\nu} t_\nu \hat{\tau}_\nu, \tag{3.9}$$

where t_ν is the cluster amplitude corresponding to the excitation operator $\hat{\tau}_\nu$. The CC wave function is equivalent to the FCI wave function when the cluster operator is not truncated. The cluster operator is often truncated such that it only includes excitations up to a given level, though the exponential form of the CC wave function provides contributions from higher order excitations through *disconnected* excitations, $\hat{\tau}_\gamma = \hat{\tau}_\eta \hat{\tau}_\nu$. The CC wave function is highly dependent on the reference state giving a decent approximation to the ground state of the system. The cluster operator includes description of the *dynamical correlation*, arising from the Coulomb repulsion. The truncated cluster operator does however not help with the description of *static correlation*, arising from near degeneracies among configurations. Systems with such degeneracies should be described by multi-reference methods.

The method used in this project was *coupled cluster singles and doubles (CCSD)*, where the cluster operator is truncated such that it only includes single and double excitations:

$$\hat{T} = \hat{T}_1 + \hat{T}_2 = \sum_{ia} t_i^a \hat{\tau}_i^a + \sum_{i>j} \sum_{a>b} t_{ij}^{ab} \hat{\tau}_{ij}^{ab}. \tag{3.10}$$

Normalization of the CC wave function $\langle \mathrm{CC}|\mathrm{CC}\rangle = 1$, and calculations using the complex conjugate $\langle \mathrm{CC}|$ of the CC wave function in general, come at a significant computational cost. The complex conjugate of the CC wave function is therefore approximated. In the variational reformulation of CC theory, the bra state is given by

$$\langle \Lambda| = \langle \mathrm{HF}| + \sum_{\eta} \langle \eta| \lambda_\eta e^{-\hat{T}}, \tag{3.11}$$

summing over all excited states $|\eta\rangle \equiv \hat{\tau}_\eta |\mathrm{HF}\rangle$ obtained by the truncated cluster operator. The normalization criterion $\langle \Lambda|\mathrm{CC}\rangle = 1$ is fulfilled. The Lagrange multipliers λ_η constitute an additional set of unknowns, but the advantage of the variational reformulation is that one may invoke the Hellmann-Feynman theorem[31] to simplify the calculations of the molecular properties.

3.4 Time Evolution of the Coupled Cluster Wave Function

The time-dependent coupled cluster theory in this section is based on the work of Koch and Jørgensen[32].

In time-dependent coupled cluster theory, the time-dependent Schrödinger equations for the bra-state and ket-state respectively are given by

$$e^{-\hat{T}(t)} \mathrm{i} \frac{\mathrm{d}}{\mathrm{d}t} |\mathrm{CC}(t)\rangle = e^{-\hat{T}(t)} \hat{H}(t) |\mathrm{CC}(t)\rangle \tag{3.12}$$

$$\left(\frac{\mathrm{d}}{\mathrm{d}t}\langle\Lambda(t)|\right)e^{\hat{T}(t)} = \mathrm{i}\,\langle\Lambda(t)|\,\hat{H}(t)e^{\hat{T}(t)}, \tag{3.13}$$

where the cluster amplitudes as well as the Lagrange multipliers are time-dependent. The CC bra and ket states are given by

$$|\mathrm{CC}(t)\rangle = e^{\hat{T}(t)}\,|\mathrm{HF}\rangle\,e^{\mathrm{i}\xi(t)} \tag{3.14}$$

$$\langle\Lambda(t)| = e^{-\mathrm{i}\xi(t)}\left(\langle\mathrm{HF}| + \sum_{\eta}\langle\eta|\,\lambda_{\eta}(t)e^{-\hat{T}(t)}\right), \tag{3.15}$$

where $\xi(t)$ is the complex-valued phase factor of the wave function. For details on solving the time-dependent coupled-cluster equations, the reader is referred to the work of Pedersen and Kvaal[33].

As remarked by Huber and Klamroth[34], the CC wave function is expected to be equivalent to a linear combination of excited states, though the non-linear form the CC equations makes this difficult to prove. It is still a strong assumption that the form in Eq. (2.18), and hence also the form of the dipole moment in Eq. (2.23) holds for CC theory.

3.5 The Dipole Moment in Coupled Cluster Theory

The time-dependent electric dipole moment in RT-TDCC simulations is calculated as the real part of the expectation value

$$\mu^d(t) = \langle\Lambda(t)|\,\hat{\mu}^d\,|\mathrm{CC}(t)\rangle = \sum_{pq} P^d_{pq}D_{pq}(t), \tag{3.16}$$

where $\mathbf{P}^d$ is the electric dipole transition matrix for direction d, as given in Eqs. (2.4) to (2.6) and $\mathbf{D}(t)$ is the one-body density matrix. The CC expectation value will have an imaginary component close to zero when the CC-ket $|\mathrm{CC}(t)\rangle$ and CC-bra $\langle\Lambda(t)|$ provide good approximations to the FCI wave function and its conjugate. A large imaginary component in the CC expectation value indicates that the truncated cluster operator inadequately describes the electron correlation. The expectation value of the hermitian operator $\hat{\mu}^d$ should be real, and the imaginary component is therefore discarded. The elements of the one-body density matrix will be given by only the real component

$$D_{pq}(t) = \mathrm{Re}\Big\{\langle\Lambda(t)|\,\hat{E}_{pq}\,|\mathrm{CC}(t)\rangle\Big\}, \tag{3.17}$$

since only $\mathbf{D}(t)$ can contribute to the imaginary component of the expectation value in CC theory using real orbitals.

The general rule for the trace of the product $\mathbf{A}^\intercal\mathbf{B}$, where both matrices $\mathbf{A}$ and $\mathbf{B}$ have size $N \times M$, is given by $\mathrm{Tr}(\mathbf{A}^\intercal\mathbf{B}) = \sum_{ij} A_{ij}B_{ij}$. This may be used to rewrite the dipole moment into

$$\mu^d(t) = \mathrm{Tr}\big[(\mathbf{P}^d)^\intercal\mathbf{D}(t)\big] = \mathrm{Tr}\big[(\mathbf{P}^d)^*\mathbf{D}(t)\big] = \mathrm{Tr}\big[\mathbf{P}^d\mathbf{D}(t)\big], \tag{3.18}$$

as the transition matrix is symmetric when using real orbitals.

The form of the dipole moment in Eq. (3.18) is a general form for the dipole moment in real-time simulations. The form of the dipole moment in the time-domain from real-time simulations will therefore provide no direct information about the frequencies in the signal.

CHAPTER 4

The Absorption Spectrum in Laser-Driven Dynamics

The absorption cross section in the electric dipole approximation, following the explanation of Goings et al.[35], is defined as the average number of absorbed photons $\Delta N(\omega)$ per average photon density $N(\omega)/A$. The absorption cross section is then given by

$$S(\omega) = \frac{\Delta N(\omega)}{N(\omega)} A, \tag{4.1}$$

for a given frequency ω. From the initial ground state, where only $|0\rangle$ is populated, the photon absorption can be determined by the decrease in electronic population in the ground state. The electronic absorption spectrum is commonly written as

$$S(\omega) = \frac{4\pi\omega}{3c} \operatorname{Im}[\alpha_{xx}(\omega) + \alpha_{yy}(\omega) + \alpha_{zz}(\omega)] \tag{4.2}$$

where c is the speed of light and α_{dd} are elements of the dipole polarizability tensor, $\boldsymbol{\alpha}(\omega)$. While the imaginary part of the dipole polarizability tensor gives the absorption, the real part describes the photon dispersion.

The three contributions $\alpha_{dd}(\omega)$ for $d \in x, y, z$, give a rotational average for the absorption spectrum. The tensor $\boldsymbol{\alpha}(\omega)$ may be written in terms of the linear response function. A short summary of relevant response theory will therefore be given. The description of response theory given in this chapter is based on work by Jørgensen et al.[32,36] and Pedersen[37].

4.1 Response Theory

The interaction operator $\hat{V}(t)$ may be treated as a perturbation, requiring the external field to have much less impact on the electronic structure than the internal forces of the molecule. The electronic ground state to the K'th order in time-dependent perturbation theory is given by the sum of all perturbation contributions up to the K'th order:

$$|\Psi(t)\rangle = \left(\left|\Psi^{(0)}\right\rangle + \left|\Psi^{(1)}(t)\right\rangle + \left|\Psi^{(2)}(t)\right\rangle + \ldots \left|\Psi^{(K)}(t)\right\rangle\right) e^{\mathrm{i}\xi(t)} \tag{4.3}$$

where the real phase factor $\xi(t)$ is as described by Olsen and Jørgensen[36] and the corrections to the wave function may be determined by Ehrenfest's theorem[38]. The magnitude of the contributions decreases significantly with the perturbation

order. The zero'th order wave function $\left|\Psi^{(0)}\right\rangle = |0\rangle$ is the electronic ground state of the unperturbed Hamiltonian, $\hat{H}_0$ from Eq. (2.10).

Equivalently, the electric dipole moment in perturbation theory to the K'th order is given by

$$\boldsymbol{\mu}(t) = \boldsymbol{\mu}^{(0)} + \boldsymbol{\mu}^{(1)}(t) + \ldots + \boldsymbol{\mu}^{(K)}(t), \tag{4.4}$$

where the $\boldsymbol{\mu}^{(k)}(t)$ is the k'th order correction to the dipole moment. The zero'th order dipole moment is the dipole moment for the system in the unperturbed ground state,

$$\boldsymbol{\mu}^{(0)} = \langle 0| \boldsymbol{\mu} |0\rangle . \tag{4.5}$$

Response theory expresses the perturbation corrections in terms of *response functions*, given by

$$\mathbf{R}^{(k)}(\omega_1, \ldots, \omega_k) = \langle\langle \hat{\boldsymbol{\mu}}; \hat{V}(\omega_1), \ldots, \hat{V}(\omega_k)\rangle\rangle_{\omega_1,\ldots,\omega_k}. \tag{4.6}$$

The general form of the k'th order correction to the dipole moment, describing k-photon transitions, is expressed using a series of inverse Fourier transforms

$$\boldsymbol{\mu}^{(k)}(t) = \frac{1}{k!}\int_{-\infty}^{\infty} \cdots \int_{-\infty}^{\infty} \mathbf{R}^{(k)}(\omega_1, \ldots, \omega_k) e^{-\mathrm{i}(\omega_1+\ldots+\omega_k)t} \ \mathrm{d}\omega_1 \cdots \ \mathrm{d}\omega_k, \tag{4.7}$$

where $\hat{V}(\omega)$ is the Fourier transform of the time-dependent perturbation:

$$\hat{V}(\omega) = \frac{1}{2\pi}\int_{-\infty}^{\infty} \hat{V}(t) e^{\mathrm{i}\omega t} \ \mathrm{d}t = -\frac{\hat{\boldsymbol{\mu}} \cdot \mathbf{u}}{2\pi}\int_{-\infty}^{\infty} \mathrm{F}(t) e^{\mathrm{i}\omega t} \ \mathrm{d}t = -\hat{\boldsymbol{\mu}} \cdot \mathbf{u}\mathrm{F}(\omega). \tag{4.8}$$

The response functions are not time-dependent, but rather depend on the frequencies of the external field. The electric dipole moment calculated through response theory is therefore usually expressed in the frequency domain.

The three components of the dipole polarizability tensor $\boldsymbol{\alpha}(\omega)$ used in the spectrum in Eq. (4.2) are defined as

$$\alpha_{dd}(\omega) = -\langle\langle \hat{\mu}^d; \hat{\mu}^d\rangle\rangle_\omega. \tag{4.9}$$

These elements may be written in terms of the linear response function, which in exact theory is given by

$$\langle\langle \hat{\boldsymbol{\mu}}; \hat{V}(\omega)\rangle\rangle_\omega = \sum_{n\neq 0}\left[\frac{\langle 0| \hat{\boldsymbol{\mu}} |n\rangle \langle n| \hat{V}(\omega) |0\rangle}{\omega - \omega_{n0}} - \frac{\langle 0| \hat{V}(\omega) |n\rangle \langle n| \hat{\boldsymbol{\mu}} |0\rangle}{\omega + \omega_{n0}}\right], \tag{4.10}$$

summing over all excited states, where the Bohr frequency $\omega_{n0} = E_n - E_0$ is the excitation energy from the ground state to the n'th excited state. The linear response function is therefore singular at all frequencies $\omega = \pm\omega_{n0}$. Some simplification yields

$$\begin{aligned}\langle\langle \hat{\mu}^d; \hat{V}_d(\omega)\rangle\rangle_\omega &= -u_d \mathrm{F}(\omega) \sum_{n\neq 0}\left[\frac{\langle 0| \hat{\mu}^d |n\rangle \langle n| \hat{\mu}^d |0\rangle}{\omega - \omega_{n0}} - \frac{\langle 0| \hat{\mu}^d |n\rangle \langle n| \hat{\mu}^d |0\rangle}{\omega + \omega_{n0}}\right] \\ &= -u_d \mathrm{F}(\omega) \langle\langle \hat{\mu}^d; \hat{\mu}^d\rangle\rangle_\omega,\end{aligned} \tag{4.11}$$

giving the new diagonal elements of the dipole polarizability tensor:

$$\alpha_{dd}(\omega) = \frac{\langle\langle \hat{\mu}^d; \hat{V}_d(\omega)\rangle\rangle_\omega}{u_d \mathrm{F}(\omega)}, \tag{4.12}$$

providing the link between the linear response function and the electron absorption spectrum in Eq. (4.2). Since the absorption spectrum can be written in terms of the linear response function, the definition of the spectrum only includes one-photon transitions.

4.2 Damping in Response Theory

A requirement of the perturbation operator $\hat{V}(t)$ is that $\hat{V}(-\infty) = 0$, making the initial electronic state $|\Psi(-\infty)\rangle = |0\rangle$ the ground state of the unperturbed system. A way of ensuring this is to introduce a real positive infinitesimal γ. The linear response function in damped response theory is given by

$$\langle\langle \hat{\boldsymbol{\mu}}; \hat{V}(\omega)\rangle\rangle_{\omega+\mathrm{i}\gamma} = \sum_{n\neq 0}\left[\frac{\langle 0|\,\hat{\boldsymbol{\mu}}\,|n\rangle\,\langle n|\,\hat{V}(\omega)\,|0\rangle}{\omega-\omega_{n0}+\mathrm{i}\gamma} - \frac{\langle 0|\,\hat{V}(\omega)\,|n\rangle\,\langle n|\,\hat{\boldsymbol{\mu}}\,|0\rangle}{\omega+\omega_{n0}+\mathrm{i}\gamma}\right], \tag{4.13}$$

where the Fourier transform now includes damping $e^{-\gamma t}$:

$$\hat{V}(\omega) = \frac{1}{2\pi}\int_{-\infty}^{\infty} \hat{V}(t) e^{(\mathrm{i}\omega-\gamma)t}\ \mathrm{d}\omega = \mathcal{F}[\hat{V}(t)e^{-\gamma t}] \tag{4.14}$$

and a single value for γ is used for all excited states. The diagonal of the polarizability tensor with damping is given by

$$\begin{aligned}
\alpha_{dd}(\omega) &= -\langle\langle \hat{\mu}^d; \hat{\mu}^d\rangle\rangle_{\omega+\mathrm{i}\gamma} \\
&= -\sum_{n\neq 0}\left[\frac{\langle 0|\,\hat{\mu}^d\,|n\rangle\,\langle n|\,\hat{\mu}^d\,|0\rangle}{\omega-\omega_{n0}+\mathrm{i}\gamma} - \frac{\langle 0|\,\hat{\mu}^d\,|n\rangle\,\langle n|\,\hat{\mu}^d\,|0\rangle}{\omega+\omega_{n0}+\mathrm{i}\gamma}\right] \\
&= -\sum_{n\neq 0}\left[\frac{\left|\langle 0|\,\hat{\mu}^d\,|n\rangle\right|^2(\omega+\mathrm{i}\gamma+\omega_{n0})}{(\omega+\mathrm{i}\gamma)^2-\omega_{n0}^2} - \frac{\left|\langle 0|\,\hat{\mu}^d\,|n\rangle\right|^2(\omega+\mathrm{i}\gamma-\omega_{n0})}{(\omega+\mathrm{i}\gamma)^2-\omega_{n0}^2}\right] \\
&= -\sum_{n\neq 0} 2\left|\langle 0|\,\hat{\mu}^d\,|n\rangle\right|^2 \frac{\omega_{n0}}{(\omega+\mathrm{i}\gamma)^2-\omega_{n0}^2}.
\end{aligned} \tag{4.15}$$

This reformulation will be important in the next section.

Damped response theory removes the possibility of encountering singularities in the response functions. These singularities occur as the theory does not account for the finite lifetime of the excited states. Damped response theory introduces a common approximation to the finite lifetime of all excited states.[39]

4.3 The Broad-Band Laser as External Field

In order to include all dipole-allowed electronic excitations, a *broad-band laser pulse* is used. The broad-band laser pulse is given by

$$\mathrm{F}(t) = \mathrm{F}_{\mathrm{str}}\delta(t-t_p), \tag{4.16}$$

where $\mathrm{F_{str}}$ is the field strength. The external field represents an instantaneous laser pulse at $t = t_p$, where the system is initially in its ground state. The frequencies of the electric field are given by its Fourier transform:

$$\mathrm{F}(\omega) = \frac{1}{2\pi}\int_{-\infty}^{\infty} \mathrm{F_{str}}\delta(t-t_p)e^{(\mathrm{i}\omega-\gamma)t}\ \mathrm{d}t = \frac{\mathrm{F_{str}}}{2\pi}e^{(\mathrm{i}\omega-\gamma)t_p}, \tag{4.17}$$

using the integration property of the Dirac delta function. As t_p approaches zero, the Fourier transform of the electric field becomes

$$\lim_{t_p\to 0}\mathrm{F}(\omega) = \lim_{t_p\to 0}\frac{\mathrm{F_{str}}}{2\pi}e^{(\mathrm{i}\omega-\gamma)t_p} = \frac{\mathrm{F_{str}}}{2\pi}, \tag{4.18}$$

creating a continuum in the frequency domain. A Dirac delta function is a nonphysical representation of a laser pulse, though conveniently it will populate all dipole-allowed excited states in the system.[13]

Assuming that the first order correction to the dipole moment in a given spatial direction can be written as

$$[\mu^d]^{(1)}(t) = \sum_{n\neq 0}\left[A_n\cos(\omega_{n0}(t-t_p)) + B_n\sin(\omega_{n0}(t-t_p))\right] + D, \tag{4.19}$$

using the known form of the complete d-component of the dipole moment in Eq. (2.23). In the real-time simulations, the induced dipole moment will be zero until t_p. The diagonal elements of the polarizability tensor may then be written as

$$\begin{aligned}\alpha_{dd}(\omega) &= \frac{2\pi}{\mathrm{F_{str}}}e^{-(\mathrm{i}\omega-\gamma)t_p}\langle\langle\hat{\boldsymbol{\mu}};\hat{V}(\omega)\rangle\rangle_{\omega+\mathrm{i}\gamma}\\ &= \frac{2\pi}{\mathrm{F_{str}}}e^{-(\mathrm{i}\omega-\gamma)t_p}\,\frac{1}{2\pi}\int_{-\infty}^{\infty}[\mu^d]^{(1)}(t)\mathcal{H}(t-t_p)e^{(\mathrm{i}\omega-\gamma)t}\ \mathrm{d}t\\ &= \frac{e^{-(\mathrm{i}\omega-\gamma)t_p}}{\mathrm{F_{str}}}\int_{t_p}^{\infty}[\mu^d]^{(1)}(t)e^{(\mathrm{i}\omega-\gamma)t}\ \mathrm{d}t\end{aligned} \tag{4.20}$$

where $\mathcal{H}(t)$ is the Heaviside step function. Shifting the integrals according to

$$\begin{aligned}\alpha_{dd}(\omega) &= \frac{e^{-(\mathrm{i}\omega-\gamma)t_p}}{\mathrm{F_{str}}}\int_{t_p-t_p}^{\infty-t_p}[\mu^d]^{(1)}(t+t_p)e^{(\mathrm{i}\omega-\gamma)(t+t_p)}\ \mathrm{d}t\\ &= \frac{1}{\mathrm{F_{str}}}\int_0^{\infty}[\mu^d]^{(1)}(t+t_p)e^{(\mathrm{i}\omega-\gamma)t}\ \mathrm{d}t\end{aligned} \tag{4.21}$$

simplifies the evaluation of the integrals. This allows a final rewriting of the diagonal elements of the polarizability tensor:

$$\begin{aligned}\alpha_{dd}(\omega) &= \sum_{n\neq 0}\left[\frac{A_n}{\mathrm{F_{str}}}\int_0^{\infty}\cos(\omega_{n0}t)e^{(\mathrm{i}\omega-\gamma)t}\ \mathrm{d}t + \frac{B_n}{\mathrm{F_{str}}}\int_0^{\infty}\sin(\omega_{n0}t)e^{(\mathrm{i}\omega-\gamma)t}\ \mathrm{d}t\right]\\ &+ \frac{1}{\mathrm{F_{str}}}\int_0^{\infty}De^{(\mathrm{i}\omega-\gamma)t}\ \mathrm{d}t\\ &= \sum_{n\neq 0}\frac{A_n}{\mathrm{F_{str}}}\frac{\mathrm{i}\omega-\gamma}{(\omega+\mathrm{i}\gamma)^2-\omega_{n0}^2} - \sum_{n\neq 0}\frac{B_n}{\mathrm{F_{str}}}\frac{\omega_{n0}}{(\omega+\mathrm{i}\gamma)^2-\omega_{n0}^2},\end{aligned} \tag{4.22}$$

where the integrals are solvable under the constraint that γ is positive. By comparing this result with the previous definition of the diagonal elements of the polarizability tensor with damping, one can see that

$$A_n = 0 \tag{4.23}$$

$$B_n = 2\left|\langle 0|\,\hat{\mu}^d\,|n\rangle\right|^2 \mathrm{F_{str}}. \tag{4.24}$$

Since $\left|\langle 0|\,\hat{\mu}^d\,|n\rangle\right|^2$ must be positive and $\mathrm{F_{str}}$ is positive, then it follows that all sine coefficients B_n are also positive. Writing out the expression gives

$$\begin{aligned}[\mu^d]^{(1)}(t) &= \sum_{n\neq 0} B_n \sin(\omega_{n0}(t-t_p)) \\ &= \sum_{n\neq 0} \Big\{ [-B_n \sin(\omega_{n0}t_p)]\cos(\omega_{n0}t) + [B_n \cos(\omega_{n0}t_p)]\sin(\omega_{n0}t) \Big\}\end{aligned} \tag{4.25}$$

From this it follows that the cosine coefficient is expected to be negative as long as $\omega_{n0} < \pi/t_p$, while the sine coefficient is expected to be positive as long as $\omega_{n0} < 0.5\pi/t_p$.

In the numerical real-real time simulation, the Dirac delta function is approximated by the box-shaped function

$$\mathrm{F}(t) = \begin{cases} \mathrm{F_{str}} & \text{if } \; 0 < t \leq t_p \\ 0 & \text{else} \end{cases}. \tag{4.26}$$

and the field is only turned on in the very first time step in the integration, such that $t_p = \Delta t$. This becomes the Dirac delta function in the limit $t_p \to 0$. Approximating the Dirac delta function in numerical integration makes it less predictable to determine what the phase t_p in Eq. (4.25) will be, although it should be close to Δt. The full one-photon absorption spectrum is the average over three simulations, one for each polarization direction. The elements of the unit vector are given by $u_r = \delta_{rd}$ for $d = \{x, y, z\}$, where δ_{rd} is the Kronecker-delta.

4.4 The Absorption Spectrum from Real-Time Simulations

The linear response function is needed in order to calculate the absorption spectrum. Real-time simulations only provide the complete dipole-moment, and give no information about the different orders of perturbation in Eq. (4.4). By using a weak external field, the first order perturbation of the dipole moment can be approximated by

$$\boldsymbol{\mu}^{(1)}(t) \approx \boldsymbol{\mu}(t) - \boldsymbol{\mu}^{(0)}, \tag{4.27}$$

as the perturbation theory requires that lower order perturbations should yield larger contributions, such that $\boldsymbol{\mu}^{(1)} \gg \boldsymbol{\mu}^{(k)}$ for $k > 1$. The extent of many-photon transitions depends on the strength of the external field. Only one-photon transitions are expected when using weak external fields, making the first order correction nearly the sole contributor to the dipole moment

perturbation correction. For weak external fields, the linear response function may then be approximated by the Fourier transform

$$\langle\langle\hat{\boldsymbol{\mu}};\hat{V}(\omega)\rangle\rangle_{\omega+\mathrm{i}\gamma} \approx \frac{1}{2\pi}\int_{-\infty}^{\infty}\left[\boldsymbol{\mu}(t)-\boldsymbol{\mu}^{(0)}\right]e^{(\mathrm{i}\omega-\gamma)t}\ \mathrm{d}t. \tag{4.28}$$

In real-time simulations, the *induced dipole moment* given by

$$\boldsymbol{\mu}^{d,\mathrm{ind}}(t) = \boldsymbol{\mu}^{d}(t) - \boldsymbol{\mu}^{d}(t=0), \tag{4.29}$$

can give an approximation to the first order correction. As mentioned in Section 2.2, the system is initially in the unperturbed ground state, such that $\left|\Psi^{(0)}\right\rangle = |\Psi(t=0)\rangle$, meaning that $\boldsymbol{\mu}^{(0)} = \boldsymbol{\mu}(t=0)$. The linear response function in real-time simulations must be further approximated by the discrete Fourier transform

$$\langle\langle\hat{\boldsymbol{\mu}};\hat{V}(\omega)\rangle\rangle_{\omega+\mathrm{i}\gamma} \approx \boldsymbol{\mu}(\omega_j) = \frac{1}{N_t}\sum_{n=0}^{N_t-1}\boldsymbol{\mu}^{\mathrm{ind}}(t_n)e^{(\mathrm{i}\omega_j-\gamma)n\Delta t}, \tag{4.30}$$

for $j = 0, 1, \ldots, N_t/2-1$, using only dipole trajectory *after* the external field is switched off, with $t_n = (n\Delta t + t_0)$. The Fourier transform is calculated for the polarization direction d:

$$\mu^{d}(\omega_j) = \frac{1}{N_t}\sum_{n=0}^{N_t-1}\mu^{\mathrm{d,\ ind}}(t_n)e^{(\mathrm{i}\omega_j-\gamma)n\Delta t}, \tag{4.31}$$

dictated by the direction of the external field, $u_r = \delta_{d,r}$. This means that three separate calculations are needed for the full spectrum, one for each polarization direction. Although the damping $e^{-\gamma t}$ is meant to account for the finite lifetime of the excites states, it also improves discrete Fourier transform by letting the signal approach zero at $t = t_{N_t-1}$. This is because the input signal provided to the discrete Fourier transform should represent one period of the signal. Discontinuity between the start and end points of the signal causes unwanted artifacts in the frequency domain.

Inserting the new expression in Eq. (4.31) into the expression for α_{dd} in Eq. (4.32) gives the diagonal elements of the dipole polarizability tensor in real-time simulations:

$$\alpha_{dd}(\omega_j) \approx 2\pi\frac{\mu^{d}(\omega_j)}{\mathrm{F}_{\mathrm{str}}}. \tag{4.32}$$

The intensities obtained by the discrete Fourier transform depends greatly on the time domain $t \in [t_0, N_t\Delta t)$ and the lifetime parameter, γ. The normalized spectrum is therefore often used:

$$I(\omega_i) = \frac{S(\omega_i)}{\max_{\omega_j} S(\omega_j)} \tag{4.33}$$

giving an absorption spectrum with relative intensities.

The absorption spectrum as given in Eq. (4.33) is the end goal of the laser-driven real-time simulations of interest in this project. The real-time simulations are computationally heavy, and high resolution spectra requires

long simulations. This severely limits which molecules theoretical chemists are able to study, as well as reduces the practically feasible choices of basis sets and molecular electronic structure models.

This project aims to reduce the computational cost of the simulated absorption spectrum by extrapolating a short trajectory of the time dependent dipole moment. The extrapolation will exploit the regular harmonic form of the exact dipole moment, as given in Eq. (2.30). The frequencies of the dipole moment when using a weak laser field should correspond to transition energies from the stationary ground state to the excited states. This would correspond to one-photon transitions, as described by first order response theory. The fitting model will therefore also try to fit the induced dipole moment in the from of the first perturbation correction to the dipole moment, given in Eq. (4.25). It is important to note that many-photon transitions may be present in the dipole moment from the real-time simulations, and such contributions cannot be isolated. One relies on using a *sufficiently weak* laser field for the absorption spectrum to only include the one-photon transition when using real-time simulations. Calculating the transition energies is comparably expensive to the real-time simulations, and will therefore be unknown during the extrapolation of the dipole moment.

PART II

Method

CHAPTER 5

Time-Series Extrapolation

There appears to be no available research within theoretical chemistry on extrapolating molecular properties in the time domain. The approach when developing the method for extrapolating the time-dependent electric dipole moment was therefore to exploit its regular harmonic form, as shown in Eq. (2.30). The first section in this chapter will go through some of the thought process and related work leading to the proposed fitting model for the dipole moment. After this, the second section will provide a short overview of the developed fitting model.

5.1 Fitting Multi-Sinusoidal Signals

The initial proposition for this project was to use an *artificial neural network* for the dipole moment forecasting. For an introduction to neural networks, the reader is referred to the widely referenced explanations of Hastie et al.[40]. The established and currently widely popular field of machine learning has proved a powerful tool, also for molecular sciences.[41–45] Neural networks in their essence *learn* patterns from large amounts of data, and one could say that their *intelligence* is in generalization. However, neural networks struggle with precise and reliable extrapolations.[46,47]

Although the extrapolation of a regular harmonic signal may seem like an ideal problem for forecasting, the periodicity would somehow have to be embedded into the architectural structure of the neural network. This is no trivial task when the frequencies, including the number of frequencies, are unknown. I therefore turned my attention to multi-sine harmonic fitting used in signal processing.

A commonly used method is the *four parameters sine fitting* algorithm. The theory is based on the explanation by Ramos et al.[48]. The least-squares multi-harmonic fitting method creates a truncated Fourier series using the fundamental frequency ω_f, as given by

$$\tilde{y}(t) = \sum_{k=1}^{K} [A_k \cos(k\omega_f t) + B_k \sin(k\omega_f t)] + D \tag{5.1}$$

to approximate a sinusoidal target function $y(t)$. The unknown parameters A_k, B_k and D in the approximated function $\tilde{y}(t)$ constitute the elements of the

vector $\mathbf{c} = [A_1, A_2, \ldots, A_K, B_1, B_2, \ldots, B_K, D]$, found by minimizing the least squares error

$$\text{MSE} = \sqrt{\frac{1}{N_t} \sum_{n=0}^{N_t-1} \Big\{ [y(t_n) - \tilde{y}(t_n)]^2 \Big\}}, \tag{5.2}$$

measuring the error between the target function $y(t_n)$, known only on a discrete grid $t_n = n\Delta t + t_0$ for $n = 0, 1, \ldots, N_t - 1$, and its approximated function $\tilde{y}(t)$. The linear system created by the least squares problem is given by

$$\mathbf{A}(\omega_f)\mathbf{c} = \mathbf{s}, \tag{5.3}$$

where the elements in the vector $\mathbf{s}$ are the discrete values of the signal $s_n = y(t_n)$, and the matrix $\mathbf{A}(\omega_f)$ is constructed such that each row in $\mathbf{A}(\omega_f)$ fulfills the equation $[\mathbf{A}(\omega_f)]_n\mathbf{c} = \tilde{y}(t_n)$.

Estimating the fundamental frequency ω_f poses a challenge, and the initial guess is often found using an interpolated fast Fourier transform[49]. The least squares multiharmonic fitting method is therefore iterative, correcting the fundamental frequency in each iteration. The solution to the i'th iteration is given by

$$\mathbf{c}^{(i)} = [(\mathbf{A}^{(i)})^T\mathbf{A}^{(i)}]^{-1}(\mathbf{A}^{(i)})^T\mathbf{s}, \tag{5.4}$$

where $\mathbf{A}^{(i)} \equiv \mathbf{A}(\omega_f^{(i-1)})$. The fundamental frequency is updated according to

$$\omega_f^{(i)} = \omega_f^{(i-1)} + \Delta\omega_f^{(i-1)}, \tag{5.5}$$

where the change $\Delta\omega_f^{(i-1)}$ is determined by using the first derivative of $\tilde{y}(\omega_f; t)$ with respect to the fundamental frequency, $\frac{\partial\tilde{y}(\omega_f;t)}{\partial\omega_f}$.[48,50,51]

In the case of the electronic absorption spectrum, the dipole-allowed transition can in theory give a continuum of frequencies. The incomplete basis sets used in actual real-time simulations have a finite number of electronic states, and hence also a finite number of transition energies. The absorption spectrum becomes increasingly dense for larger molecules. A dense spectrum forces the fundamental frequency to be small, and consequently K will be large. The size of the linear system becomes excessive, and the majority of the frequencies $\omega_k = k\omega_f$ are not present in the dipole moment. For this reason, the developed fitting model in this project avoids the use of a fundamental frequency.

In 2009, Salinas et al.[52] implemented the multi-harmonic fitting algorithm described above using an artificial neural network. This would enforce the correct form of the output function for the dipole moment. Their work showed proof of concept on simple harmonic signals, but the accuracy of the neural network depended greatly on the method of optimization of the weight variables. Multi-harmonic fitting using neural networks encounters the same challenge of determining the fundamental frequency as when using the classical multi-harmonic fitting. At the current state of development, I can see no apparent advantage with using a neural network for fitting a noise-free (apart from numerical noise) multi-harmonic signal compared to using classical fitting methods.

There are also recursive least-square methods, like the method presented by Xu and Ding[53], avoiding the inversion of large matrices. The recursive methods

fit a single sinusoidal to the signal, determining the amplitudes of a single frequency. The determined contribution is removed from the signal, and the next frequency is fitted on the remaining residual. As the recursion progresses, the residual shrinks, giving a natural stopping criterion for the recursion. The challenge of finding the fundamental frequency remains the same. In addition, any wrongly estimated sinusoidal will cause accumulative error in all succeeding levels of recursion.

The proposed method for fitting the time-dependent dipole moment draws inspiration from the least-squares multi-harmonic fitting presented in this section. Instead of using the fundamental frequency ω_f, a method for estimating frequencies using an interpolated Fourier spectrum will be developed.

5.2 The Fitting Model for the Dipole Moment

In the chapters in the method section, the dipole moment $\mu(t_n)$ refers to the discrete values of the *induced electric dipole moment* for an arbitrary spatial coordinate obtained by real-time molecular electronic structure simulations, and $\tilde{\mu}(t)$ is its approximation. Using the form of the exact numerical dipole moment found in Eq.(2.30), the approximated function is defined as

$$\tilde{\mu}(t) = \sum_{\alpha=0}^{N_\omega - 1} \left[c_\alpha \cos(w_\alpha t) + c_{N+\alpha} \sin(w_\alpha t) \right] + c_{2N}. \tag{5.6}$$

The fitting model will estimate the frequencies $\{\omega_\alpha\}$ and the linear coefficients $\{c_i\}$ based on a short discrete dipole trajectory from the real-time simulations. The approximated dipole moment $\tilde{\mu}(t)$ is a function, and may be evaluated at any point in time. This allows for arbitrarily long extrapolations.

To simplify the notation, the approximated dipole moment is rewritten into a linear combination of a set of basis functions, as

$$\tilde{\mu}(t) = \sum_{i=0}^{2N_\omega} c_i \varphi_i(t), \tag{5.7}$$

where φ_i are the basis functions given by

$$\varphi_i(t) = \begin{cases} \cos(w_i t) & 0 \leq i < N_\omega \\ \sin(w_{i-N_\omega} t) & N_\omega \leq i < 2N_\omega \\ 1 & i = 2N_\omega \end{cases}, \tag{5.8}$$

following conventions of function approximation.[54] Determining the coefficients $\{c_i\}$ for $i = 0, 1, \ldots, 2N_\omega$ becomes a linear problem once the frequencies $\{\omega_\alpha\}$ for $\alpha = 0, 1, \ldots, N_\omega - 1$ are determined.

The proposed fitting model goes as follows:

1. **Poles of the Fourier-Padé:** Determine the complex poles $\tilde{\omega}_p$ of the interpolated Fourier spectrum, called the Fourier-Padé approximant.

2. **Estimating frequencies:** Determine the frequencies $\omega_\alpha \in \{|\tilde{\omega}_p|\}$ from the set of poles in the interpolated spectrum. The frequencies should correspond to extrema in the spectrum using real-valued ω.

3. **Linear regression:** Determine the linear coefficients using least squares fitting.

A short explanation of each step will be given below and more detailed discussions in the following chapters. In an attempt to stabilize the extraction of frequencies, the time-dependent dipole moment was decomposed into molecular orbital pairs. The fitting of each MO component $\mu_{pq}(t)$ follows the same fitting algorithm. The MO decomposition will be introduced and discussed in Chapter 9.

5.2.1 Poles of the Fourier-Padé

The frequency estimation in the fitting model will avoid the use of a fundamental frequency. Instead, all the estimated frequencies will be determined by the extrema of the Fourier-Padé approximant.

The frequencies of the dipole moment should correspond to extrema of the Fourier transform, though the spectral resolution would be too low for a direct reading of the spectral lines. The Fourier-Padé Approximant:

$$\mu(\omega) \approx [M/M]_{\mu}(\omega) = \frac{P(z(\omega))}{Q(z(\omega))} \tag{5.9}$$

offers an interpolation of the discrete Fourier transform, represented through the two polynomials $P(z)$ and $Q(z)$, where

$$z(\omega) = e^{\mathrm{i}\omega\Delta t}. \tag{5.10}$$

The frequencies will be found by examining the complex poles of the Fourier-Padé approximant with respect to z, identified as roots of $Q(z)$:

$$Q(z(\tilde{\omega}_p)) = 0. \tag{5.11}$$

The actual roots $\tilde{\omega}_p$ will be complex, but the absolute value $\omega_p = |\tilde{\omega}_p|$ of the roots close to the real axis should correspond to extrema of the interpolated spectrum. There are far more roots $\omega_p = |\tilde{\omega}_p|$ than actual frequencies in the signal. All roots are treated as prospective frequencies, but only a subset of these will be used in the approximated function, $\tilde{\mu}(t)$. There are examples in the literature of using the Fourier-Padé approximant for frequency estimation.[55,56]

In order to extract the frequencies successfully, the Fourier-Padé must converge well enough to pick up all the significant frequencies in the signals, such that the frequencies $\{\omega_\alpha\} \in \{\omega_p\}$ form a subset of the prospective frequencies. Details on the Fourier-Padé approximant and how the prospective frequencies ω_p are found will be given in Chapter 6.

5.2.2 Estimating Frequencies

The Fourier-Padé will have an excessive number of complex poles compared to the actual number of frequencies in the dipole moment. A considerable amount of the prospective frequencies ω_p are therefore redundant. The number of acceptable redundant frequencies used in the fitting is limited, as it both increases the computation time of the linear fitting and – more importantly – may cause false solutions. Any sufficiently large basis $\{\varphi_i\}$ with arbitrary

frequencies $\{\omega_\alpha\}$ will be able to interpolate a short trajectory of the dipole moment, the precision increasing as the basis grows. A well interpolated short trajectory does not however guarantee a stable extrapolation. Limiting the frequencies used for creating the basis set will therefore be essential for reliable extrapolation.

In order to separate the small subset of estimated frequencies $\{\omega_\alpha\}$ from the prospective frequencies $\{\omega_p\}$, a *clustering algorithm* will be used. The prospective frequencies will be divided into two groups, representing estimated frequencies and redundancies. This will be the topic of Chapter 7.

5.2.3 Linear Regression

For the optimization of the coefficients, the well established method of linear regression will be used. The method is presented in Chapter 8, along with details on how to evaluate the goodness of the fit. The error measure will be important if the convergence criterion is to be used for automatic termination of real-time simulations.

5.3 Implementation and Testing

The code for fitting the dipole moment was implemented in the Python programming language. The code was vectorized using NumPy[57] arrays, and all plots are generated using MatPlotLib[58].

Each of the following chapters, describing the method, will also provide a short description of implementation choices. Some unit testing and sanity checks will also be presented. For this purpose, a synthetic test signal $f(t)$ was created in the form of Eq. (5.6). The synthetic signal is given by:

$$f(t) = \sum_{i=1}^{50} \Big[A_i \cos(\omega_i t) + B_i \sin(\omega_i t) \Big], \tag{5.12}$$

with randomly generated frequencies $\omega_i \in (0, 5]$ and random amplitudes $A_i, B_i \in [-1, 1]$. All the random variables were generated using the `random` library of NumPy[57]. This function will be used for several sanity checks in the following chapters.

CHAPTER 6

The Fourier-Padé Approximant

The first step of the developed method is to determine the frequencies by examining the extrema of a Fourier-Padé spectrum. This chapter will introduce the equations of the Fourier-Padé approximant, and describe how the prospective frequencies are extracted. The implementation of the Fourier-Padé approximant will be briefly discussed, including a test case using a synthetic sinusoidal signal.

6.1 The Equations of the Fourier-Padé Approximant

The Padé approximant is used to accelerate the convergence of a truncated power series, such that the function $f(z) = \sum_{n=0}^{\infty} c_n z^n$ is approximated by

$$[M/N]_f(z) = P(z)/Q(z), \tag{6.1}$$

where $P(z)$ and $Q(z)$ are polynomials of respectively M'th and N'th degree. In the work of Bruner et al.[12], the discrete Fourier transform of the dipole moment is interpolated using a Padé approximant. The explanation of the method in this section is heavily based on their article, although the article uses a different convention for the discrete Fourier transform. Damping will also be incorporated into the Fourier-Padé equations.

Rewriting the discrete Fourier transform into a power series expansion yields

$$\mu(\omega) \propto \sum_{n=0}^{N_t-1} \mu(t_n) e^{(\mathrm{i}\omega-\gamma)n\Delta t} = \sum_{n=0}^{N_t-1} \mu(t_n) \left(e^{(\mathrm{i}\omega-\gamma)\Delta t}\right)^n, \tag{6.2}$$

where N_t is the number of time points and $\mu(t_n)$ are the discrete values from real-time calculations and $t_n = n\Delta t + t_0$. This leads to the required form of the Padé approximant, with the diagonal Padé scheme given by

$$[M/M]_\mu(z) = \frac{\sum_{k=0}^{M} a_k z^k}{\sum_{k=0}^{M} b_k z^k}, \tag{6.3}$$

where $M = (N_t - 1)/2$ and

$$z(\omega) \equiv e^{(\mathrm{i}\omega-\gamma)\Delta t}. \tag{6.4}$$

The coefficients are determined by

$$\sum_{n=0}^{N_t-1} c_n z^n = \frac{\sum_{k=0}^{M} a_k z^k}{\sum_{k=0}^{M} b_k z^k}, \tag{6.5}$$

where $c_n \equiv \mu(t_n)$. This creates the linear system

$$\sum_{n=0}^{N_t} c_n z^n \sum_{m=0}^{M} b_m z^m = \sum_{k=0}^{M} a_k z^k, \tag{6.6}$$

where convention sets $a_0 = c_0$ and $b_0 = 1$. Unless otherwise specified, the indices in the following explanation therefore run $m, k = 1, \ldots, M$. The coefficients $\{b_k\}$ are determined by solving

$$\mathbf{G}\mathbf{b} = \mathbf{d}, \tag{6.7}$$

where $\mathbf{G}$ is a $M \times M$ Toeplitz matrix and $\mathbf{d}$ is a vector of dimensionality M. Their elements are defined by

$$G_{km} = c_{M-m+k} \tag{6.8}$$

$$d_k = -c_{M+k}. \tag{6.9}$$

After determining $\{b_k\}$, the next set of coefficients $\{a_k\}$ is found by

$$a_k = \sum_{m=0}^{k} b_m c_{k-m}. \tag{6.10}$$

The resulting function $\mu(z(\omega))$ may be evaluated at any point ω, enabling arbitrary resolution to the Fourier spectrum.

The Fourier-Padé approximant can be used directly to improve the resolution of the absorption spectrum. The proposed fitting model uses the Fourier-Padé as a tool to estimate the frequencies, making the fitting method more computationally expensive compared to the Fourier-Padé alone. So why the extra work of fitting the dipole moment in the time domain? Firstly, the hope is that the fitting model can surpass the performance of the Fourier-Padé approximant. Secondly, self-evaluation of the fitting model uses quantitative measures of error in the time domain. Measuring error in the frequency domain is far less trivial, and the Fourier-Padé approximant offers no self-evaluation. Using the Fourier-Padé alone, there is no way of evaluating the error in the approximated spectrum. The fitting model will provide such an error estimate, which is the topic of Section 8.3.

It should be pointed out that determining the coefficients in $Q(z)$ requires solving a linear system, prone to near-degeneracy. Small variations in the power series coefficients $\{c_n\}$ make the calculations sensitive to numerical imprecision, potentially causing significant round-off errors in the coefficients of both $Q(z)$ and $P(z)$.[59]

6.2 Estimating Frequencies From the Complex Poles

By identifying the poles z_p of the Padé approximant in Eq. (6.5), the possible peaks of the spectrum may be identified as

$$\omega_p = |\tilde{\omega}_p| = \left| \frac{\ln(z_p)}{\mathrm{i}\Delta t} \right|, \tag{6.11}$$

where the undamped $\gamma = 0$ version is used in order to achieve higher precision in the frequencies. The poles will yield complex frequencies $\tilde{\omega}_p$, and the real ω_p should not represent singularities of the function $\mu(\omega)$, but rather extrema.

The complex poles are found by determining the roots z_p of $Q(z) = \sum_k b_k z^k$ from the Fourier-Padé, $[M/M]_\mu(z) = \frac{P(z)}{Q(z)}$. The coefficients in the polynomial $Q(z)$ will be real, as $\mu(t)$ is real. According to the complex conjugate root theorem, a polynomial with real coefficients will be mirror-symmetric with respect to the real axis. This implies that if z_q is a root of $Q(z)$, then the complex conjugate $z_{-q} = \overline{z}_q$ is also a root. Rewriting the conjugate pairs gives

$$z_q = e^{\mathrm{i}\,\mathrm{Re}(\tilde{\omega}_q)\Delta t} e^{\mathrm{Im}(\tilde{\omega}_q)\Delta t} \tag{6.12}$$

$$\overline{z}_q = \; e^{-\mathrm{i}\,\mathrm{Re}(\tilde{\omega}_q)\Delta t} e^{\mathrm{Im}(\tilde{\omega}_q)\Delta t}. \tag{6.13}$$

This shows that if $\tilde{\omega}_q = a_q + \mathrm{i}b_q$ is a root of $Q(z(\tilde{\omega}))$, then $\tilde{\omega}_{-q} = -a_q + \mathrm{i}b_q$ is also a root. All poles $\mathrm{Im}(z_p) < 0$ may be discarded, as these will simply yield duplicates among real frequencies ω_p.

A real pole z_r implies that $\tilde{\omega}_r = \mathrm{i}b_r$ is a pure imaginary number. These poles are assumed not to represent the actual frequencies in the signal. Either the root $\tilde{\omega}_r$ is far from the real axis, making it likely that it will not represent a peak in the spectra, or $\tilde{\omega}_r$ is close to zero, representing a peak corresponding to a constant in the signal. Either way, the pole should be discarded.

This reduces the number of possible frequencies to maximum $M/2$, considering only the poles $\mathrm{Im}(z_p) > 0$. The possible frequencies are then

$$\omega_p = \left| \frac{\ln(z_p)}{\Delta t} \right|, \quad \mathrm{Im}(z_p) > 0. \tag{6.14}$$

It is safe to assume that $M/2 \gg N_\omega$, where N_ω is the number of frequencies present in the signal. In order to separate the estimated frequencies from the redundant roots, a *clustering* algorithm will be used, as will be introduced in Chapter 7.

6.3 Limitations on the Frequency Domain

While the resolution of the Fourier-Padé is greatly determined by final time $T_f = N_t \Delta t$, studies have shown that the convergence depends less on the step length, Δt.[17] The time step does however set limits to the range of the frequency domain, as will be shown in this section.

For the absorption spectrum, the polynomials $P(z)$ and $Q(z)$ are only evaluated on $z(\omega) = e^{\mathrm{i}(\omega-\gamma)\Delta t}$, where ω is real and positive. The function $z(\omega)$ is periodic:

$$z(n\frac{2\pi}{\Delta t} + \omega) = z(\omega), \tag{6.15}$$

effectively making the Fourier-Padé approximant periodic.

The imaginary part of the Fourier spectra is anti-symmetric around $\omega = 0$, implying that the Fourier-Padé also is expected to be anti-symmetric, such that $\mathrm{Im}\{[M/M]_\mu(z(-\omega))\} = -\mathrm{Im}\{[M/M]_\mu(z(\omega))\}$. Since $z(\frac{2\pi}{\Delta t} - \omega) = z(-\omega)$, the spectrum is expected to also appear backwards from $\frac{2\pi}{\Delta t}$, as shown by

$$\mathrm{Im}\left\{ [M/M]_\mu(z(\frac{2\pi}{\Delta t} - \omega)) \right\} = -\mathrm{Im}\{[M/M]_\mu(z(\omega))\}. \tag{6.16}$$

In order to get a correct Fourier-Padé spectrum, it is vital to constrain the time step to $\Delta t < \pi/\omega_{\max}$, where $\omega_{\max}$ is the largest frequency in the signal. This limitation is similar to that of the regular discrete Fourier transform, where the positive frequencies are limited to $\omega_k \in [0, \pi/\Delta t)$. Unlike the Fourier-Padé, the discrete Fourier transform is not affected by any frequencies $\omega \geq \pi/\Delta t$.

6.4 Scaling the Fourier-Padé Spectrum

The Fourier-Padé spectrum approximates the *truncated discrete* Fourier spectrum. One may imagine that the Fourier-Padé spectrum approximates a discrete Fourier transform with a larger number of discrete time points N_t'. The time step Δt is hard coded into the Fourier-Padé, but the resolution is improved when $N_t' > N_t$. The discrete Fourier spectrum $\mu(\omega_j)$ where $\omega_j = j\Delta\omega$ with resolution

$$\Delta\omega = \frac{2\pi}{N_t'\Delta t'} \tag{6.17}$$

using the same time step $\Delta t' = \Delta t$ may then be approximated as

$$\mu(\omega_j) \approx \frac{1}{N_t'}[M/M]_\mu(z(\omega_j)), \tag{6.18}$$

where $M = (N_t - 1)/2$ with $N_t' > N_t$.

The spectral resolution of a discrete Fourier transform using N_t and Δt is equivalent to that of the discrete Fourier transform using $N_t' = mN_t$ and $\Delta t' = \Delta t/m$. To approximate the longer simulation using N_t' and $\Delta t'$, for $m > 1$, the Fourier Padé should be scaled according to

$$\mu(\omega_j) \approx \frac{\Delta t}{N_t'\Delta t'}\,[M/M]_\mu(z(\omega_j)). \tag{6.19}$$

A given resolution $\Delta\omega$ may then be approximated according to

$$\mu(\omega_j) \approx \frac{\Delta\omega\Delta t}{2\pi}\,[M/M]_\mu(z(\omega_j)), \tag{6.20}$$

where the rewriting mN_t is not guaranteed to be an integer. The available frequency domain of the Fourier-Padé will still be determined by the time step Δt used when creating the approximant.

6.5 Implementation and Sanity Checks

The implementation of the Fourier-Padé approximant follows the equations given above. The Toeplitz matrix $\mathbf{G}$ in Eq. (6.8) was created and its linear system in Eq. (6.7) solved using functions from SciPy[60]. The matrix inversion for solving the linear system does not exploit the symmetry in $\mathbf{G}$, as the Toeplitz solver was observed to be numerically unstable. The complex roots of $Q(z)$ were found using the NumPy[57] function for determining polynomial roots, which is based on finding the eigenvalues of the companion matrix[61] of the polynomial.

The rewriting of the damped discrete Fourier transform in Eq. (6.2) could have been chosen differently, making the damping part of the coefficients c_n instead of part of the variable $z(\omega)$. The Fourier-Padé approximant with

$c_n = \mu(t_n)e^{-\gamma n \Delta t}$ and $z(\omega) = e^{\mathrm{i}\omega\Delta t}$ is equivalent to the equations given in Section 6.1. The decision to keep the damping in $z(\omega)$ was to achieve higher flexibility in the implementation. This way, the damping is not included in the linear system. Different values for the lifetime parameter γ may then be tried out without repeating the matrix inversion.

A sanity check for the Fourier-Padé spectrum is that it should converge towards the high resolution Fourier spectrum when given a sufficiently long trajectory. Fig. 6.1 shows the performance of the Fourier-Padé approximant on the synthetic signal form Eq. (5.12). Discrete values $f(t_n)$ were evenly spaced using $\Delta t = 0.1$, using two different trajectory lengths. The Fourier-Padé spectrum using the shorter trajectory coincides well with the high resolution fast Fourier spectrum on the right part of the spectrum ($\omega > 3$), but deviated greatly on the left side of the spectrum. The Fourier-Padé spectrum using the longer trajectory becomes almost interchangeable with the high resolution fast Fourier transform.

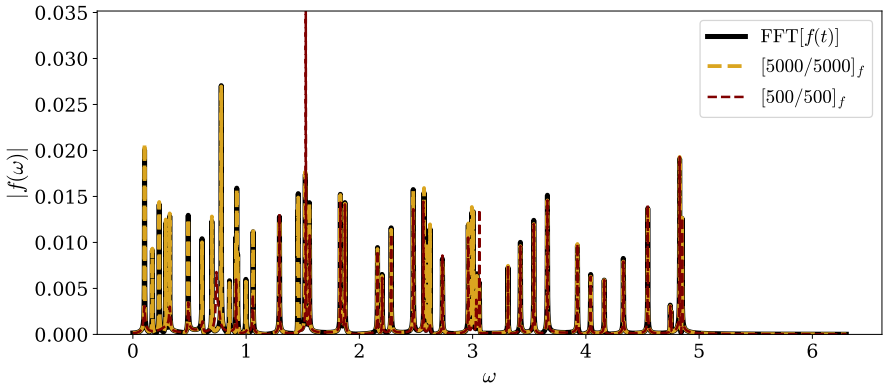

Figure 6.1: Fourier transform of the sinusoidal signal $f(t)$ from Eq. (5.12), using damping parameter $\gamma = \pi/5000$. The black line shows the fast Fourier transform using $t_n \in [0, 5000]$. The yellow and red lines show the Fourier-Padé approximants using $t_n \in [0, 1000]$ and $t_n \in [0, 100]$, respectively.

Further verification of the Fourier-Padé implementation is shown in Chapter 7, where the combination of the Fourier-Padé and cluster algorithm is used to determine the frequencies of the synthetic signal.

CHAPTER 7

K-means Clustering

The K-means clustering method falls under the category of *unsupervised machine learning*. Clustering methods divide data into clusters, aiming to minimize the variability of each cluster. Each data sample, from now on referred to as a *node*, has a position vector representing the features of the corresponding data sample. The data set may have several features, determining the dimensionality of the position vectors. Features may vary in proportions, often causing a bias in the clustering where the larger features dominate the arrangement of the clusters. To counter this, the features are typically normalized in the position vector representation.[62,63]

7.1 The K-means Algorithm

The K-means method is a fast clustering method for dividing a set of nodes into K clusters. Each cluster has a centroid, defined by the average position of all nodes in the cluster. The iterative scheme distributes all nodes among the K clusters in each iteration. The nodes are assigned to the cluster with the centroid closest to the node, using an euclidean norm to measure the distance. The positions of the centroids are then updated before the next iteration. Convergence is reached when the centroids are left unaffected by an iteration. The algorithm may be summed up by:

1. Give the centroid of each cluster an initial position.
2. Assign each node to the cluster with the closest centroid.
3. Update the value of the centroid of each cluster as the average position of all nodes in the cluster.
4. Compute the change in position of all centroids. If any centroids moved from the previous iteration; repeat steps 2.- 4.
5. Convergence has been reached, and the final clusters are given as output.

The method suffers from several limitations. The K-means method is non-deterministic in that it may yield different results depending on the initial values of the centroids. The clusters may not make complete sense if the number of clusters K is not well suited for the data set. Methods like *hierarchical clustering* do not suffer from these deficiencies, but would considerably increase the computational cost of the clustering.[62,63]

7.2 Creating Features

The nodes in this case would be the roots ω_p, and the clustering will be binary ($K = 2$), as the root will either be classified as a frequency ω_α or a redundancy ω_β. The value of the root is in itself irrelevant for the classification. Some relevant features for the classification must therefore be constructed.

Given that the Fourier-Padé has converged, the roots $\tilde{\omega}_p = \frac{\ln(z_p)}{\mathrm{i}\Delta t}$ not corresponding to an actual frequency should have a relatively large imaginary component. This should have two consequences. Firstly, none of the estimated real roots ω_p will be actual roots of the polynomial, meaning that $Q(z(\omega_p)) \neq 0$. The size of $Q(z(\omega_p))$ may serve as an indicator of how likely ω_p corresponds to a redundant frequency, assuming that $Q(z(\omega_p))$ will be larger for redundant frequencies. Secondly, the intensity of the Fourier-Padé $[M/M]_\mu(z(\omega_p))$ will serve as an indicator of how likely ω_p corresponds to an actual frequency in the signal. Each root ω_p is assigned two features, the intensity $[M/M]_\mu(z(\omega_p))$ and the polynomial value, $Q(z(\omega_p))$.

Both features will have quite extreme scaling, as they approach infinity for $[M/M]_\mu(z(\tilde{\omega}_p))$ and zero for $Q(z(\tilde{\omega}_p))$ for the complex roots $\tilde{\omega}_p$. In order to smooth out the differences, the common logarithm is used on the features. The features are then scaled from 0 to 1. The position vector of node q, is then $\mathbf{r}^q = (r_x^q, r_y^q)$ with elements given by

$$r_x^q = \frac{X(\omega_q) - \min_p \left[X(\omega_p)\right]}{\max_p \left[X(\omega_p)\right] - \min_p \left[X(\omega_p)\right]} \tag{7.1}$$

$$r_y^q = \frac{Y(\omega_q) - \min_p \left[Y(\omega_p)\right]}{\max_p \left[Y(\omega_p)\right] - \min_p \left[Y(\omega_p)\right]}, \tag{7.2}$$

where the unnormalized features are defined as

$$X(\omega_q) = \log_{10} \left|[M/M]_\mu(z(\omega_q))\right| \tag{7.3}$$

$$Y(\omega_q) = \log_{10} \left|Q(z(\omega_q))\right|. \tag{7.4}$$

The initial position of the centroid of the redundant root cluster is set to $c_0^\beta = (0, 1)$, while the initial position of the centroid of the estimated frequency cluster is set to $c_0^\alpha = (1, 0)$.

7.3 Implementation and Sanity Checks

The clustering algorithm was implemented according to the details above.

The example in Fig. 7.1 serves as a sanity check for the implementation of both the Fourier-Padé approximant and the clustering algorithm. The figure shows the clustering of the potential frequencies of the synthetic signal $f(t)$ from Eq. (5.12). The relative distances in the plot correspond to how the clustering algorithm will *see* the features, ignoring the numbers on the axes.

The clustering algorithm successfully separates all 50 frequencies in $f(t)$. The maximum absolute error of the determined frequencies was 10^{-12}. This example validates the implementation, as the Fourier-Padé approximant achieves high precision in the frequency estimation, and the clustering algorithm is successful in the separation of the actual frequencies.

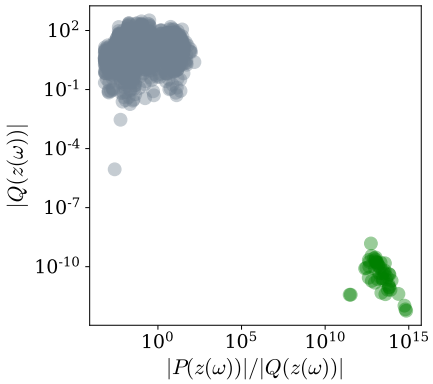

Figure 7.1: Clustering of $\omega_p = |\tilde{\omega}_p|$ where $Q(z(\tilde{\omega}_p)) = 0$. Estimated frequencies ω_α are marked in green, while redundant roots ω_β are marked in gray.

CHAPTER 8

Linear Regression

Once the frequencies for the basis functions $\varphi_i(t)$ in Eq. (5.8) have been estimated, the linear coefficients $\{c_i\}$ in

$$\tilde{\mu}(t) = \sum_{i=0}^{2N_\omega} c_i \varphi_i(t) \tag{8.1}$$

are determined using *linear regression*. An implementation choice should be pointed out before the equations are introduced. The approximated dipole moment $\tilde{\mu}(t)$ was not approximated as $\tilde{\mu}(t) \approx \mu(t)$, but rather as $\tilde{\mu}(t) \approx \mu(t+t_0)$. The change in the phase is baked into the coefficients, and should not alter the general form of the dipole moment in Eq. (2.30). The results are slightly different when approximating $\tilde{\mu}(t) \approx \mu(t + t_0)$ versus $\tilde{\mu}(t) \approx \mu(t)$, and the initial observation was that the fitting model was marginally better when using $\tilde{\mu}(t) \approx \mu(t + t_0)$. This was however not extensively tested, but changing it back to $\tilde{\mu}(t) \approx \mu(t)$ in the future is a trivial implementation detail.

The problem will be rewritten into a linear equation

$$\mathbf{Ac} = \boldsymbol{\mu'}, \tag{8.2}$$

where $\boldsymbol{\mu'}$ is a vector of dimensionality N_t with elements

$$[\boldsymbol{\mu'}]_n = \mu(t_n), \tag{8.3}$$

corresponding to data points from the real-time simulations at $t_n = n\Delta t + t_0$. The vector $\mathbf{c}$ is of dimensionality $(2N_\omega+1)$ and contains the unknown coefficients c_i. The matrix $\mathbf{A}$ is a $N_t \times (2N_\omega + 1)$ matrix with elements

$$A_{ni} = \varphi_i(n\Delta t), \tag{8.4}$$

such that each row contains all the basis functions of $\tilde{\mu}(t_n)$ evaluated at a given time, t_n. All the N_t linear equations are in the form

$$[\mathbf{A}]_n \mathbf{c} = [\boldsymbol{\mu'}]_n, \tag{8.5}$$

where the number of equations N_t is much larger than the number of unknowns, $(2N_\omega + 1)$. The linear equations try to solve

$$\sum_{i=0}^{2N_\omega} \varphi_i(n\Delta t) c_i = \mu(t_n), \tag{8.6}$$

making each linear equation in the system try to solve $\tilde{\mu}(n\Delta t) = \mu(t_n)$ for all N_t available time points. This will not be achieved ($\tilde{\mu}(n\Delta t) \neq \mu(t_n)$), as the estimated frequencies will introduce an error. The linear regression will always use the induced dipole moment, but the regular dipole moment is easily approximated by adding $\mu^d(t=0)$ to the constant c_{2N_ω}.

The linear regression optimizes the coefficients by minimizing the *mean square error*:

$$R(\mathbf{c}) = \sum_{i=0}^{N_t-1} \left[\mu(t_n) - \sum_{i=0}^{2N_\omega} \varphi_i(n\Delta t) c_i \right]^2 = \sum_{i=0}^{N_t-1} \left[\mu(t_n) - \tilde{\mu}(n\Delta t) \right]^2, \tag{8.7}$$

known as the *cost function*. The cost function measures the difference between the *true* discrete values of the dipole moment $\mu(t_n)$ obtained by the real-time simulations and the approximated dipole moment, $\tilde{\mu}(t_n)$. This chapter includes a short description of the well established least squares method, as well as explaining the chosen measure of error in the approximated function. The explanation of the regression methods in this chapter is based on those of Hastie et al.[64,65] and Géron[66].

8.1 Ordinary Least Squares Method

The ordinary least squares method (OLS) aims to minimize the cost function, which in matrix form is given by

$$R(\mathbf{c}) = (\boldsymbol{\mu}' - \mathbf{A}\mathbf{c})^\intercal (\boldsymbol{\mu}' - \mathbf{A}\mathbf{c}). \tag{8.8}$$

The cost function is minimized with respect to $\mathbf{c}$. Writing out the differentiation of the cost function gives

$$\frac{\partial R(\mathbf{c})}{\partial \mathbf{c}} = 2\mathbf{A}^\intercal (\boldsymbol{\mu}' - \mathbf{A}\mathbf{c}). \tag{8.9}$$

The minimum of the cost function is found by setting the derivative to zero, creating the optimization criterion

$$\mathbf{A}^\intercal \boldsymbol{\mu}' = \mathbf{A}^\intercal \mathbf{A}\mathbf{c}. \tag{8.10}$$

The SVD of the $N_t \times (2N_\omega + 1)$ *real* matrix $\mathbf{A}$ is given by

$$\mathbf{A} = \mathbf{U}\mathbf{D}\mathbf{V}^\intercal, \tag{8.11}$$

where $\mathbf{U}$ is an $N_t \times (2N_\omega + 1)$ orthonormal matrix, $\mathbf{D}$ is a real positive diagonal $(2N_\omega + 1) \times (2N_\omega + 1)$ matrix and $\mathbf{V}$ is another orthonormal matrix, also of dimensionality $(2N_\omega + 1) \times (2N_\omega + 1)$. The coefficient vector is given by

$$\begin{aligned} \mathbf{c} &= (\mathbf{A}^\intercal \mathbf{A})^{-1} \mathbf{A}^\intercal \boldsymbol{\mu}' \\ &= ((\mathbf{U}\mathbf{D}^\intercal \mathbf{V}^\intercal)^\intercal \mathbf{U}\mathbf{D}\mathbf{V}^\intercal)^{-1} (\mathbf{U}\mathbf{D}\mathbf{V}^\intercal)^\intercal \boldsymbol{\mu}'. \end{aligned} \tag{8.12}$$

Since $\mathbf{U}$ and $\mathbf{V}$ are orthogonal matrices, then it follows that $\mathbf{U}^{-1} = \mathbf{U}^\intercal$ and $\mathbf{V}^{-1} = \mathbf{V}^\intercal$. The relation $\mathbf{D}^\intercal = \mathbf{D}$ also holds since $\mathbf{D}$ is symmetric diagonal. Using this, the expression becomes

$$\begin{aligned} \mathbf{c} &= (\mathbf{V}\mathbf{D}\mathbf{U}^\intercal \mathbf{U}\mathbf{D}\mathbf{V}^\intercal)^{-1} \mathbf{V}\mathbf{D}\mathbf{U}^\intercal \boldsymbol{\mu}' \\ &= (\mathbf{V}\mathbf{D}^2\mathbf{V}^\intercal)^{-1} \mathbf{V}\mathbf{D}\mathbf{U}^\intercal \boldsymbol{\mu}' \\ &= \mathbf{V}\mathbf{D}^{-2}\mathbf{V}^\intercal \mathbf{V}\mathbf{D}\mathbf{U}^\intercal \boldsymbol{\mu}', \end{aligned} \tag{8.13}$$

giving the final expression for the coefficient vector:

$$\mathbf{c} = \mathbf{V}\mathbf{D}^{-1}\mathbf{U}^{\intercal}\boldsymbol{\mu}'. \tag{8.14}$$

This way, the matrix $\mathbf{A}^{\intercal}\mathbf{A}$ can then be inverted despite potential singularity.

8.2 LASSO Regression

The *least absolute shrinkage and selection operator (LASSO)* method determines the linear coefficients according to

$$\text{argmin}_{\mathbf{c}} \left\{ \frac{1}{2} R(\mathbf{c}) + \lambda \sum_{i=0}^{2N_\omega} |c_i| \right\}, \tag{8.15}$$

where $\lambda \geq 0$ *shrinks* the parameters $\mathbf{c}$. The LASSO method has no closed form for $\mathbf{c}$, and the solution is found iteratively. The shrinkage parameter λ generally makes the LASSO method less prone to over-fitting compared to OLS.

The expected form of the induced dipole moment according to linear response theory has negative cosine coefficients and positive sine coefficients, as seen in Eq. (4.25). The time step used in all calculations in this project was $\Delta t = 0.01$, and the largest molecule was the water molecule. We therefore expect none of the frequencies to be large enough to alter the sign of the coefficients, as discussed in Section 4.3.

The sampling of the dipole moment started at $t_0 = 2\Delta t$. The approximated dipole moment according to the linear response theory was therefore fitted according to

$$\begin{aligned} \tilde{\mu}(t) &\approx [\mu^d]^{(1)}(t + t_0) = [\mu^d]^{(1)}(t + 2t_p) = \sum_{n \neq 0} B_n \sin(\omega_{n0}(t + t_p)) \\ &= \sum_{n \neq 0} \Big\{ [B_n \sin(\omega_{n0} t_p)] \cos(\omega_{n0} t) + [B_n \cos(\omega_{n0} t_p)] \sin(\omega_{n0} t) \Big\}, \end{aligned} \tag{8.16}$$

since $t_p \approx \Delta t$. This alters the sign of the cosine coefficient, making both the sine and cosine coefficients positive. The non-linearity of the LASSO method enables extra constraints on the coefficients. The LASSO method can therefore be used to find the solution under the constraint

$$c_i \geq 0, \tag{8.17}$$

for both the sine and the cosine coefficients, $i = [0, 2N_\omega)$. Adding additional constraints on the optimization could minimize the potential for false solutions, given that the imposed form is correct. The LASSO method will therefore be used to force the induced dipole moment in the linear response form seen in Eq. (4.25).

8.3 Measure of Error

In order to evaluate the fitting, the available trajectory is divided into a fitting set and a (smaller) verification set. The verification data is used to ensure that

the approximated function is not over-fitted. The need for such division of the data is illustrated in Fig. 8.1, where the function $f(t)$ from Eq. (5.12) is fitted. The least squares method was provided with all frequencies in $f(t)$, but with a random error $\delta\omega \in [-10^{-3}, 10^{-3}]$ added to each frequency. Since the error in the estimated frequencies is unknown when fitting the dipole moment, the error must be measured in the time domain. The linear coefficients of the

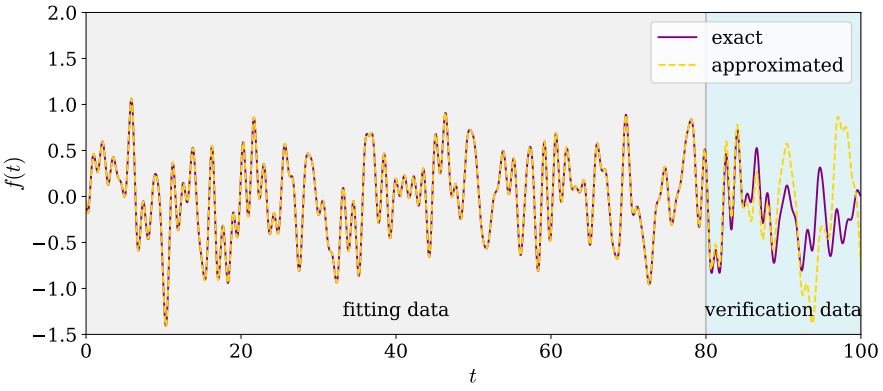

Figure 8.1: The purple line shows the true function $f(t)$ from Eq. (5.12), while the yellow dashed line shows the approximated function $\tilde{f}(t)$. The fitting data is marked with gray background, and the verification data is marked with blue background.

approximated function $\tilde{f}(t)$ were determined by OLS using discrete values of $f(t_n)$ on $t_n \in [0, 80]$, called the *fitting domain*. As seen in Fig. 8.1, $\tilde{f}(t)$ is indistinguishable from the true function $f(t)$ on the fitting domain, achieving good *interpolation*. The *extrapolation* on the *verification domain* $t_n \in (80, 100]$ shows that $\tilde{f}(t)$ is a poor approximation to $f(t)$ when evaluated outside of the fitting domain. The error in the frequencies was masked by over-fitting on the small fitting domain. With the short fitting trajectory, the method succeeds in reproducing the *known* values used for the fitting, but fails at extrapolation. The goal of the fitting model is to achieve long and accurate extrapolation of the dipole moment from short real-time simulations. Dividing the available dipole data into fitting data and verification data is therefore necessary to avoid over-fitting, as the error in the estimated frequencies will be unknown.

The coefficient of determination is used to determine the goodness of a fit. The coefficient is given by

$$R^2 = 1 - \frac{\sum_n [y_n - g(t_n)]^2}{\sum_n [y_n - \bar{y}]^2}, \tag{8.18}$$

where y_n is observed data, with $\bar{y}$ being the mean value and $g(t)$ is the function fitted on the data. The observed data in the fitting model will be the true dipole moment from the real-time simulations $y_n \equiv \mu(t_n)$ and the fitted function is the approximation $g(t_n) \equiv \tilde{\mu}(n\Delta t)$. The coefficient of determination has a range $R^2 \in [1, 0]$, where $R^2 = 1$ is a perfect fit.[67] A measure of error may therefore

be $1 - R^2$, and the measure of error in the fitting of the dipole moment will be

$$E = \frac{\sum_n \left[\mu(t_n) - \tilde{\mu}(n\Delta t)\right]^2}{\sum_n \left[\mu(t_n) - \bar{\mu}\right]^2}. \tag{8.19}$$

The most important error measure will be the error seen in the verification domain, $t_n \in (T_{\text{fit}}, T_{\text{ver}}]$, as the error in the fitting domain $t_n \in [t_0, T_{\text{fit}}]$ can be artificially low due to over-fitting. The convergence of the fitting model must be based on the error on the verification data, as doing the heavy real-time molecular electronic structure simulations to verify the approximated function would defeat the purpose of the fitting model.

During development of the fitting model, long real-time simulations are required for benchmarking. The goal is to find a convergence criterion based on the verification data which ensures that a long extrapolation will be stable and accurate. Finding such a convergence criterion would enable automatic termination of future real-time simulations of the absorption spectrum. At predetermined time intervals, the fitting model would try to fit the dipole moment and evaluate the error in the approximation. The real-time dipole trajectory length would increase until the error of the fitting model is below the convergence criterion. The real-time simulations would then be terminated, and the absorption spectrum would be calculated by extrapolating the approximated dipole moment, $\tilde{\mu}(t)$.

8.4 Implementation and Sanity Checks

The implementation of the ordinary least squares fitting is implemented as explained in Section 8.1, using the SVD function from NumPy[57]. The LASSO method uses the implementation from SciKit-learn[68].

To test the implementation, the error of the approximated function $\tilde{f}(t)$ of the synthetic signal from $f(t)$ Eq. (5.12) was studied as a function of different trajectory lengths. The approximated function $\tilde{f}(t)$ was fitted using OLS and the exact frequencies of $f(t)$, using the same step length $\Delta t = 0.01$ in all cases. The error was measured as $1 - R^2$, where R^2 was computed on the time domain $t \in [0, 4000)$, using the time step $\Delta t = 1/3$. The result is shown in Fig. 8.2. The error quickly converges towards numerical zero, validating the correctness of the implementation of the least-squares algorithm.

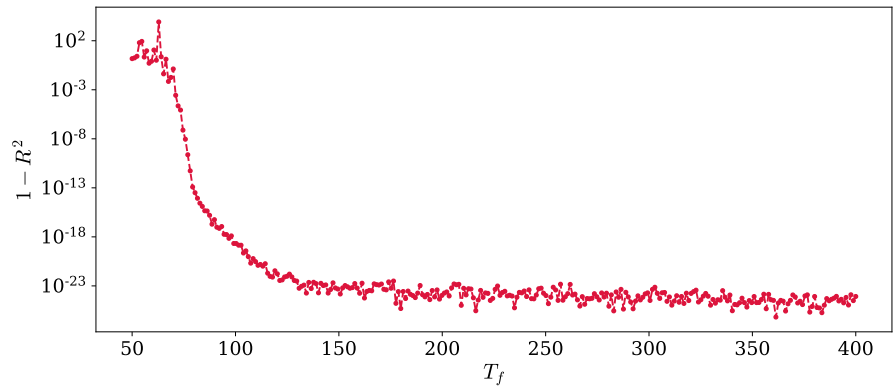

Figure 8.2: Error between approximated function $\tilde{f}(t)$ and target function $f(t)$ as a function of different fitting domains $t \in [0, T_f]$. The exact frequencies were used in the least square fitting.

CHAPTER 9

Molecular Orbital Decomposition of the Dipole Moment

In 2016, Bruner et al.[12] used a diagonal Padé approximant $[M/M]_{\mu^d}$ to accelerate the convergence of the discrete Fourier transform of the dipole moment obtained from *real-time time-dependent density functional theory (RT-TDDFT)*. The Padé approximant struggles with dense spectra. To counter this, Bruner et al. used an occupied-virtual molecular orbital decomposition of the dipole moment, as originally proposed by Repisky et al.[13,14]. The dipole moment was decomposed into

$$\mu^d(t) = \sum_{ia} \mu^d_{ia}(t) \tag{9.1}$$

where i indexes occupied orbitals and a indexes the virtual orbitals. The Padé approximant was determined for each component $\mu^d_{ia}(t)$, creating many, but sparser spectra. The linearity of the Fourier transform allows to write the total spectrum as $\mathcal{F}[\mu^d(t)] = \sum_{ia} \mathcal{F}[\mu^d_{ia}(t)]$. According to Bruner et al., this reduced the simulation time five- to seven-fold compared to the regular fast Fourier transform.

The MO decomposition will also be used in this project, with hopes of simplifying the fitting of the dipole moment. The description of the MO pair decomposition below follows the same idea, though it is rewritten to suit the RT-TDCC framework.

9.1 Decomposition in Coupled Cluster Theory

The dipole moment in the real-time simulations is calculated according to

$$\mu^d(t) = \mathrm{Tr}\big[\mathbf{P}^d\mathbf{D}(t)\big] = \sum_p [\mathbf{P}^d\mathbf{D}(t)]_{pp}, \tag{9.2}$$

where p is a general orbital index, $\mathbf{P}^d$ is the transition dipole matrix for the direction of interest and $\mathbf{D}(t)$ is the time dependent density matrix, given in the MO basis. The diagonal of the product $\mathbf{P}^d\mathbf{D}(t)$ will be

$$[\mathbf{P}^d\mathbf{D}(t)]_{pp} = \sum_q P^d_{pq} D_{qp}(t), \tag{9.3}$$

summing over all orbitals, ψ_q. The dipole moment is decomposed into MO pairs, including all unique pairs and the diagonal:

$$\mu^d_{pq}(t) = P^d_{pq} D_{qp}(t) + P^d_{qp} D_{pq}(t) \tag{9.4}$$

$$\mu^d_{pp}(t) = P^d_{pp} D_{pp}(t). \tag{9.5}$$

The full dipole moment is the sum over all components, as given by

$$\mu^d(t) = \sum_{p \leq q} \mu^d_{pq}(t). \tag{9.6}$$

The decomposition of the induced dipole moment is similarly given as

$$\mu^{d,\mathrm{ind}}(t) = \sum_{p \leq q} \mu^{d,\mathrm{ind}}_{pq}(t), \tag{9.7}$$

where the components of the decomposed induced dipole moment are given by

$$\mu^{d,\mathrm{ind}}_{pq}(t) = \mu^d_{pq}(t) - \mu^d_{pq}(t=0). \tag{9.8}$$

The decomposition serves two purposes. Firstly, by decomposing the dipole moment we hope to simplify the fitting of the dipole moment. The separate dipole components in RT-TDDFT yielded several, but simpler spectra compared to the full dipole moment. The hope is that the decomposition in RT-TDCC theory will give a similar simplification. Secondly, the decomposition may enable us to determine which orbital transitions contribute to the different peaks in the absorption spectrum.

9.2 Similarity Measure Between Components

The decomposition of the dipole moment poses difficulties with memory load, as the memory usage for the decomposed dipole moment scales with $N_p(N_p+1)/2 \times N_t$, where N_t is the number of time points N_p is the number of molecular orbitals. The memory demand grows fast for both larger molecules as well as for larger basis sets. This problem was addressed by Ghosh et al.[16], where they used a reduced MO space decomposition, effectively reducing the memory cost of the real-time dynamics simulation. Ghosh et al. chose to divide the molecular orbitals into groups based on their orbital energy.

An interesting question could therefore be how to cluster the components of the dipole moment in CC theory. Should the decomposition prove beneficial for the function fitting, the number of components will quickly grow vast for larger systems. Studying similarities between the components may reveal suitable groupings.

The similarity between two components can be defined by their normalized correlation, commonly used to determine the similarity between two oscillating signals in signal processing.[69] The similarity is given by

$$r_{pq,rs} = \frac{\sum_n \mu^{d,\mathrm{ind}}_{pq}(t_n)\mu^{d,\mathrm{ind}}_{rs}(t_n)}{\sqrt{\left(\sum_n [\mu^{d,\mathrm{ind}}_{pq}(t_n)]^2\right)\left(\sum_n [\mu^{d,\mathrm{ind}}_{rs}(t_n)]^2\right)}}, \tag{9.9}$$

where $r_{pq,rs} \in [-1, 1]$. If $r_{pq,rs} = 1$, then the two signals are completely equivalent, differing possibly only in magnitude. If $r_{pq,rs} = -1$, then the signals are anti-parallel. In order to find patterns in the similarity between the components of the dipole moment, a recursive algorithm was created to cluster similar components:

1. Decide a tolerance parameter ϵ.
2. Select an unassigned component. $\mu_{pq}^{d,\text{ind}}$
3. Create new cluster for $\mu_{pq}^{d,\text{ind}}$.
4. Mark $\mu_{pq}^{d,\text{ind}}$ as assigned.
5. For each unassigned component $\mu_{rs}^{d,\text{ind}}$:
   a) If $r_{pq,rs} \geq (1 - \epsilon)$:
      i. Add $\mu_{rs}^{d,\text{ind}}$ to the cluster of $\mu_{pq}^{d,\text{ind}}$.
      ii. Mark $\mu_{rs}^{d,\text{ind}}$ as assigned.
      iii. Recursive call to point 5.
6. If any components are unassigned: go back to point 2.

This way the components will form groups where $\mu_{pq}^{d,\text{ind}}$ will be similar within the tolerance parameter $r_{pq,rs} \geq (1 - \epsilon)$ to at least one other component $\mu_{rs}^{d,\text{ind}}$ in its group. All components in the same group will be similar if the tolerance parameter is small.

9.3 Implementation and Sanity Checks

Several of the MO pairs will not contribute to the dipole moment and should be excluded from the simulations to avoid unnecessary memory usage. Redundant pairs were identified by finding the zero-elements in the symmetric transition matrix $\mathbf{P}^d$. The stored components μ_{pq}^d were therefore restricted to $p \leq q$ and $|P_{pq}^d| = |P_{qp}^d| < \delta$ for a positive infinitesimal δ. Storing the components followed the idea of sparse matrix representation.

Some testing of the implementation of the MO decomposition of the dipole moment is included in Section 10.1.1.

PART III

Results, Discussion and Conclusion

CHAPTER 10

The Coupled Cluster Calculations and Parameter Studies

The first part of this chapter contains the simulation details of the RT-TDCCSD calculations used to obtain the dipole data for testing the fitting model. The second part contains a small parameter study of the fitting model, which will motivate choices of the size of the verification window used for the fitting of the dipole moment presented in later chapters.

10.1 Simulation Details

The dipole moment of all systems was obtained using RT-TDCCSD calculations using the implementation of Pedersen et. al[33,70]. The external field used in all simulations was

$$\mathrm{F}(t) = \begin{cases} 10^{-3} & \text{if } \ 0 < t \leq \Delta t \\ 0 & \text{else} \end{cases}, \tag{10.1}$$

where $t_p = \Delta t = 0.01$ a.u. and the field strength was $\mathrm{F}_{\mathrm{str}} = 10^{-3}$ a.u.. The polarization direction was z, such that $\mathbf{u} = (0, 0, 1)$. The calculated dipole moment was therefore $\mu^z(t)$ for all systems, which was sampled from $t_0 = 2\Delta t$.

All three spatial directions are needed for a complete absorption spectrum. Still, only the z-direction will be discussed in this project, as the fitting method is equivalent in all three directions. The assumption is that the fitting of the three spatial coordinates should be similar in difficulty, and it was therefore prioritized to include a few more atoms/molecules and a wider variety of studies rather than to compute the dipole moment for all spatial directions for each system.

Two different atoms, both placed at the origin, will be part of the study. These are the helium atom and the beryllium atom. The molecules in the study will be the hydrogen molecule, lithium hydride and the water molecule. The nuclei of the hydrogen atoms in the hydrogen molecule are placed at $(0, 0, 0)$ a_0 and $(0, 0, 1.4)$ a_0. In lithium hydride, the lithium nucleus is placed at $(0, 0, 0)$ a_0 and the hydrogen nucleus at $(0, 0, 3.08)$ a_0. Lastly, the nucleus of the oxygen atom in the water molecule is placed at $(0, 0, -0.1239093563)$ a_0 and the nuclei of the two hydrogen atoms are placed at $(0, 1.4299372840, 0.9832657567)$ a_0 and $(0, -1.4299372840, 0.9832657567)$ a_0.

All simulations used *augmented correlation-consistent polarized valence basis sets*[71], and the basis sets were obtained from PySCF[72]. The closed-shell

restricted Hartree-Fock ground state, used as reference state, was computed with a tolerance parameter $\epsilon = 10^{-10}$ for all systems. The molecular orbital energies are listed in Table A.1 in Appendix A. The point group symmetry was not imposed on the wave function in the calculations. The reference states and orbital integrals were computed using either PySCF[72] or Dalton[73]. Specifics for each atom or molecule are given in Table 10.1. The vode integrator comes

Table 10.1: Details on the RT-TDCCSD simulations.

	basis set	**integrator**	**background**
He	aug-cc-pVTZ	Gauss	Dalton
H_2	aug-cc-pVTZ	vode	PySCF
Be	aug-cc-pVTZ	Gauss	Dalton
LiH	aug-cc-pVDZ	Gauss	Dalton
H_2O	aug-cc-pVDZ	vode	PySCF

from SciPy[60], while the symplectic Gauss-Legendre integrator is as described by Pedersen and Kvaal[33].

10.1.1 Molecular Orbital Decomposition

The decomposition stored all dipole moment components where $|P^d_{pq}| > 10^{-10}$. A measure of the sparsity of the MO decomposition could be given as

$$s_\delta = \frac{N_{pq} - N_\delta}{N_{pq}}, \tag{10.2}$$

where N_δ is the number of MO pairs stored when using the threshold δ, and $N_{pq} = N_p(N_p + 1)/2$ is the number of unique MO pairs of the orbital basis of size N_p. The sparsity of each studied system is given in Table 10.2.

To test the implementation of the MO decomposition, a measure of error was defined on the discrete time domain as

$$E_{\mathrm{MO}} = \max_n |\operatorname{Tr}\left[\mathbf{P}^d\mathbf{D}(t_n)\right] - \sum_{p\leq q} \mu^d_{pq}(t_n)|, \tag{10.3}$$

measuring the maximum deviation between the full dipole moment and the sum over the non-trivial components of the dipole moment. The errors in the MO decomposition of the studied systems are given in Table 10.2. The decomposed

Table 10.2: Error in MO decomposition. The error measure E_{MO} as defined in Eq. (10.3). The sparsity s_δ of the MO decomposition is given in Eq. (10.2) using $\delta = 10^{-10}$.

	E_{MO} [a.u.]	s_δ
He	$3.0 \cdot 10^{-20}$	0.89
H_2	$4.8 \cdot 10^{-14}$	0.82
Be	$3.0 \cdot 10^{-19}$	0.92
LiH	$9.8 \cdot 10^{-15}$	0.70
H_2O	$1.3 \cdot 10^{-15}$	0.67

dipole moment replicates the full dipole moment to machine precision.

10.2 Parameter Study

This section presents a few small scale parameter studies regarding the choice of time step Δt used in the Fourier-Padé when estimating the frequencies and the size of the verification window used when optimizing the linear coefficients. The studies motivate the parameter choices made in the succeeding chapters. Several of the studies in this chapter are based on observations made during the development of the method. The number of available test systems during this project was limited, though some parameter trends were still apparent. These trends are illustrated using example systems.

10.2.1 The Periodicity of the Fourier-Padé Approximant

As discussed in Section 6.3, the Fourier-Padé approximant should be periodic. This study uses Helium as an example system, and details about the simulation are found in Section 10.1. The absorption spectrum of Helium with $\gamma = \frac{\pi}{6000}$ was used to verify the periodicity, as shown in Figs. 10.1 and 10.2. The fast Fourier transform was calculated using the time domain $t_n \in [t_0, 6000 \text{ a.u.}]$, using $\Delta t = 0.01$ a.u. and $t_0 = 0.02$ a.u.. The Fourier-Padé approximant was calculated using the dipole moment values on the time domain $t_n \in [t_0, 1000 \text{ a.u.}]$, using different time steps in Figs. 10.1 and 10.2.

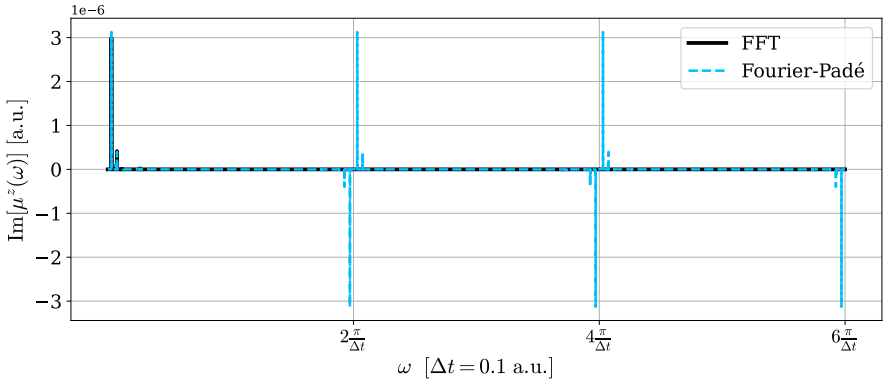

Figure 10.1: Comparing $\mu^z(\omega)$ of He, using fast Fourier transform (black line) and a Fourier-Padé approximant (blue line). The x-axis is shown relative to the time step $\Delta t = 0.1$ a.u. used for the Fourier-Padé approximant.

The Fourier-Padé spectra of Helium in Figs. 10.1 and 10.2 show the periodicity and anti-symmetry as expected from the discussion in Section 6.3. Fig. 10.1 displays three cycles, with the expected cycle length from Eq. (6.15) of $2\pi/\Delta t$. The Fourier-Padé approximant in Fig. 6.1 also displays the anti-symmetric behavior $\mathrm{Im}\{[M/M]_\mu(z(\frac{2\pi}{\Delta t} - \omega))\} = -\mathrm{Im}\{[M/M]_\mu(z(\omega))\}$, creating additional and unwanted peaks in the spectrum.

The example shown is a constructed illustration, where the time step is set to very a large value in order to see the possible effects from limitations in the frequency domain of the Fourier-Padé approximant. The upper bound of the

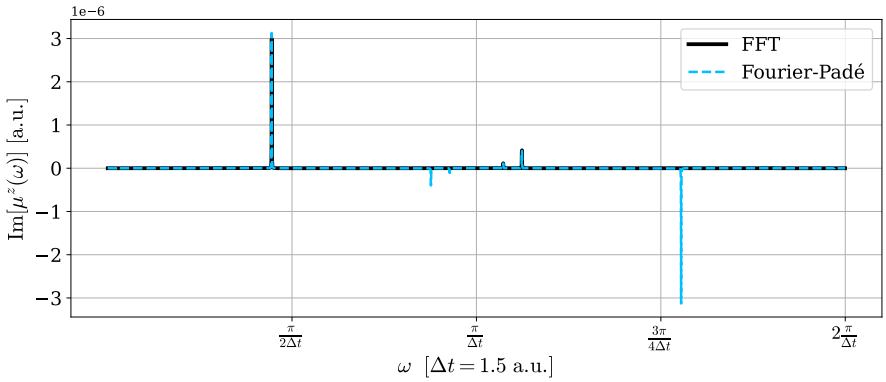

Figure 10.2: Comparing $\mu^z(\omega)$ of He, using fast Fourier transform (black line) and a Fourier-Padé approximant (blue line). The x-axis is shown relative to the time step $\Delta t = 1.5$ a.u. used for the Fourier-Padé approximant.

time step should however be kept in mind when dealing with larger systems, where long simulations are required for the Fourier-Padé to converge.

10.2.2 Frequency Convergence and the Time Domain

The visual table in Fig. 10.3 explores the relationship between the time domain used for the Fourier-Padé approximant and the success of the frequency estimation, using lithium hydride as the example molecule. Simulation details are found in Section 10.1. The ordinary least squares fitting used the exact same long dipole trajectory in all cases to limit the difference in error introduced by the fitting. The error in all Figs. 10.3 to 10.6 was calculated on the time domain $t_n \in [t_0, 8000 \text{ a.u.}]$ where $t_0 = 0.02$ a.u., using $\Delta t = 0.01$ a.u., measuring the error on the fitting domain as well as for a longer extrapolation. There is a clear trend in Fig. 10.3 of the error decreasing when the time domain $t_n \in [t_0, T_f]$ is increased for estimating the frequencies. The error seems to be quite unaffected by the step length, Δt. This coincides well with the findings of Mattiat and Luber[17], who published on Padé accelerated Raman spectra computed using RT-TDDFT, where they provided an analysis of the performance of the Fourier-Padé approximant. They found that the convergence depends more on the propagation time T_f than the step length Δt. This is in good agreement with the findings in Fig. 10.3, where the error trends also stem from convergence, or lack thereof, of the Fourier-Padé approximant when searching for the frequencies.

The same study was repeated, results shown in Fig. 10.4, this time using the same time domain for the fitting as for the frequency estimation. The estimated frequencies are the same for the studies shown in Figs. 10.3 to 10.6, differing only in the linear coefficients in $\tilde{\mu}^z(t)$. Note that the colors in Figs. 10.3 to 10.6 use the same scaling. The error in Fig. 10.4 is very similar to that in Fig. 10.3, suggesting that the error in the approximated dipole moment in these two studies primarily stems from the frequency estimation, and not from the linear fitting.

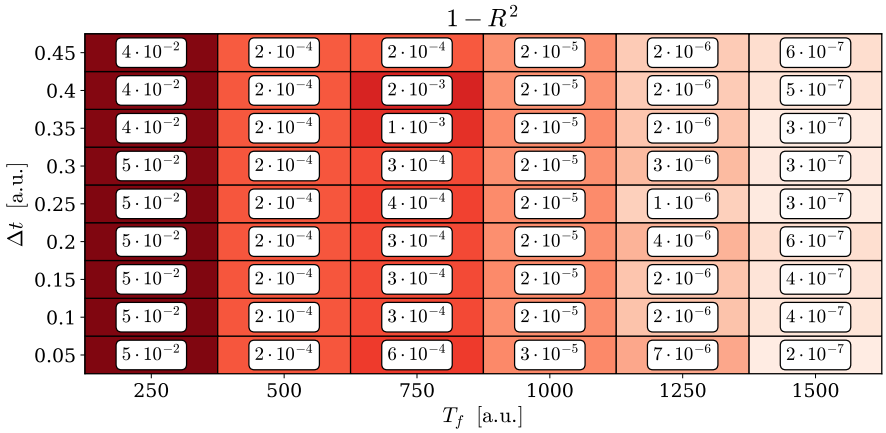

Figure 10.3: Error of the approximated dipole moment $\tilde{\mu}^z(t)$ of LiH. The x-axis shows the time domain $t_n \in [t_0, T_f]$ and y-axis the time step Δt used when determining the frequencies. The function was fitted using $\mu^z(t_n)$, $t_n \in [t_0, 1500 \text{ a.u.}]$ and $\Delta t = 0.01$ a.u. in all cases.

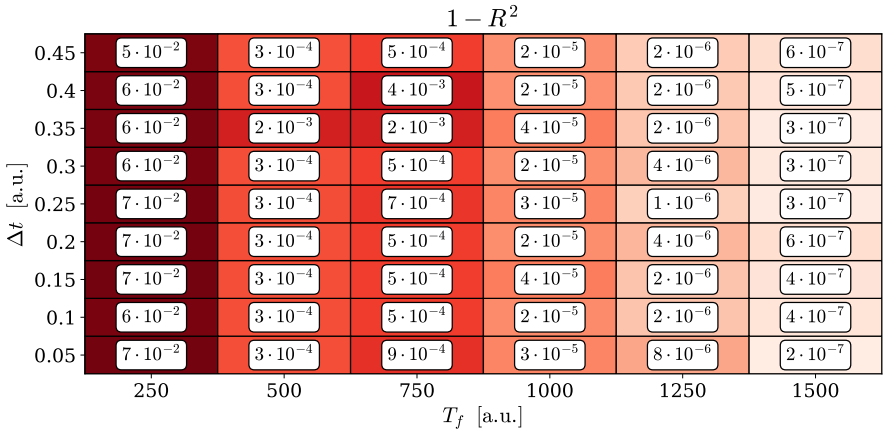

Figure 10.4: Error of the approximated dipole moment $\tilde{\mu}^z(t)$ of LiH. The x-axis shows the time domain $t_n \in [t_0, T_f]$ and y-axis the time step Δt used when determining the frequencies. The function was fitted using $\mu^z(t_n)$, $t_n \in [t_0, T_f]$ and $\Delta t = 0.01$ a.u. in all cases.

The available dipole trajectory must be split into fitting data and verification data, in order to evaluate the success of the function approximation. *Available trajectory* only includes the dipole moment on the time domain $t_n \in [t_0, T_f]$. Since the error seems to be more sensitive to the estimated frequencies than the least squares fitting, the frequencies will be estimated using the entire available trajectory. The study in Fig. 10.4 was repeated twice again using

first 75% and then 50% of the available data for the fitting. The results are shown in Figs. 10.5 and 10.6, respectively. The error in Fig. 10.5 is slightly

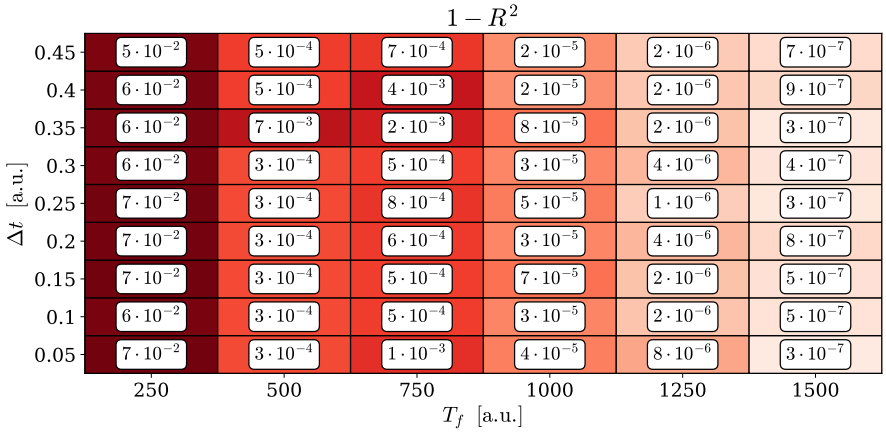

Figure 10.5: Error of the approximated dipole moment $\tilde{\mu}^z(t)$ of LiH. The x-axis shows the time domain $t_n \in [t_0, T_f]$ and y-axis the time step Δt used when determining the frequencies. The function was fitted using $\mu^z(t_n)$, $t_n \in [t_0, 0.75 \cdot T_f]$ and $\Delta t = 0.01$ a.u. in all cases.

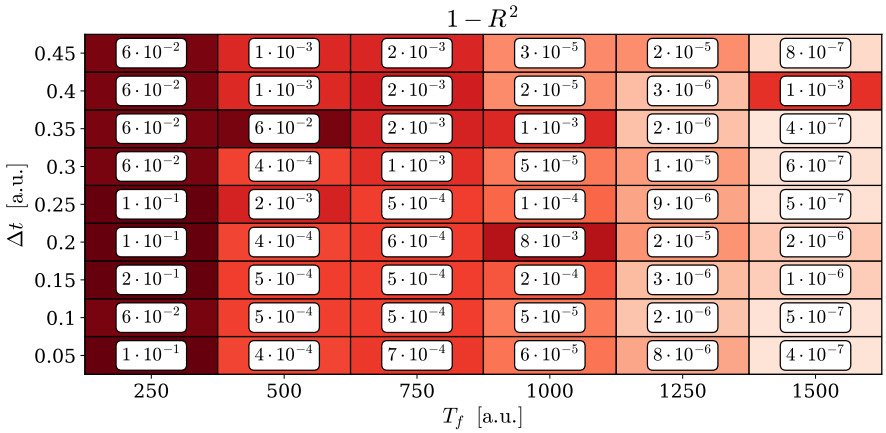

Figure 10.6: Error of the approximated dipole moment $\tilde{\mu}^z(t)$ of LiH. The x-axis shows the time domain $t_n \in [t_0, T_f]$ and y-axis the time step Δt used when determining the frequencies. The function was fitted using $\mu^z(t_n)$, $t_n \in [t_0, 0.5 \cdot T_f]$ and $\Delta t = 0.01$ a.u. in all cases.

higher compared to Fig. 10.4, where the entire available trajectory was used for the fitting. The study using only half of the trajectory for fitting in Fig. 10.6 shows a clear increase in error compared to Fig. 10.4, including some seemingly

random jumps (e.g. at $T_f = 1500$ a.u., $\Delta t = 0.4$ a.u.). In this limited study of the verification window size, it seems that a verification window of 50% is too large, while a verification window of 25% does not have a significant negative impact on the quality of the fitting.

The visual table in Fig. 10.7 shows the number of estimated frequencies found in the studies from in Figs. 10.3 to 10.6. The number of estimated

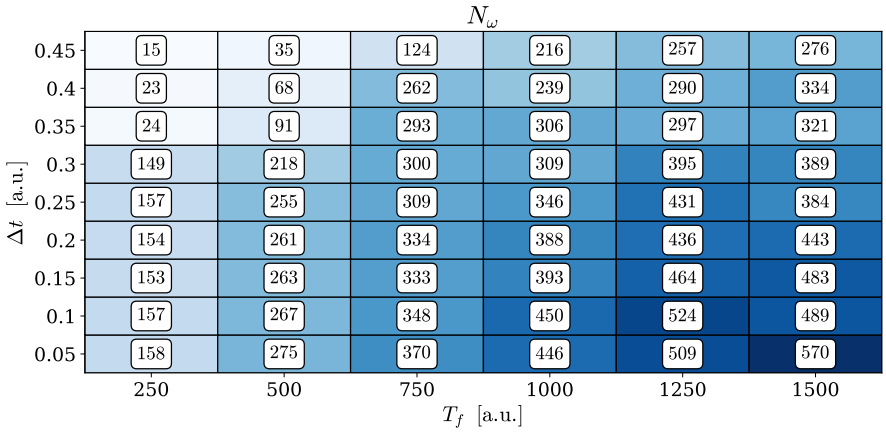

Figure 10.7: Number of frequencies estimated in the dipole moment of LiH. The x-axis shows the time domain $t_n \in [t_0, T_f]$ and y-axis the time step Δt used when determining the frequencies.

frequencies increases with the number of dipole data points provided to the frequency estimator. By looking at the columns in Fig. 10.7, the number of frequencies increases when a smaller time step (and hence more data points) is used, while the error in Fig. 10.3 remains quite stable in the columns. This suggests that the increase in number of frequencies does not correspond to actual frequencies found, but rather that the clustering algorithm is less successful in separating the actual frequencies from the redundant roots of $Q(z(\omega))$. The clustering of the roots to obtain the frequencies in the dipole moment does not yield a clean separation, as shown in Fig. 10.8. The unclear separation between the frequencies and the redundant roots of $Q(z(\omega))$, as seen in Fig. 10.8, is to various degrees representative for the observations made during this project. The behavior of the frequency clusters of the dipole moment deviates from the frequency clusters from synthetic signals. The synthetic signals were observed to give a much clearer division between the estimated frequencies and the redundant roots. The clustering of the potential frequencies of the synthetic signal $f(t)$ from Eq. (5.12) in Fig. 7.1 shows a clear division. A clear division was also observed in cases of poor resolution for the synthetic signals, even when the set of estimated frequencies was imprecise and incomplete.

It is unclear why the behavior is different for synthetic signals and the dipole moment, but two possible explanations can be offered. Firstly, the synthetic signals have no noise, while the dipole moment will suffer from a small but increasing numerical error due to the numerical integration in the time domain.

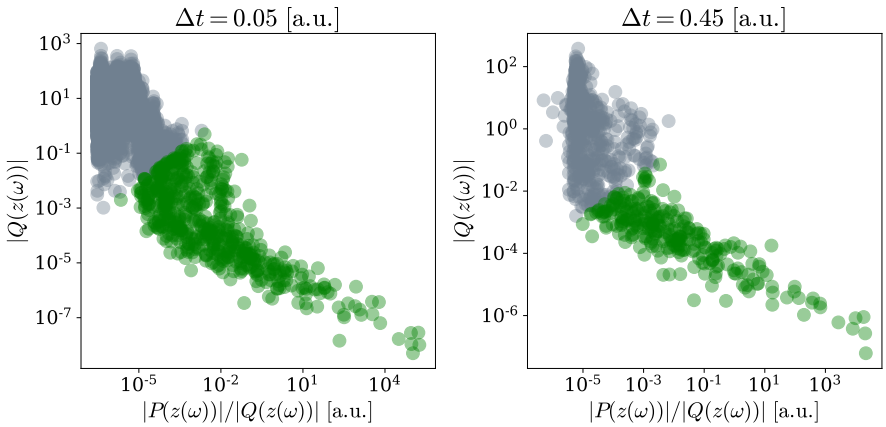

Figure 10.8: Clustering of possible frequencies found in $\mu^z(t)$ of LiH, using the interval $t_n \in [t_0, 1500$ a.u.]. The green circles are estimated frequencies, while the gray circles are deemed as redundancies.

Secondly, the dipole moment contains a large amount of frequencies with very low intensities. These frequencies are not interesting for fitting of the dipole moment, but may cause difficulties in the resolution of the Fourier-Padé.

When creating the function approximation $\tilde{\mu}^d(t)$ to the dipole moment $\mu^d(t)$, more than 50% of the available trajectory should be used for linear fitting. Providing a large amount of data points when estimating frequencies seems to increase the number of redundant roots among the estimated frequencies. The success of the fitting depends greatly on the length of time domain, T_f, and does not seem to be improved when reducing the step length, Δt. When fitting the dipole moment in the subsequent chapters, the available trajectory will be divided into 75% fitting data and a 25% verification window. The number of data points used for Fourier-Padé in the frequency estimator will be held constant, such that Δt will depend on the trajectory length, T_f.

CHAPTER 11

Performance of the Fitting Model

This chapter shows the fitting of the full z-component of the dipole moment $\mu^z(t)$ from RT-TDCCSD simulations. All simulation details can be found in Section 10.1. Each study features a different atom or molecule, but the study follows the same structure for all cases.

The dipole moment for each system was approximated using the dipole trajectory $\mu^z(t_n)$ with $t_n \in [t_0, T_{\text{ver}}]$, repeated several times using different trajectory lengths. The frequencies were estimated using the full length of the trajectory, $t_n \in [t_0, T_{\text{ver}}]$, but the time step was increased such that the number of dipole data points provided to the frequency estimator should not exceed $7.5 \cdot 10^3$ time points. The linear coefficients were determined using the dipole data $\mu^z(t_n)$ with $t_n \in [t_0, T_{\text{fit}}]$, using 75% of the trajectory

$$T_{\text{fit}} = 0.75 \cdot T_{\text{ver}}, \tag{11.1}$$

leaving a verification window of 25%. The fitting and error measure use all data points, i.e. using $\Delta t = 0.01$. The error of the approximated dipole $\tilde{\mu}^z(t)$ is presented in tables, and is calculated using the coefficient of determination in Eq. (8.19). The error is calculated separately on the fitting data, the verification window and on the full test data:

$$\begin{aligned} E_{\text{fit}} \quad & t_n \in [t_0, T_{\text{fit}}] \\ E_{\text{ver}} \quad & t_n \in (T_{\text{fit}}, T_{\text{ver}}] \\ E_{\text{full}} \quad & t_n \in [t_0, T_{\text{full}}], \end{aligned} \tag{11.2}$$

using $\Delta t = 0.01$ a.u. and $t_0 = 0.02$ a.u.. The error E_{fit} shows the error in the fitting domain, E_{ver} is the error in the verification domain, and E_{full} is the benchmarking error showing the error in a long extrapolation. The dipole moment of each atom and molecule has been calculated for a very long trajectory, $t_n \in [0, T_{\text{full}}]$ to evaluate if the extrapolation is truly stable and correct.

For each system, two cases of dipole extrapolation have been chosen for a closer look. These examples are chosen to illustrate the significance of the size of the error. The spectra shown in this chapter are calculated according to

$$I_z(\omega_i) = \frac{S_z(\omega_i)}{\max_{\omega_j} S_z(\omega_j)}, \tag{11.3}$$

where only the z-component of the absorption spectrum:

$$S_z(\omega) = \frac{8\pi^2\omega}{3c\mathrm{F}_{\text{str}}} \operatorname{Im}[\mu^z(\omega)] \tag{11.4}$$

is included. Note that while $S(\omega) = S_x(\omega) + S_y(\omega) + S_z(\omega)$, the same is not necessarily true for $I(\omega)$. For symmetry reasons, the relative spectrum can only be given as $I(\omega) = I_x(\omega) + I_y(\omega) + I_z(\omega)$ for atoms. Each absorption spectrum figure in this chapter will show the spectrum of the approximated dipole moment $\tilde{\mu}^z(t)$ extrapolated from T_{ver} to T_{full}, together with the spectrum obtained from the short trajectory used for the function approximation $t_n \in [t_0, T_{\text{ver}}]$ and the spectrum using all available data $t_n \in [t_0, T_{\text{full}}]$. All computed spectra in this chapter will use the lifetime parameter

$$\gamma = \frac{\pi}{N_t \Delta t}, \tag{11.5}$$

where $\Delta t = 0.01$ will be used in all cases and N_t is the number of data points used for the discrete Fourier transform.

11.1 Fitting Using Ordinary Least Squares

This first section will present the studies of the fitting model using the ordinary least squares method for optimizing the linear coefficients. The studies of each atom or molecule follow the structure described in the beginning of this chapter. Some cases of extrapolation T_{ver} for each system are chosen for a closer look. These are chosen to illustrate the correlation between the quantitative measure of error in the time domain and the more qualitative evaluation of the approximated absorption spectra.

11.1.1 The Helium Atom

The full z-component of the dipole moment $\mu^z(t)$ of helium using the aug-cc-pVTZ basis set was sampled up to $T_{\text{full}} = 6000$ a.u.. The error from the extrapolation using different trajectory lengths is presented in Table 11.1.

Table 11.1: Coefficient of determination when fitting $\mu^z(t)$ of He using OLS.

$\boldsymbol{T}_{\text{ver}}$ [a.u.]	$\boldsymbol{E}_{\text{fit}}$	$\boldsymbol{E}_{\text{ver}}$	$\boldsymbol{E}_{\text{full}}$	$\boldsymbol{E}_{\text{ver}}/\boldsymbol{E}_{\text{fit}}$
10	$1 \cdot 10^{-10}$	$2 \cdot 10^{-5}$	$1 \cdot 10^{-1}$	$1 \cdot 10^{5}$
20	$1 \cdot 10^{-10}$	$1 \cdot 10^{-10}$	$2 \cdot 10^{-8}$	1
50	$4 \cdot 10^{-12}$	$4 \cdot 10^{-12}$	$1 \cdot 10^{-8}$	1
75	$8 \cdot 10^{-15}$	$4 \cdot 10^{-12}$	$1 \cdot 10^{-8}$	$5 \cdot 10^{2}$
100	$7 \cdot 10^{-15}$	$2 \cdot 10^{-13}$	$1 \cdot 10^{-8}$	$3 \cdot 10$
150	$2 \cdot 10^{-13}$	$1 \cdot 10^{-11}$	$1 \cdot 10^{-8}$	$4 \cdot 10$
200	$1 \cdot 10^{-12}$	$3 \cdot 10^{-11}$	$1 \cdot 10^{-8}$	$2 \cdot 10$
300	$1 \cdot 10^{-12}$	$5 \cdot 10^{-11}$	$1 \cdot 10^{-8}$	$4 \cdot 10$
400	$2 \cdot 10^{-12}$	$1 \cdot 10^{-10}$	$2 \cdot 10^{-8}$	$9 \cdot 10$
500	$3 \cdot 10^{-13}$	$3 \cdot 10^{-11}$	$1 \cdot 10^{-8}$	$7 \cdot 10$
600	$5 \cdot 10^{-12}$	$2 \cdot 10^{-10}$	$1 \cdot 10^{-8}$	$5 \cdot 10$
750	$2 \cdot 10^{-11}$	$3 \cdot 10^{-10}$	$1 \cdot 10^{-8}$	$2 \cdot 10$
1000	$3 \cdot 10^{-13}$	$1 \cdot 10^{-11}$	$6 \cdot 10^{-9}$	$4 \cdot 10$
1250	$2 \cdot 10^{-12}$	$1 \cdot 10^{-10}$	$1 \cdot 10^{-8}$	$5 \cdot 10$
1500	$3 \cdot 10^{-12}$	$1 \cdot 10^{-9}$	$1 \cdot 10^{-8}$	$5 \cdot 10^{2}$
1750	$2 \cdot 10^{-10}$	$2 \cdot 10^{-9}$	$2 \cdot 10^{-8}$	$2 \cdot 10$

The error of the extrapolation is approximately 10^{-8} for the long extrapolation to T_{full}, for all but the very smallest fitting trajectory. This corresponds to a very good fit, as is shown in Fig. 11.1, where the spectrum of the extrapolation from $T_{\text{ver}} = 20$ a.u. is evaluated. The spectrum of the

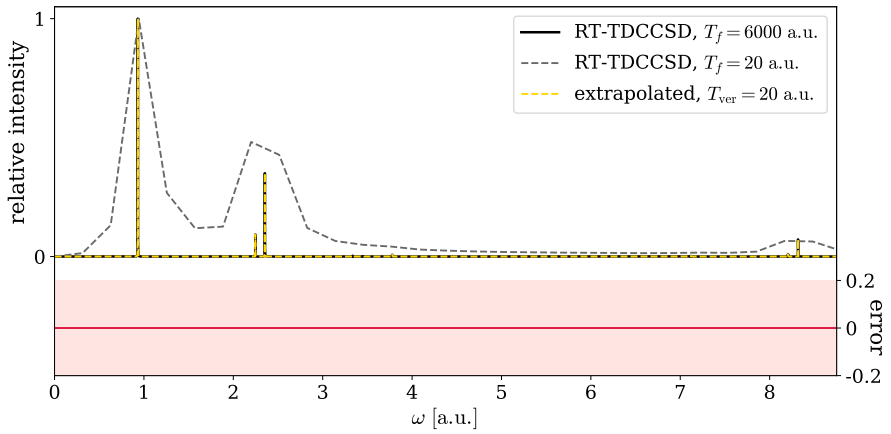

Figure 11.1: Evaluation of the extrapolation of $\mu^z(t)$ of He from 20 a.u. to 6000 a.u. using OLS. The spectrum of the extrapolation $\tilde{I}_z(\omega)$ is shown in yellow, the spectrum of the short trajectory is gray and long trajectory spectrum $I_z(\omega)$ is shown in black. The red area shows the error $\tilde{I}_z(\omega) - I_z(\omega)$.

extrapolated dipole $\tilde{\mu}^z(t)$ is indistinguishable from the actual high resolution spectrum from the real-time simulations. The extrapolation is a significant improvement over the short trajectory, which shows a very poor resolution spectrum. The dipole trajectory in Fig. 11.2 was used for the extrapolation

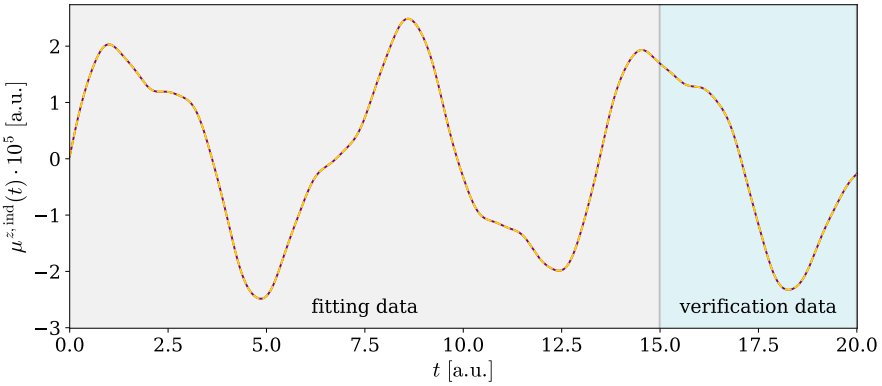

Figure 11.2: Comparison of the RT-TDCCSD dipole moment $\mu^z(t)$ of He (purple solid line) and its approximation $\tilde{\mu}^z(t)$ (yellow dashed line).

shown in Fig. 11.1. The dipole $\mu^z(t)$ and its approximation $\tilde{\mu}^z(t)$ show no

visible difference.

Only the first case with $T_{\text{ver}} = 10$ a.u. has a noteworthy higher error in the full extrapolation, ($E_{\text{full}} = 10^{-1}$). There is a significant error in the frequency estimation in this case, as can be seen in Fig. 11.3. The most prominent

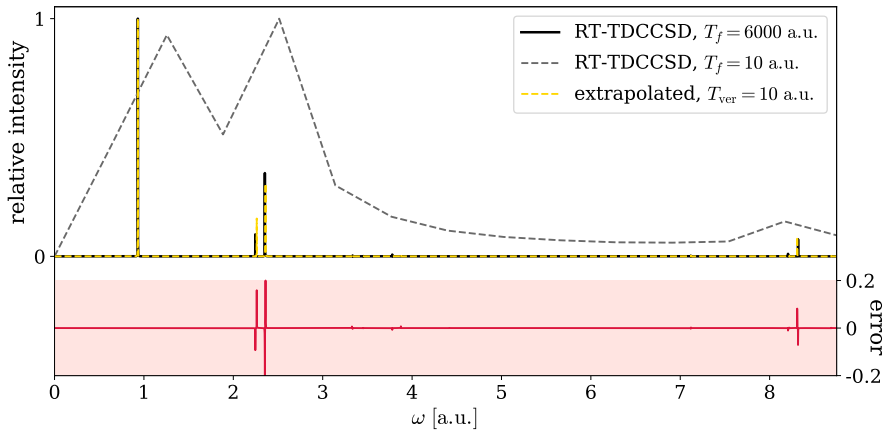

Figure 11.3: Evaluation of the extrapolation of $\mu^z(t)$ of He from 10 a.u. to 6000 a.u. using OLS. The spectrum of the extrapolation $\tilde{I}_z(\omega)$ is shown in yellow, the spectrum of the short trajectory is gray and long trajectory spectrum $I_z(\omega)$ is shown in black. The red area shows the error $\tilde{I}_z(\omega) - I_z(\omega)$.

peak (at $\omega \approx 1$ a.u.) is estimated well, though the two smaller peaks (between $2 - 2.5$ a.u.) are slightly shifted to the right. The approximated function $\tilde{\mu}^z(t)$ is shown in Fig. 11.4. The error on the fitting data is small ($E_{\text{fit}} = 10^{-10}$),

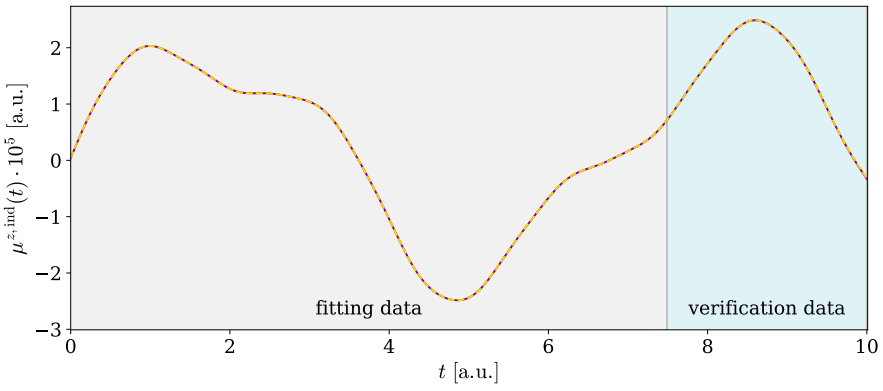

Figure 11.4: Comparison of the RT-TDCCSD dipole moment $\mu^z(t)$ of He (purple solid line) and its approximation $\tilde{\mu}^z(t)$ (yellow dashed line).

and comparable in size to successful extrapolations in Table 11.1. The error in the verification data ($E_{\text{ver}} = 10^{-5}$) is much larger compared to the successful

extrapolations ($E_{\text{ver}} \in [10^{-12}, 10^{-9}]$), but still not visible, as seen in Fig. 11.4. The jump in error from the fitting data to the verification data is very large ($E_{\text{ver}}/E_{\text{fit}} = 10^5$), and can be seen as a warning of over-fitting.

11.1.2 The Hydrogen Molecule

In the simulations of the hydrogen molecule using the aug-cc-pVTZ basis set, the z-component of dipole moment $\mu^z(t)$ was sampled up to $T_{\text{full}} = 8000$ a.u.. The error in the extrapolation using different trajectory lengths is given in Table 11.2. The error in the extrapolation to T_{full} is larger for the

Table 11.2: Coefficient of determination when fitting $\mu^z(t)$ of H_2 using OLS.

$\boldsymbol{T}_{\text{ver}}$ [a.u.]	$\boldsymbol{E}_{\text{fit}}$	$\boldsymbol{E}_{\text{ver}}$	$\boldsymbol{E}_{\text{full}}$	$\boldsymbol{E}_{\text{ver}}/\boldsymbol{E}_{\text{fit}}$
10	$1 \cdot 10^{-4}$	$1 \cdot 10$	3	$9 \cdot 10^4$
20	$2 \cdot 10^{-5}$	$8 \cdot 10^{-1}$	2	$5 \cdot 10^4$
50	$2 \cdot 10^{-8}$	$6 \cdot 10^{-6}$	$1 \cdot 10^{-3}$	$3 \cdot 10^2$
75	$7 \cdot 10^{-9}$	$4 \cdot 10^{-7}$	$1 \cdot 10^{-4}$	$5 \cdot 10$
100	$1 \cdot 10^{-9}$	$1 \cdot 10^{-7}$	$9 \cdot 10^{-6}$	$1 \cdot 10^2$
150	$3 \cdot 10^{-10}$	$2 \cdot 10^{-8}$	$6 \cdot 10^{-6}$	$5 \cdot 10$
200	$6 \cdot 10^{-11}$	$1 \cdot 10^{-8}$	$5 \cdot 10^{-6}$	$2 \cdot 10^2$
300	$3 \cdot 10^{-11}$	$2 \cdot 10^{-10}$	$2 \cdot 10^{-7}$	8
400	$2 \cdot 10^{-11}$	$2 \cdot 10^{-10}$	$1 \cdot 10^{-7}$	$1 \cdot 10$
500	$3 \cdot 10^{-11}$	$3 \cdot 10^{-10}$	$3 \cdot 10^{-8}$	8
600	$1 \cdot 10^{-10}$	$2 \cdot 10^{-10}$	$1 \cdot 10^{-8}$	2
750	$1 \cdot 10^{-10}$	$2 \cdot 10^{-10}$	$1 \cdot 10^{-8}$	1
1000	$5 \cdot 10^{-8}$	$5 \cdot 10^{-8}$	$6 \cdot 10^{-8}$	1
1250	$2 \cdot 10^{-10}$	$7 \cdot 10^{-10}$	$1 \cdot 10^{-8}$	3
1500	$3 \cdot 10^{-10}$	$1 \cdot 10^{-9}$	$1 \cdot 10^{-8}$	4
1750	$3 \cdot 10^{-10}$	$2 \cdot 10^{-9}$	$1 \cdot 10^{-8}$	6

hydrogen molecule compared to the helium atom. While the extrapolation error of helium was $E_{\text{full}} = 10^{-8}$ for all $T_{\text{ver}} \geq 20$ a.u., the same precision is achieved for $T_{\text{ver}} \geq 500$ a.u. for hydrogen. The error in the extrapolation is expected to increase in time. Since the full trajectory length of the hydrogen molecule ($T_{\text{full}} = 8000$ a.u.) is longer compared to that of the helium atom ($T_{\text{full}} = 6000$ a.u.), a direct comparison in the extrapolation error E_{full} will be somewhat unbalanced. The extrapolation error of the hydrogen molecule might appear to be higher simply because the extrapolation is longer compared to that of the helium atom. The goal of the error measure is to find a convergence criterion based on E_{fit} and E_{ver}, as the extrapolation error E_{full} will not be known. The full trajectory length T_{full} should correspond to a high resolution spectrum in the development phase of the dipole fitting model. The two atoms helium and beryllium therefore have somewhat shorter trajectories.

As seen in Fig. 11.5, the extrapolation error of $E_{\text{full}} = 9 \cdot 10^{-6}$ (for $T_{\text{ver}} = 100$ a.u.) is sufficient for a perfect approximation of the absorption spectrum. This also gives a great improvement over the poor resolution spectrum obtained by the trajectory used in the dipole extrapolation. The dipole data $\mu^z(t)$ used for the extrapolation in Fig. 11.5, along with its approximation $\tilde{\mu}^z(t)$, is shown in Fig. 11.6. There is no visible difference between the two.

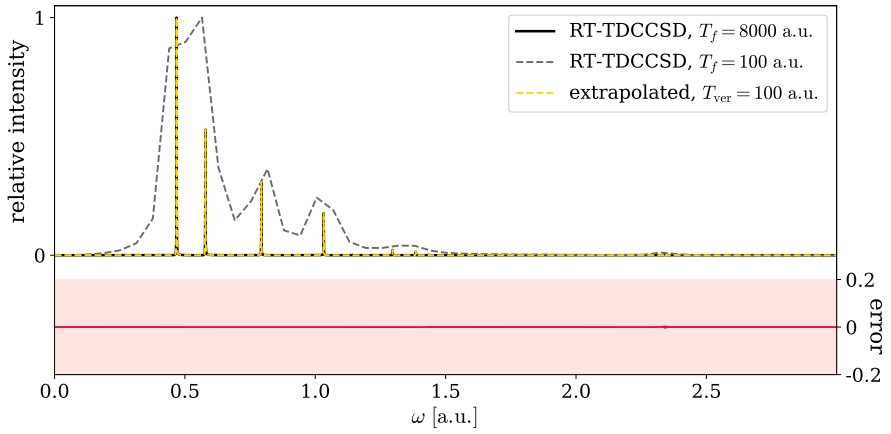

Figure 11.5: Evaluation of the extrapolation of $\mu^z(t)$ of H_2 from 100 a.u. to 8000 a.u. using OLS. The spectrum of the extrapolation $\tilde{I}_z(\omega)$ is shown in yellow, the spectrum of the short trajectory is gray and long trajectory spectrum $I_z(\omega)$ is shown in black. The red area shows the error $\tilde{I}_z(\omega) - I_z(\omega)$.

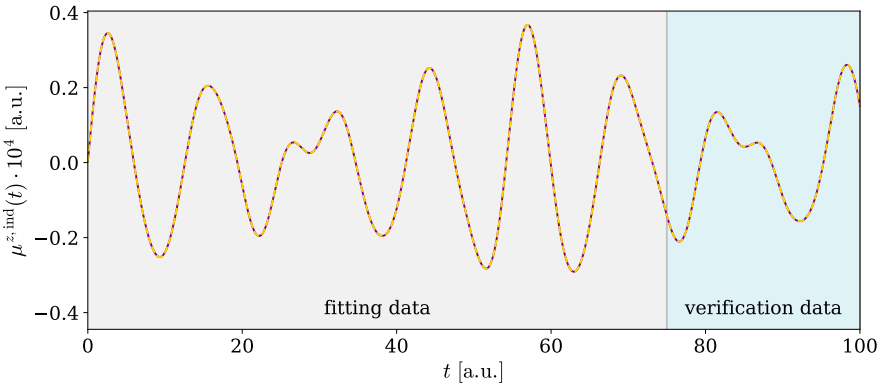

Figure 11.6: Comparison of the RT-TDCCSD dipole moment $\mu^z(t)$ of H_2 (purple solid line) and its approximation $\tilde{\mu}^z(t)$ (yellow dashed line).

The verification error ($E_{\text{ver}} = 1 \cdot 10^{-7}$) of the successful extrapolation using $T_{\text{ver}} = 100$ a.u. is significantly lower than the verification error ($E_{\text{ver}} = 6 \cdot 10^{-6}$) of the extrapolation using $T_{\text{ver}} = 50$ a.u.. The difference in the extrapolation error is a little more than a hundred times larger for $T_{\text{ver}} = 50$ a.u. ($E_{\text{full}} = 1 \cdot 10^{-3}$) compared to that of $T_{\text{ver}} = 100$ a.u. ($E_{\text{full}} = 9 \cdot 10^{-6}$). Still, the spectra in Fig. 11.7 show only a very small difference between the true high resolution spectrum and the spectrum obtained by the extrapolation. The difference between the two spectra is not easily spotted, but is visible on the error line $\tilde{I}_z(\omega) - I_z(\omega)$ in the red area below the spectra. The error of the fitted function

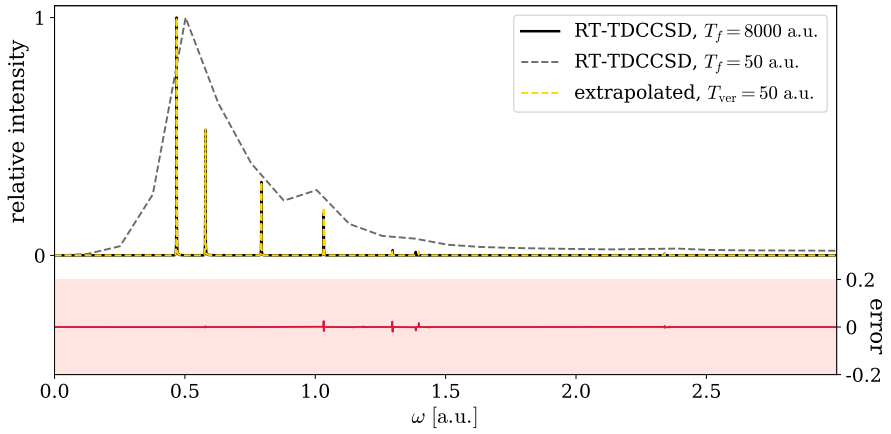

Figure 11.7: Evaluation of the extrapolation of $\mu^z(t)$ of H_2 from 50 a.u. to 8000 a.u. using OLS. The spectrum of the extrapolation $\tilde{I}_z(\omega)$ is shown in yellow, the spectrum of the short trajectory is gray and long trajectory spectrum $I_z(\omega)$ is shown in black. The red area shows the error $\tilde{I}_z(\omega) - I_z(\omega)$.

$\tilde{\mu}^z(t)$ in the verification window is too small to observe in Fig. 11.8.

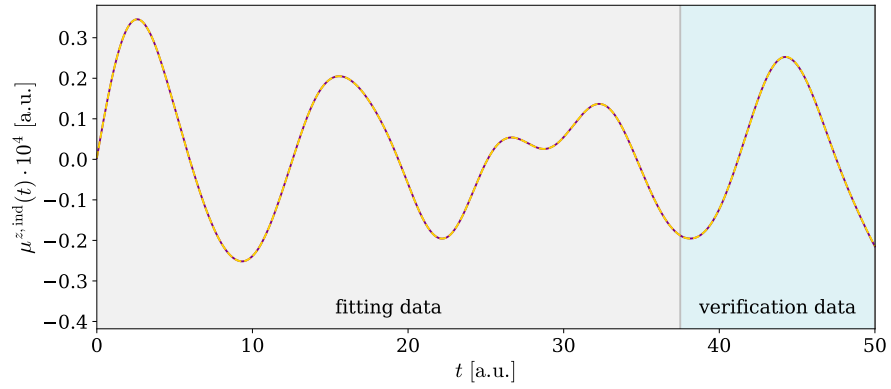

Figure 11.8: Comparison of the RT-TDCCSD dipole moment $\mu^z(t)$ of H_2 (purple solid line) and its approximation $\tilde{\mu}^z(t)$ (yellow dashed line).

The only two examples from Table 11.2 giving poor approximation to the absorption spectrum were $T_{\text{ver}} = 10$ a.u. and $T_{\text{ver}} = 20$ a.u.. The spectrum of the extrapolation using $T_{\text{ver}} = 20$ a.u. is shown in Fig. 11.9. In this case, the verification error ($E_{\text{ver}} = 8 \cdot 10^{-1}$) and the extrapolation error ($E_{\text{full}} = 2$) was much higher than the previous two cases. The ratio between the verification error and the fitting error ($E_{\text{ver}}/E_{\text{fit}} = 5 \cdot 10^4$) was also very high. The extrapolation spectrum is missing significant peaks, and the existing peaks are not on the correct location on the ω-axis. The error of the fitted function $\tilde{\mu}^z(t)$ is clearly

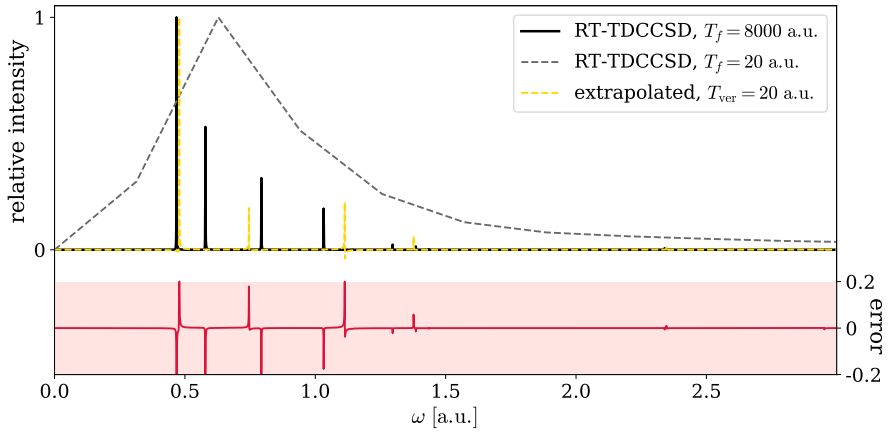

Figure 11.9: Evaluation of the extrapolation of $\mu^z(t)$ of H_2 from 20 a.u. to 8000 a.u. using OLS. The spectrum of the extrapolation $\tilde{I}_z(\omega)$ is shown in yellow, the spectrum of the short trajectory is gray and long trajectory spectrum $I_z(\omega)$ is shown in black. The red area shows the error $\tilde{I}_z(\omega) - I_z(\omega)$.

visible in Fig. 11.10.

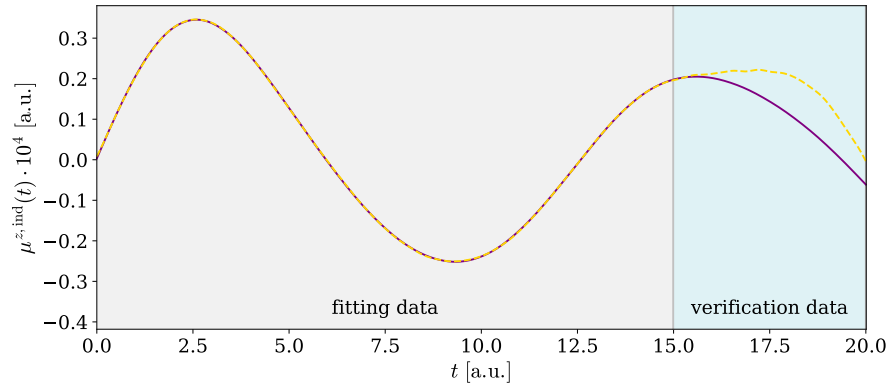

Figure 11.10: Comparison of the RT-TDCCSD dipole moment $\mu^z(t)$ of H_2 (purple solid line) and its approximation $\tilde{\mu}^z(t)$ (yellow dashed line).

11.1.3 The Beryllium Atom

The dipole moment $\mu^z(t)$ was sampled up to $T_{\text{full}} = 6000$ a.u. during the RT-TDCCSD calculations of the beryllium atom. The calculations used the aug-cc-pVTZ basis set. The error from the extrapolation using different trajectory lengths is given in Table 11.3.

Table 11.3: Coefficient of determination when fitting $\mu^z(t)$ of Be using OLS.

T_{ver} [a.u.]	E_{fit}	E_{ver}	E_{full}	$E_{\text{ver}}/E_{\text{fit}}$
10	$2 \cdot 10^{-8}$	$2 \cdot 10^{-1}$	3	$1 \cdot 10^{7}$
20	$4 \cdot 10^{-5}$	$7 \cdot 10^{-2}$	1	$2 \cdot 10^{3}$
50	$3 \cdot 10^{-6}$	$3 \cdot 10^{-4}$	$2 \cdot 10^{-1}$	$1 \cdot 10^{2}$
75	$2 \cdot 10^{-7}$	$2 \cdot 10^{-5}$	$4 \cdot 10^{-3}$	$1 \cdot 10^{2}$
100	$6 \cdot 10^{-7}$	$1 \cdot 10^{-5}$	$2 \cdot 10^{-3}$	$2 \cdot 10$
150	$6 \cdot 10^{-10}$	$5 \cdot 10^{-8}$	$2 \cdot 10^{-5}$	$9 \cdot 10$
200	$6 \cdot 10^{-11}$	$6 \cdot 10^{-9}$	$6 \cdot 10^{-7}$	$9 \cdot 10$
300	$1 \cdot 10^{-11}$	$6 \cdot 10^{-9}$	$3 \cdot 10^{-7}$	$5 \cdot 10^{2}$
400	$4 \cdot 10^{-11}$	$4 \cdot 10^{-11}$	$8 \cdot 10^{-10}$	1
500	$3 \cdot 10^{-11}$	$3 \cdot 10^{-11}$	$5 \cdot 10^{-10}$	1
600	$2 \cdot 10^{-12}$	$4 \cdot 10^{-12}$	$4 \cdot 10^{-10}$	3
750	$1 \cdot 10^{-10}$	$1 \cdot 10^{-10}$	$5 \cdot 10^{-10}$	1
1000	$2 \cdot 10^{-10}$	$3 \cdot 10^{-10}$	$6 \cdot 10^{-10}$	1
1250	$2 \cdot 10^{-9}$	$2 \cdot 10^{-9}$	$3 \cdot 10^{-9}$	1
1500	$2 \cdot 10^{-8}$	$2 \cdot 10^{-8}$	$2 \cdot 10^{-8}$	1
1750	$2 \cdot 10^{-8}$	$2 \cdot 10^{-8}$	$2 \cdot 10^{-8}$	1

The shortest trajectory yielding a completely successful extrapolation used $T_{\text{ver}} = 150$ a.u., as shown in Fig. 11.11. The spectrum of the extrapolation is

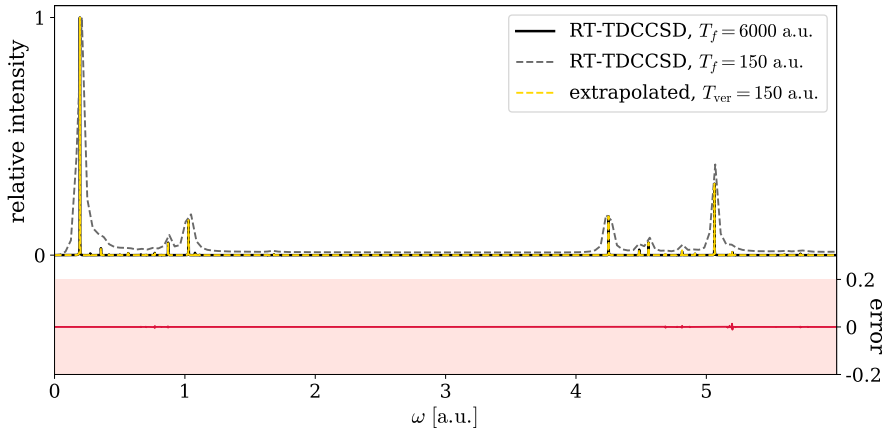

Figure 11.11: Evaluation of the extrapolation of $\mu^z(t)$ of Be from 150 a.u. to 6000 a.u. using OLS. The spectrum of the extrapolation $\tilde{I}_z(\omega)$ is shown in yellow, the spectrum of the short trajectory is gray and long trajectory spectrum $I_z(\omega)$ is shown in black. The red area shows the error $\tilde{I}_z(\omega) - I_z(\omega)$.

nearly indistinguishable from the actual high resolution spectrum, and a great improvement over the spectrum obtained using the extrapolation data $\mu^z(t_n)$, $t_n \in [t_0, T_{\text{ver}}]$. The extrapolation spectra using $T_{\text{ver}} = 75$ a.u. and $T_{\text{ver}} = 100$ a.u. were also very good approximations. The extrapolation error ($E_{\text{full}} = 2 \cdot 10^{-5}$) lies in between the three cases shown for the hydrogen molecule, while the

verification error ($E_{\text{ver}} = 2 \cdot 10^{-8}$) is lower for beryllium than for all three cases for hydrogen ($E_{\text{ver}} \sim 10^{-5}$). The dipole data used for the extrapolation in Fig. 11.11 is shown in Fig. 11.12, along with its approximation.

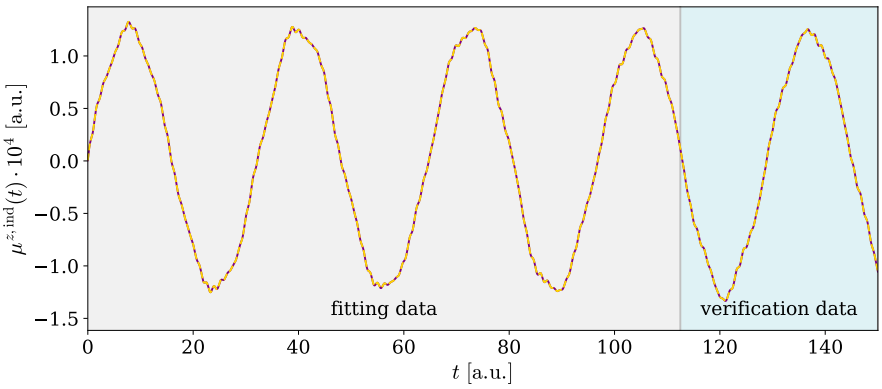

Figure 11.12: Comparison of the RT-TDCCSD dipole moment $\mu^z(t)$ of Be (purple solid line) and its approximation $\tilde{\mu}^z(t)$ (yellow dashed line).

The extrapolation error ($E_{\text{full}} = 2 \cdot 10^{-1}$) of $T_{\text{ver}} = 50$ a.u. is comparable in size to the extrapolation error ($E_{\text{full}} = 1 \cdot 10^{-1}$) of the dipole moment of helium shown in Fig. 11.3. Like in the case of helium, the spectrum of the extrapolated dipole moment of beryllium shows visible deviation from the actual high resolution spectrum. This is shown in Fig. 11.13. Most of the peaks are

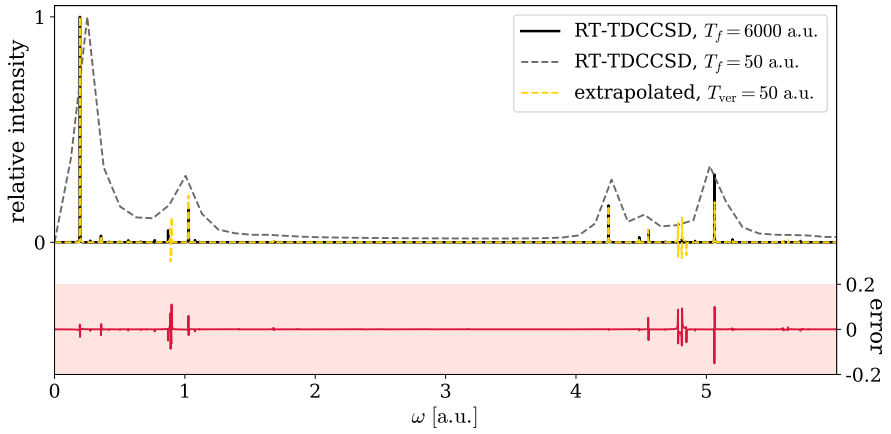

Figure 11.13: Evaluation of the extrapolation of $\mu^z(t)$ of Be from 50 a.u. to 6000 a.u. using OLS. The spectrum of the extrapolation $\tilde{I}_z(\omega)$ is shown in yellow, the spectrum of the short trajectory is gray and long trajectory spectrum $I_z(\omega)$ is shown in black. The red area shows the error $\tilde{I}_z(\omega) - I_z(\omega)$.

approximated quite well, but there are several visible errors. This includes a

cluster of unwanted oscillating peaks around $\omega \approx 4.8$ a.u.. The verification error $E_{\text{ver}} = 3 \cdot 10^{-4}$ corresponds to a visible error in the time domain, as can be seen in Fig. 11.14. The approximated dipole moment $\tilde{\mu}^z(t)$ is slightly larger than

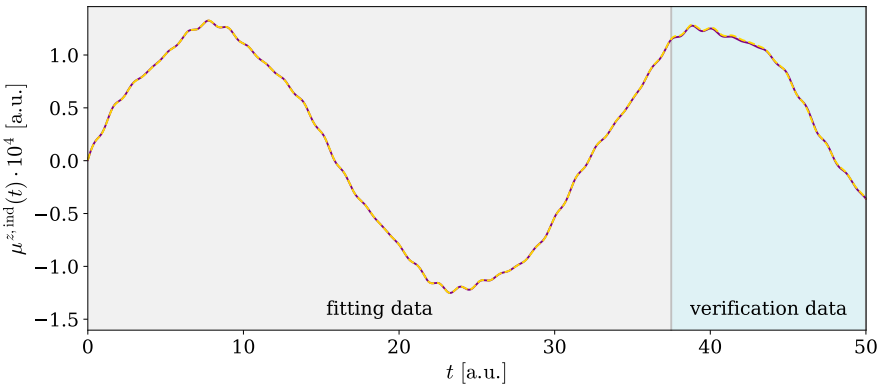

Figure 11.14: Comparison of the RT-TDCCSD dipole moment $\mu^z(t)$ of Be (purple solid line) and its approximation $\tilde{\mu}^z(t)$ (yellow dashed line).

the actual dipole moment $\mu^z(t)$ around $t = 40$ a.u.. There is a visible dominant frequency with a period of ~ 30 a.u.. The fitting data barely contains a full period of the dominant frequency. The extrapolation spectra using $T_{\text{ver}} < 50$ a.u. gave poor approximations to the true high resolution spectrum.

The oscillations around $\omega \approx 4.8$ a.u. in Fig. 11.13 seem to be several unwanted frequencies trying to make up for a missing frequency. This hypothesis is strengthened by Fig. 11.15. Assuming that the *good* approximation of the

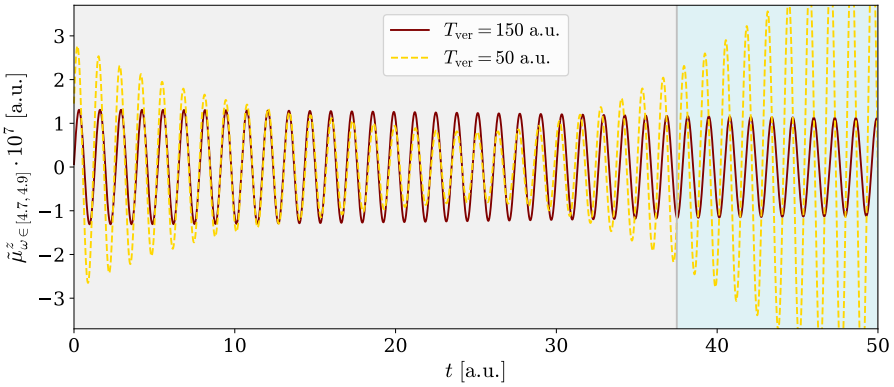

Figure 11.15: A part of approximated dipole moment $\tilde{\mu}^z(t)$ of Be, only including the basis functions with frequencies $\omega \in [4.7, 4.9]$ a.u..

dipole moment using $T_{\text{ver}} = 150$ a.u. has the correct frequencies with correct amplitudes, then one may compare this to the *poor* approximation of the dipole

moment using $T_{\text{ver}} = 50$ a.u.. Only the frequency domain $\omega \in [4.7, 4.9]$ a.u. is included in Fig. 11.15. While the *good* $\tilde{\mu}$ seems to be dominated by a single frequency, the *bad* $\tilde{\mu}$ clearly consists of several frequencies. The unwanted several frequencies are severely over-fitted on the short trajectory, causing the oscillations in the spectrum.

11.1.4 Lithium Hydride

The error of $\tilde{\mu}^z(t)$ of lithium hydride using the aug-cc-pVDZ basis set is given in Table 11.4. The full dipole moment $\mu^z(t)$ was sampled up to $T_{\text{full}} = 8000$ a.u..

Table 11.4: Coefficient of determination when fitting $\mu^z(t)$ of LiH using OLS.

$\boldsymbol{T}_{\text{ver}}$ [a.u.]	$\boldsymbol{E}_{\text{fit}}$	$\boldsymbol{E}_{\text{ver}}$	$\boldsymbol{E}_{\text{full}}$	$\boldsymbol{E}_{\text{ver}}/\boldsymbol{E}_{\text{fit}}$
10	$6 \cdot 10^{-3}$	$1 \cdot 10$	3	$2 \cdot 10^{3}$
20	$1 \cdot 10^{-3}$	5	3	$5 \cdot 10^{3}$
50	$4 \cdot 10^{-1}$	$2 \cdot 10$	4	$6 \cdot 10$
75	$9 \cdot 10^{-3}$	1	2	$1 \cdot 10^{2}$
100	$3 \cdot 10^{-3}$	$6 \cdot 10^{-1}$	3	$2 \cdot 10^{2}$
150	$3 \cdot 10^{-3}$	$2 \cdot 10^{-1}$	1	$6 \cdot 10$
200	$3 \cdot 10^{-5}$	$9 \cdot 10^{-4}$	$3 \cdot 10^{-1}$	$3 \cdot 10$
300	$1 \cdot 10^{-5}$	$1 \cdot 10^{-4}$	$6 \cdot 10^{-3}$	$1 \cdot 10$
400	$5 \cdot 10^{-6}$	$3 \cdot 10^{-5}$	$7 \cdot 10^{-4}$	6
500	$3 \cdot 10^{-6}$	$5 \cdot 10^{-5}$	$3 \cdot 10^{-4}$	$2 \cdot 10$
600	$2 \cdot 10^{-6}$	$2 \cdot 10^{-5}$	$4 \cdot 10^{-4}$	$1 \cdot 10$
750	$4 \cdot 10^{-7}$	$2 \cdot 10^{-5}$	$5 \cdot 10^{-4}$	$4 \cdot 10$
1000	$6 \cdot 10^{-8}$	$3 \cdot 10^{-6}$	$5 \cdot 10^{-5}$	$5 \cdot 10$
1250	$7 \cdot 10^{-9}$	$2 \cdot 10^{-7}$	$3 \cdot 10^{-6}$	$3 \cdot 10$
1500	$1 \cdot 10^{-9}$	$8 \cdot 10^{-8}$	$8 \cdot 10^{-7}$	$6 \cdot 10$
1750	$2 \cdot 10^{-9}$	$8 \cdot 10^{-8}$	$1 \cdot 10^{-7}$	$5 \cdot 10$

The extrapolations using $T_{\text{ver}} \geq 1250$ a.u. yields spectra indistinguishable from the true high resolution spectrum of lithium hydride. Both the verification error ($E_{\text{ver}} \sim 10^{-8}$) and the extrapolation error ($E_{\text{full}} \in (10^{-6}, 10^{-8})$) for these cases strongly suggest that the extrapolation was successful. The spectrum for the $T_{\text{ver}} = 1250$ a.u. extrapolation is shown in Fig. 11.16, where the trajectory used for the extrapolation has decent spectral resolution. The dipole data used for the extrapolation in Fig. 11.16, along with the approximation $\tilde{\mu}^z(t)$, is shown in Fig. 11.17.

The extrapolations on data $T_{\text{ver}} \in [400, 750]$ a.u. display similar behavior in Table 11.4. The verification error is $E_{\text{ver}} \sim 10^{-5}$ and the extrapolation error $E_{\text{full}} \sim 10^{-4}$. This is comparable to the hydrogen molecule using $T_{\text{ver}} = 50$ a.u., with $E_{\text{ver}} = 6 \cdot 10^{-6}$ and $E_{\text{full}} = 1 \cdot 10^{-3}$. The verification error was slightly lower for the hydrogen molecule, but the ratio $E_{\text{ver}}/E_{\text{fit}} = 3 \cdot 10^{2}$ was higher for the hydrogen molecule than for the fitting of lithium hydride $E_{\text{ver}}/E_{\text{fit}} \sim 10$. The spectra obtained by the extrapolations on $T_{\text{ver}} \in [400, 750]$ a.u. of lithium hydride are also comparable to the spectrum of hydrogen extrapolated from $T_{\text{ver}} = 50$ a.u., seen in Fig. 11.7. The worst of these spectra of lithium hydride

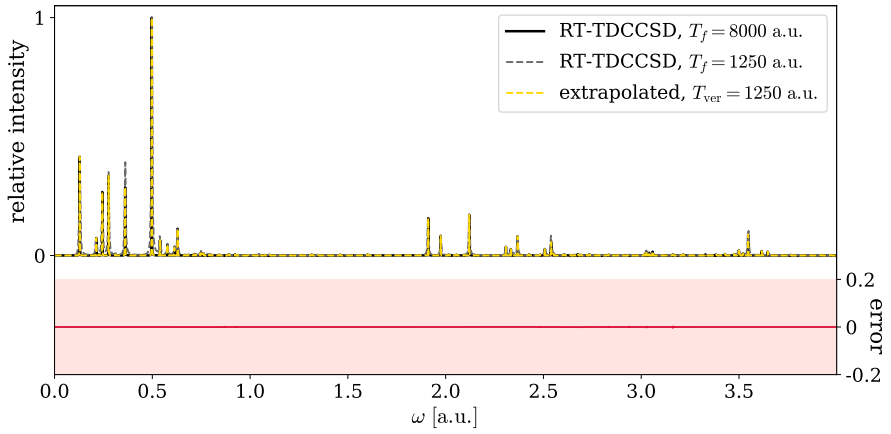

Figure 11.16: Evaluation of the extrapolation of $\mu^z(t)$ of LiH from 1250 a.u. to 8000 a.u. using OLS. The spectrum of the extrapolation $\tilde{I}_z(\omega)$ is shown in yellow, the spectrum of the short trajectory is gray and long trajectory spectrum $I_z(\omega)$ is shown in black. The red area shows the error $\tilde{I}_z(\omega) - I_z(\omega)$.

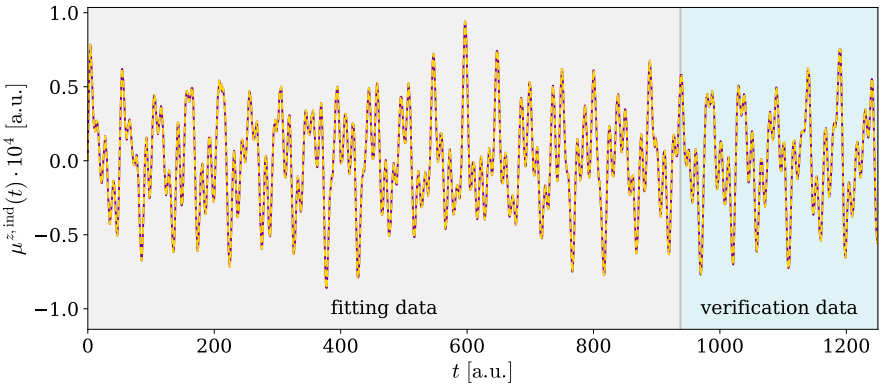

Figure 11.17: Comparison of the RT-TDCCSD dipole moment $\mu^z(t)$ of LiH (purple solid line) and its approximation $\tilde{\mu}^z(t)$ (yellow dashed line).

is shown in Fig. 11.18, where the approximated spectrum is close to true high resolution spectrum. The spectrum of the dipole data used in the extrapolation is quite crude, losing information about several of the peaks present in the spectrum. The inaccuracies of the spectrum of the extrapolation are not easily observable, with the exception of two narrowly spaced frequencies with opposite amplitudes at $\omega \approx 3.1$ a.u.. Some additional discrepancies are visible in the error area below the spectra, where $\tilde{I}_z(\omega) - I_z(\omega)$ is shown. The other cases $T_{\text{ver}} \in [500, 750]$ a.u. gave similar extrapolation spectra, but without the visible error at $\omega \approx 3.1$ a.u.. The extrapolation spectrum in Fig. 11.18 is very similar

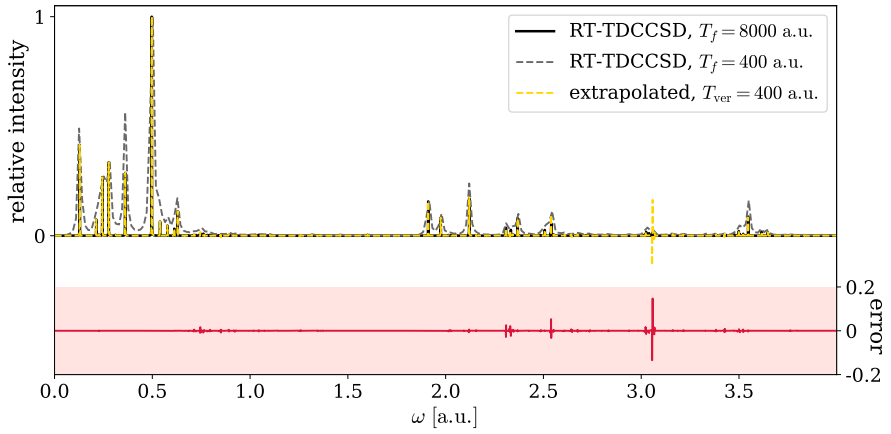

Figure 11.18: Evaluation of the extrapolation of $\mu^z(t)$ of LiH from 400 a.u. to 8000 a.u. using OLS. The spectrum of the extrapolation $\tilde{I}_z(\omega)$ is shown in yellow, the spectrum of the short trajectory is gray and long trajectory spectrum $I_z(\omega)$ is shown in black. The red area shows the error $\tilde{I}_z(\omega) - I_z(\omega)$.

to the spectra obtained when using $T_{\text{ver}} = 200$ a.u. and $T_{\text{ver}} = 300$ a.u., even though the verification error of these two extrapolations is ten times higher. The error in the verification window ($E_{\text{ver}} = 3 \cdot 10^{-4}$) is too small to see in Fig. 11.19, where the dipole moment $\mu^z(t)$ and its approximation $\tilde{\mu}^z(t)$ is shown

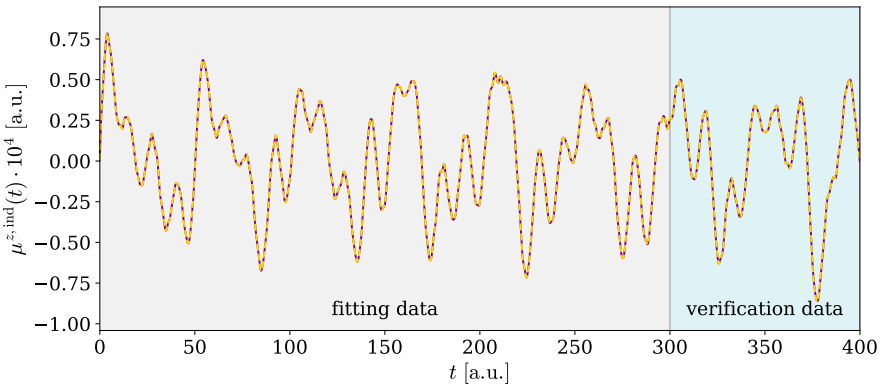

Figure 11.19: Comparison of the RT-TDCCSD dipole moment $\mu^z(t)$ of LiH (purple solid line) and its approximation $\tilde{\mu}^z(t)$ (yellow dashed line).

on the interval used for the extrapolation in Fig. 11.18.

Extrapolations using $T_{\text{ver}} \in [10, 75]$ a.u. all had large verification error ($E_{\text{ver}} \geq 1$) and extrapolation error ($E_{\text{full}} \geq 1$). Not surprisingly, the approximated spectra were all of poor quality. The verification error when using $T_{\text{ver}} = 100$ a.u. and $T_{\text{ver}} = 150$ a.u. was $E_{\text{ver}} \sim 10^{-1}$. The case using

$T_{\text{ver}} = 100$ a.u. shows more signs of over-fitting ($E_{\text{ver}}/E_{\text{fit}} = 2 \cdot 10^2$) compared to the fitting using $T_{\text{ver}} = 150$ a.u. ($E_{\text{ver}}/E_{\text{fit}} = 6 \cdot 10$). In both cases, the extrapolation spectra showed significant errors, but the $T_{\text{ver}} = 150$ a.u. trajectory gave a visibly better approximation.

11.1.5 The Water Molecule

The simulations of the water molecule, using the aug-cc-pVDZ basis set, sampled the dipole moment $\mu^z(t)$ up to $T_{\text{full}} = 8000$ a.u.. The error from the extrapolation using different trajectory lengths is given in Table 11.5.

Table 11.5: Coefficient of determination when fitting $\mu^z(t)$ of H_2O using OLS.

$\boldsymbol{T}_{\text{ver}}$ [a.u.]	$\boldsymbol{E}_{\text{fit}}$	$\boldsymbol{E}_{\text{ver}}$	$\boldsymbol{E}_{\text{full}}$	$\boldsymbol{E}_{\text{ver}}/\boldsymbol{E}_{\text{fit}}$
10	$1 \cdot 10^{-3}$	$1 \cdot 10^{-1}$	4	$9 \cdot 10$
20	$9 \cdot 10^{-3}$	$6 \cdot 10^{-1}$	$5 \cdot 10$	$6 \cdot 10$
50	$7 \cdot 10^{-3}$	$1 \cdot 10^{-1}$	3	$2 \cdot 10$
75	$4 \cdot 10^{-3}$	$2 \cdot 10^{-1}$	2	$4 \cdot 10$
100	$2 \cdot 10^{-3}$	$7 \cdot 10^{-2}$	$4 \cdot 10$	$3 \cdot 10$
150	$3 \cdot 10^{-3}$	$3 \cdot 10^{-1}$	2	$8 \cdot 10$
200	$1 \cdot 10^{-3}$	$1 \cdot 10^{-1}$	2	$1 \cdot 10^2$
300	$2 \cdot 10^{-3}$	$6 \cdot 10^{-2}$	1	$3 \cdot 10$
400	$2 \cdot 10^{-3}$	$1 \cdot 10^{-1}$	1	$5 \cdot 10$
500	$8 \cdot 10^{-4}$	$2 \cdot 10^{-1}$	$6 \cdot 10^{-1}$	$3 \cdot 10^2$
600	$6 \cdot 10^{-4}$	$3 \cdot 10^{-2}$	$5 \cdot 10^{-1}$	$4 \cdot 10$
750	$2 \cdot 10^{-3}$	$2 \cdot 10^{-2}$	$5 \cdot 10^{-1}$	$1 \cdot 10$
1000	$1 \cdot 10^{-4}$	$4 \cdot 10^{-2}$	$6 \cdot 10^{-1}$	$4 \cdot 10^2$
1250	$1 \cdot 10^{-4}$	$2 \cdot 10^{-3}$	$2 \cdot 10^{-2}$	$2 \cdot 10$
1500	$7 \cdot 10^{-5}$	$1 \cdot 10^{-3}$	$1 \cdot 10^{-2}$	$2 \cdot 10$
1750	$6 \cdot 10^{-5}$	$5 \cdot 10^{-3}$	$2 \cdot 10^{-2}$	$9 \cdot 10$

In the case of the water molecule, a perfect spectrum was not achieved for any of the T_{ver} included in the study. The results when using $T_{\text{ver}} \geq 1250$ a.u. were very similar, with an extrapolation error of $E_{\text{full}} \sim 10^{-2}$ and a verification error of $E_{\text{ver}} \sim 10^{-3}$. The resulting approximated spectrum is quite close to the real high resolution spectrum, as seen in Fig. 11.20. The error is not easily visible in the (relatively) dense spectrum, but the inaccuracies are exposed in the error area showing $\tilde{I}_z(\omega) - I_z(\omega)$ below the spectra. The spectral resolution when using dipole trajectory on $t_n \in [t_0, T_{\text{ver}}]$ for the Fourier-transform is also quite decent. The dipole trajectory used for the dipole approximation in Fig. 11.16, along with its approximation, is shown in Fig. 11.17. There is no visible difference between the real dipole moment $\mu^z(t)$ of the water molecule and its approximation, $\tilde{\mu}^z(t)$.

At this point there is reason to fear that the density of the spectrum increases the difficulty of the dipole moment extrapolation. The length of the trajectory needed for a successful extrapolation seems to increase with the size and complexity of the system. This is not too surprising, as the main difficulty of the dipole fitting is the frequency estimation. The frequency estimation is in terms limited by the convergence of the Fourier-Padé approximant. The challenge of dense spectra is a common problem for all methods of harmonic

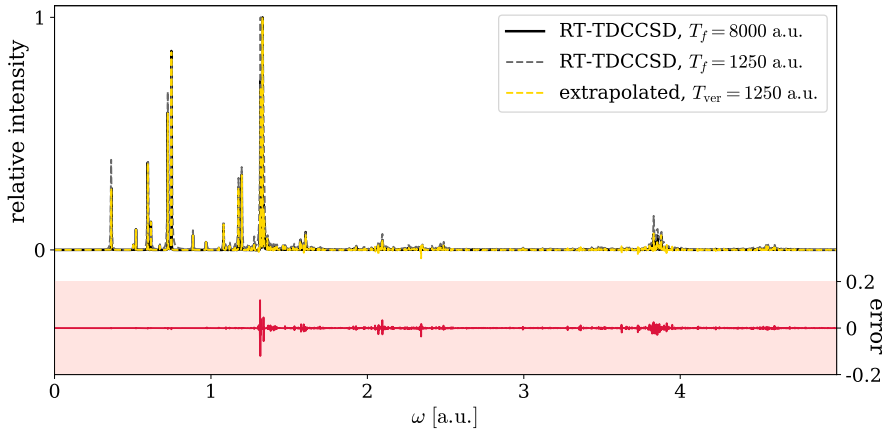

Figure 11.20: Evaluation of the extrapolation of $\mu^z(t)$ of H_2O from 1250 a.u. to 8000 a.u. using OLS. The spectrum of the extrapolation $\tilde{I}_z(\omega)$ is shown in yellow, the spectrum of the short trajectory is gray and long trajectory spectrum $I_z(\omega)$ is shown in black. The red area shows the error $\tilde{I}_z(\omega) - I_z(\omega)$.

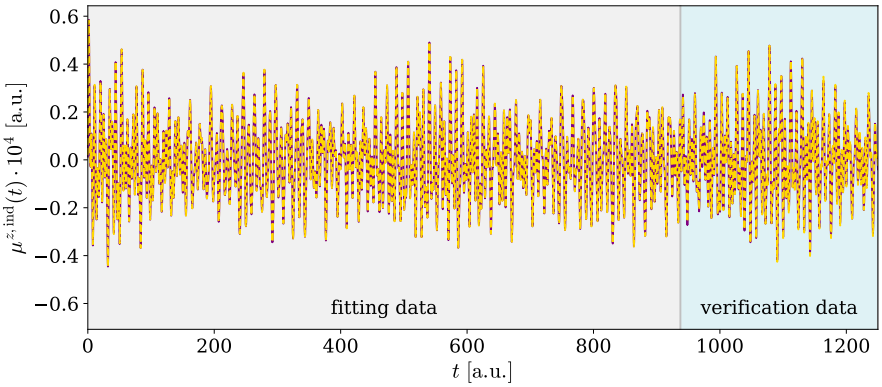

Figure 11.21: Comparison of the RT-TDCCSD dipole moment $\mu^z(t)$ of H_2O (purple solid line) and its approximation $\tilde{\mu}^z(t)$ (yellow dashed line).

inversion.[1] The MO decomposition used to remedy this problem for the Fourier-Padé approximant of RT-TDDFT absorption spectra in the work of Bruner et al.[12] will be studied in Section 12.3 for the RT-TDCCSD simulations in this project.

The extrapolation using $T_{\text{ver}} = 400$ a.u. shows a significant verification error $E_{\text{ver}} = 2 \cdot 10^{-1}$ and extrapolation error $E_{\text{ver}} = 6 \cdot 10^{-1}$. The resulting spectrum of the extrapolated dipole moment deviates visibly from the true high resolution spectrum, as seen in Fig. 11.22. The approximated spectrum coincides well with the true spectrum for low frequencies $\omega < 1.1$ a.u., although

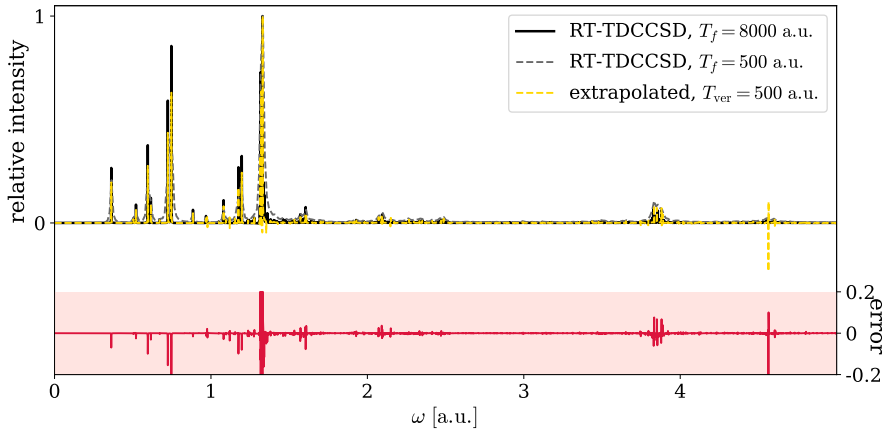

Figure 11.22: Evaluation of the extrapolation of $\mu^z(t)$ of H_2O from 500 a.u. to 8000 a.u. using OLS. The spectrum of the extrapolation $\tilde{I}_z(\omega)$ is shown in yellow, the spectrum of the short trajectory is gray and long trajectory spectrum $I_z(\omega)$ is shown in black. The red area shows the error $\tilde{I}_z(\omega) - I_z(\omega)$. (I).

the normalization using a faulty peak at $\omega \approx 1.4$ a.u. consistently reduces the height of the peaks of the approximated spectrum. The approximated spectrum starts to deviate significantly for larger ω. This includes two phantom peaks with opposite sign near $\omega = 4.6$ a.u., and the extrapolation spectrum is quite erroneous around the dense part at $\omega = 1.4$ a.u.. As seen in Fig. 11.22, the

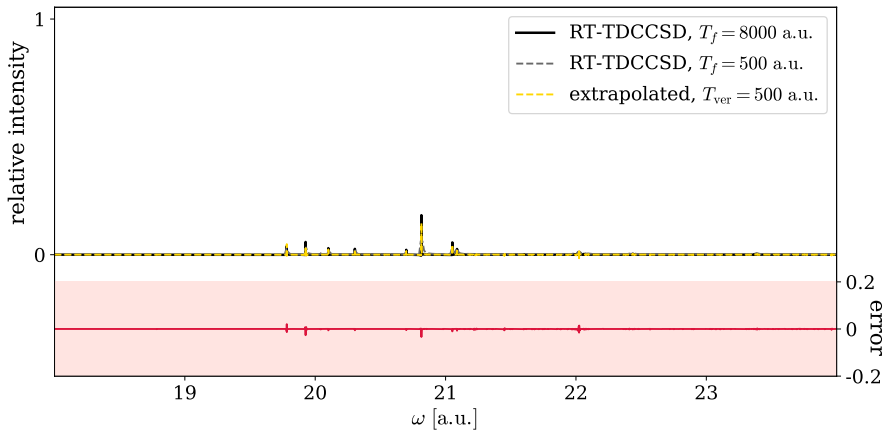

Figure 11.23: Evaluation of the extrapolation of $\mu^z(t)$ of H_2O from 500 a.u. to 8000 a.u. using OLS. The spectrum of the extrapolation $\tilde{I}_z(\omega)$ is shown in yellow, the spectrum of the short trajectory is gray and long trajectory spectrum $I_z(\omega)$ is shown in black. The red area shows the error $\tilde{I}_z(\omega) - I_z(\omega)$.

spectrum of the water molecule contains some very high energy transitions. This figure is a continuation of the spectrum in Fig. 11.22. This part of the spectrum is commonly discarded, but errors in this area will be present in the evaluation of the fitting. The dipole trajectory used for the extrapolation yielding the spectrum shown Figs. 11.22 and 11.23, along with its approximation, is shown in Fig. 11.24. The difference between the dipole moment $\mu^z(t)$ and its

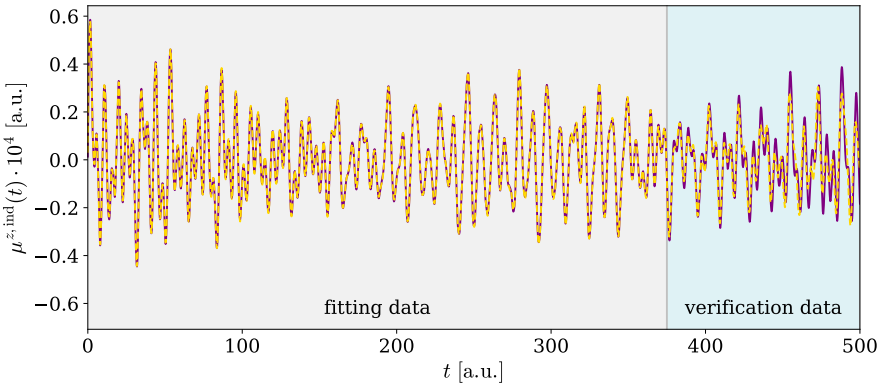

Figure 11.24: Comparison of the RT-TDCCSD dipole moment $\mu^z(t)$ of H_2O (purple solid line) and its approximation $\tilde{\mu}^z(t)$ (yellow dashed line).

approximation $\tilde{\mu}^z(t)$ is apparent on the verification data.

The extrapolation error when using $T_{\mathrm{ver}} < 400$ a.u. is quite high, as seen in Table 11.5. The approximated spectra in all these cases are poor. It was observed that the dominant peak in all these cases came from a cluster of pollution in the spectrum, of the same type that can be seen at $\omega \approx 4.6$ a.u. in Fig. 11.22.

11.2 Fitting Using LASSO

The simulations in Section 11.1 were repeated, this time using the LASSO method for determining the coefficients. The estimated frequencies are the same, and the approximated dipole moment $\tilde{\mu}^z(t)$ in these studies and the studies in Section 11.1 differ only in the linear coefficients.

The LASSO method is iterative and terminates either if the error is lower than a tolerance δ, or an upper limit for the number of iterations N_{iter} is reached. The maximum number of iterations was set to

$$N_{\mathrm{iter}} = 200 N_\omega, \tag{11.6}$$

where N_ω is the number of estimated frequencies. The number of iterations was set relative to the number of unknowns ($2N_\omega$), as each iteration only updates one coefficient. This leaves an average of 100 iterations per parameter. The tolerance parameter was set relative to the magnitude of the induced dipole moment on the fitting trajectory $t_n \in [t_0, T_{\mathrm{fit}}]$:

$$\delta = 10^{-6} \cdot \frac{\max_n \mu^z(t_n) - \min_n \mu^z(t_n)}{2}. \tag{11.7}$$

The shrinkage parameter was similarly set to

$$\lambda = 10^{-8} \cdot \frac{\max_n \mu^z(t_n) - \min_n \mu^z(t_n)}{2}. \tag{11.8}$$

All the sign of the coefficients of sine and cosine in $\tilde{\mu}^z(t)$ were forced to follow the form of linear response theory in Eq. (4.25). The coefficients were updated in random order, setting the parameter `random_state` to 42 for reproducibility. The details are otherwise as described in the beginning of this chapter.

11.2.1 The Helium Atom

The error from the extrapolation of the dipole moment of helium using the aug-cc-pVTZ basis set is presented in Table 11.6. The dipole moment $\mu^z(t)$ was sampled up to $T_{\text{full}} = 6000$ a.u.. The extrapolation error when using

Table 11.6: Coefficient of determination when fitting $\mu^z(t)$ of He using LASSO.

$\boldsymbol{T}_{\text{ver}}$ [a.u.]	$\boldsymbol{E}_{\text{fit}}$	$\boldsymbol{E}_{\text{ver}}$	$\boldsymbol{E}_{\text{full}}$	$\boldsymbol{E}_{\text{ver}}/\boldsymbol{E}_{\text{fit}}$
10	$7 \cdot 10^{-8}$	$4 \cdot 10^{-5}$	$1 \cdot 10^{-1}$	$6 \cdot 10^{2}$
20	$1 \cdot 10^{-10}$	$1 \cdot 10^{-10}$	$2 \cdot 10^{-8}$	1
50	$4 \cdot 10^{-12}$	$5 \cdot 10^{-12}$	$1 \cdot 10^{-8}$	1
75	$2 \cdot 10^{-13}$	$3 \cdot 10^{-12}$	$1 \cdot 10^{-8}$	$2 \cdot 10$
100	$4 \cdot 10^{-13}$	$4 \cdot 10^{-12}$	$1 \cdot 10^{-8}$	9
150	$1 \cdot 10^{-12}$	$5 \cdot 10^{-12}$	$1 \cdot 10^{-8}$	6
200	$2 \cdot 10^{-12}$	$2 \cdot 10^{-11}$	$1 \cdot 10^{-8}$	8
300	$6 \cdot 10^{-12}$	$6 \cdot 10^{-11}$	$2 \cdot 10^{-8}$	$1 \cdot 10$
400	$7 \cdot 10^{-12}$	$8 \cdot 10^{-11}$	$1 \cdot 10^{-8}$	$1 \cdot 10$
500	$9 \cdot 10^{-12}$	$1 \cdot 10^{-10}$	$1 \cdot 10^{-8}$	$1 \cdot 10$
600	$1 \cdot 10^{-11}$	$2 \cdot 10^{-10}$	$1 \cdot 10^{-8}$	$1 \cdot 10$
750	$3 \cdot 10^{-11}$	$2 \cdot 10^{-10}$	$1 \cdot 10^{-8}$	9
1000	$5 \cdot 10^{-11}$	$3 \cdot 10^{-10}$	$1 \cdot 10^{-8}$	6
1250	$4 \cdot 10^{-11}$	$5 \cdot 10^{-10}$	$1 \cdot 10^{-8}$	$1 \cdot 10$
1500	$8 \cdot 10^{-11}$	$8 \cdot 10^{-10}$	$1 \cdot 10^{-8}$	$1 \cdot 10$
1750	$3 \cdot 10^{-10}$	$1 \cdot 10^{-9}$	$1 \cdot 10^{-8}$	6

LASSO is very similar to the extrapolation error in Table 11.1 using OLS. In both cases, the shortest trajectory $T_{\text{ver}} = 10$ a.u. gives the extrapolation error $E_{\text{full}} = 1 \cdot 10^{-1}$, while all the other trajectory lengths give almost insignificant extrapolation error, $E_{\text{full}} \sim 10^{-8}$.

Both examples ($T_{\text{ver}} = 10$ a.u. and $T_{\text{ver}} = 20$ a.u.) of the helium atom shown in greater detail when using OLS in Section 11.1.1 give the same spectra when extrapolating using the LASSO method. The spectrum obtained by extrapolating the dipole moment using $T_{\text{ver}} = 20$ a.u. in Fig. 11.25 is a perfect fit on the true high resolution spectrum, just like the OLS extrapolation in Fig. 11.1.

The less accurate extrapolation using $T_{\text{ver}} = 10$ a.u. shown in Fig. 11.26 is visibly different from the true high resolution spectrum. The extrapolation spectrum using LASSO is indistinguishable from the extrapolation using OLS in Fig. 11.3.

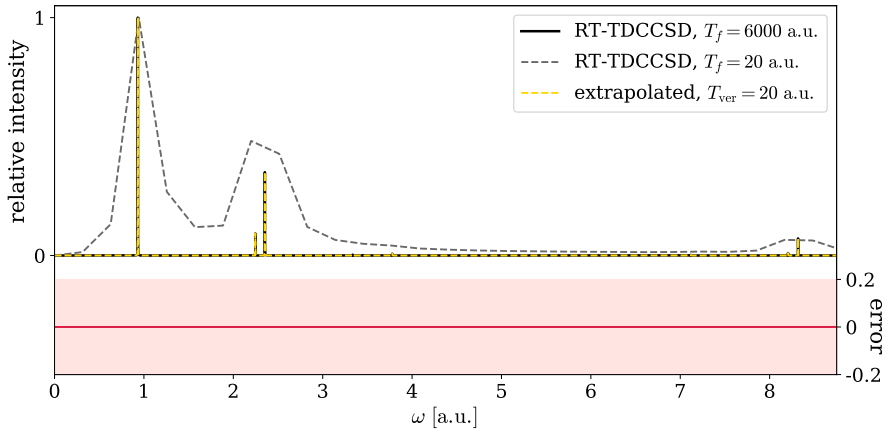

Figure 11.25: Evaluation of the extrapolation of $\mu^z(t)$ of He from 20 a.u. to 6000 a.u. using LASSO. The spectrum of the extrapolation $\tilde{I}_z(\omega)$ is shown in yellow, the spectrum of the short trajectory is gray and long trajectory spectrum $I_z(\omega)$ is shown in black. The red area shows the error $\tilde{I}_z(\omega) - I_z(\omega)$.

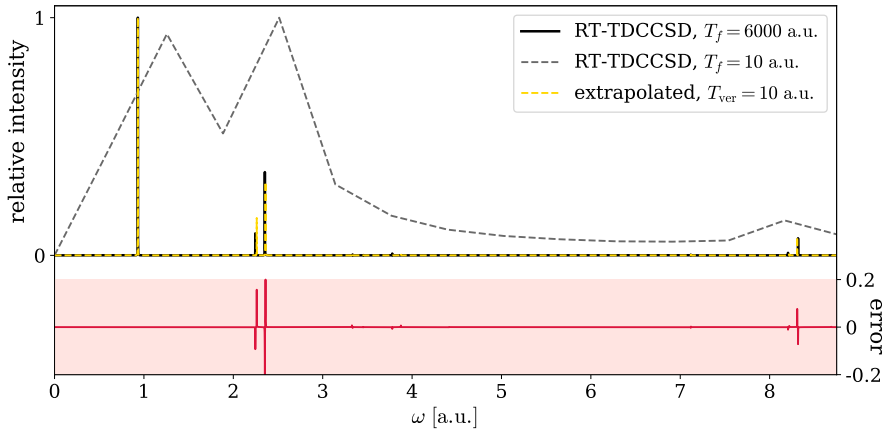

Figure 11.26: Evaluation of the extrapolation of $\mu^z(t)$ of He from 10 a.u. to 6000 a.u. using LASSO. The spectrum of the extrapolation $\tilde{I}_z(\omega)$ is shown in yellow, the spectrum of the short trajectory is gray and long trajectory spectrum $I_z(\omega)$ is shown in black. The red area shows the error $\tilde{I}_z(\omega) - I_z(\omega)$.

11.2.2 The Hydrogen Molecule

The dipole moment $\mu^z(t)$ of the hydrogen molecule using the aug-cc-pVTZ basis was sampled up to $T_{\text{full}} = 8000$ a.u.. The error in the fitted function $\tilde{\mu}^z(t)$ is shown in Table 11.7. As for the helium atom, the extrapolation error E_{full} of the hydrogen molecule is almost the same when using OLS and LASSO for

Table 11.7: Coefficient of determination when fitting $\mu^z(t)$ of H_2 using LASSO.

T_{ver} [a.u.]	E_{fit}	E_{ver}	E_{full}	$E_{\text{ver}}/E_{\text{fit}}$
10	$2 \cdot 10^{-3}$	$3 \cdot 10$	3	$2 \cdot 10^{4}$
20	$4 \cdot 10^{-3}$	1	2	$3 \cdot 10^{2}$
50	$4 \cdot 10^{-7}$	$8 \cdot 10^{-6}$	$1 \cdot 10^{-3}$	$2 \cdot 10$
75	$8 \cdot 10^{-8}$	$3 \cdot 10^{-7}$	$1 \cdot 10^{-4}$	4
100	$2 \cdot 10^{-8}$	$8 \cdot 10^{-8}$	$6 \cdot 10^{-6}$	4
150	$4 \cdot 10^{-9}$	$2 \cdot 10^{-8}$	$6 \cdot 10^{-6}$	4
200	$2 \cdot 10^{-10}$	$1 \cdot 10^{-8}$	$5 \cdot 10^{-6}$	$5 \cdot 10$
300	$4 \cdot 10^{-11}$	$2 \cdot 10^{-10}$	$1 \cdot 10^{-7}$	4
400	$3 \cdot 10^{-11}$	$2 \cdot 10^{-10}$	$1 \cdot 10^{-7}$	8
500	$8 \cdot 10^{-11}$	$2 \cdot 10^{-10}$	$1 \cdot 10^{-8}$	3
600	$1 \cdot 10^{-10}$	$2 \cdot 10^{-10}$	$1 \cdot 10^{-8}$	1
750	$1 \cdot 10^{-10}$	$3 \cdot 10^{-10}$	$2 \cdot 10^{-8}$	2
1000	$5 \cdot 10^{-8}$	$5 \cdot 10^{-8}$	$6 \cdot 10^{-8}$	1
1250	$2 \cdot 10^{-10}$	$7 \cdot 10^{-10}$	$1 \cdot 10^{-8}$	3
1500	$3 \cdot 10^{-10}$	$1 \cdot 10^{-9}$	$1 \cdot 10^{-8}$	4
1750	$3 \cdot 10^{-10}$	$2 \cdot 10^{-9}$	$1 \cdot 10^{-8}$	5

optimizing the linear coefficients.

The example using $T_{\text{ver}} = 100$ a.u. showed a slight improvement of the LASSO method ($E_{\text{ver}} = 6 \cdot 10^{-9}$) compared to the OLS method ($E_{\text{ver}} = 9 \cdot 10^{-9}$). While the error on the fitting data was ten times lower when using OLS ($E_{\text{fit}} = 1 \cdot 10^{-9}$) compared to LASSO ($E_{\text{fit}} = 2 \cdot 10^{-8}$), LASSO showed no sign of over-fitting ($E_{\text{ver}}/E_{\text{fit}} = 4$) while OLS shows increase in error from the fitting data to the verification data ($E_{\text{ver}}/E_{\text{fit}} = 1 \cdot 10^{2}$). The spectrum from the extrapolation using LASSO is shown in Fig. 11.27. It is not possible to observe

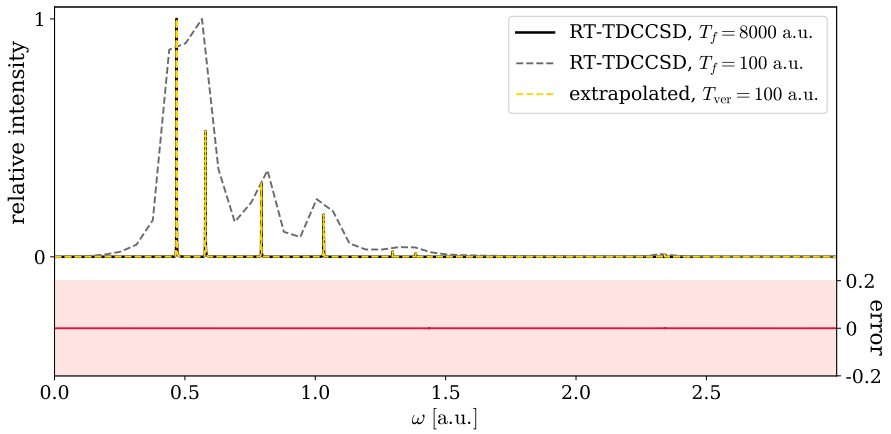

Figure 11.27: Evaluation of the extrapolation of $\mu^z(t)$ of H_2 from 100 a.u. to 8000 a.u. using LASSO. The spectrum of the extrapolation $\tilde{I}_z(\omega)$ is shown in yellow, the spectrum of the short trajectory is gray and long trajectory spectrum $I_z(\omega)$ is shown in black. The red area shows the error $\tilde{I}_z(\omega) - I_z(\omega)$.

any difference between the extrapolated spectrum and the true high resolution spectrum. The spectrum obtained by the extrapolation using OLS shown in Fig. 11.5 has a small error around $\omega = 2.3$ a.u., only visible in the error area below the spectrum. The LASSO method provides a negligible improvement in this case.

When the shorter trajectory ($T_{\text{ver}} = 20$ a.u.) was used, the extrapolation error was the same ($E_{\text{full}} = 2$) independent of the linear optimizing method. LASSO showed less signs of over-fitting ($E_{\text{ver}}/E_{\text{fit}} = 3 \cdot 10^2$) compared to OLS ($E_{\text{ver}}/E_{\text{fit}} = 5 \cdot 10^4$). The spectrum from the fitted function $\tilde{\mu}^z(t)$ using LASSO in Fig. 11.28 is identical to that using OLS in Fig. 11.9.

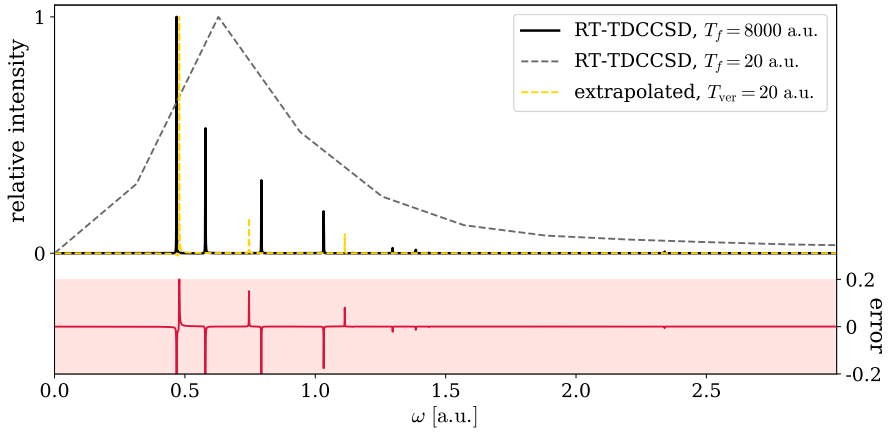

Figure 11.28: Evaluation of the extrapolation of $\mu^z(t)$ of H_2 from 50 a.u. to 8000 a.u. using LASSO. The spectrum of the extrapolation $\tilde{I}_z(\omega)$ is shown in yellow, the spectrum of the short trajectory is gray and long trajectory spectrum $I_z(\omega)$ is shown in black. The red area shows the error $\tilde{I}_z(\omega) - I_z(\omega)$.

11.2.3 The Beryllium Atom

The error of the extrapolation of $\mu^z(t)$ of the beryllium atom calculated using the aug-cc-pVTZ basis set is found in Table 11.8. The full extrapolation was to $T_{\text{full}} = 6000$ a.u.. The extrapolation error is very similar to what is found in Table 11.3 when using the OLS method for optimizing the linear coefficients. The jump in error from the fitting data to the verification data is generally higher when using the OLS method compared to LASSO on shorter trajectories $T_{\text{ver}} \leq 400$ a.u..

The approximated spectrum obtained from extrapolating the $T_{\text{ver}} = 150$ a.u. trajectory is shown in Fig. 11.29. The extrapolation error was $E_{\text{full}} = 2 \cdot 10^{-5}$ independent of the method used for the linear regression. Both extrapolation spectra, using LASSO in Fig. 11.29 and OLS in Fig. 11.11 have the same, negligible small errors compared to the true high resolution spectrum.

The extrapolation error when using $T_{\text{ver}} = 50$ a.u. was $E_{\text{full}} = 2 \cdot 10^{-1}$ for both methods for linear regression. The resulting spectra are however quite different. All the errors in the absorption spectrum of $\tilde{\mu}^z(t)$ using LASSO in

Table 11.8: Coefficient of determination when fitting $\mu^z(t)$ of Be using LASSO.

$\boldsymbol{T}_{\text{ver}}$ [a.u.]	$\boldsymbol{E}_{\text{fit}}$	$\boldsymbol{E}_{\text{ver}}$	$\boldsymbol{E}_{\text{full}}$	$\boldsymbol{E}_{\text{ver}}/\boldsymbol{E}_{\text{fit}}$
10	$4 \cdot 10^{-6}$	$9 \cdot 10^{-1}$	3	$2 \cdot 10^{5}$
20	$2 \cdot 10^{-4}$	$4 \cdot 10^{-2}$	$9 \cdot 10^{-1}$	$2 \cdot 10^{2}$
50	$5 \cdot 10^{-5}$	$3 \cdot 10^{-4}$	$2 \cdot 10^{-1}$	5
75	$4 \cdot 10^{-6}$	$4 \cdot 10^{-5}$	$4 \cdot 10^{-3}$	$1 \cdot 10$
100	$2 \cdot 10^{-6}$	$3 \cdot 10^{-5}$	$2 \cdot 10^{-3}$	$1 \cdot 10$
150	$1 \cdot 10^{-8}$	$4 \cdot 10^{-8}$	$2 \cdot 10^{-5}$	3
200	$2 \cdot 10^{-10}$	$3 \cdot 10^{-9}$	$6 \cdot 10^{-7}$	$1 \cdot 10$
300	$3 \cdot 10^{-10}$	$3 \cdot 10^{-9}$	$3 \cdot 10^{-7}$	$1 \cdot 10$
400	$4 \cdot 10^{-11}$	$5 \cdot 10^{-11}$	$1 \cdot 10^{-9}$	1
500	$3 \cdot 10^{-11}$	$3 \cdot 10^{-11}$	$5 \cdot 10^{-10}$	1
600	$2 \cdot 10^{-12}$	$7 \cdot 10^{-12}$	$5 \cdot 10^{-10}$	3
750	$1 \cdot 10^{-10}$	$1 \cdot 10^{-10}$	$5 \cdot 10^{-10}$	1
1000	$2 \cdot 10^{-10}$	$3 \cdot 10^{-10}$	$6 \cdot 10^{-10}$	1
1250	$2 \cdot 10^{-9}$	$2 \cdot 10^{-9}$	$3 \cdot 10^{-9}$	1
1500	$2 \cdot 10^{-8}$	$2 \cdot 10^{-8}$	$2 \cdot 10^{-8}$	1
1750	$2 \cdot 10^{-8}$	$2 \cdot 10^{-8}$	$2 \cdot 10^{-8}$	1

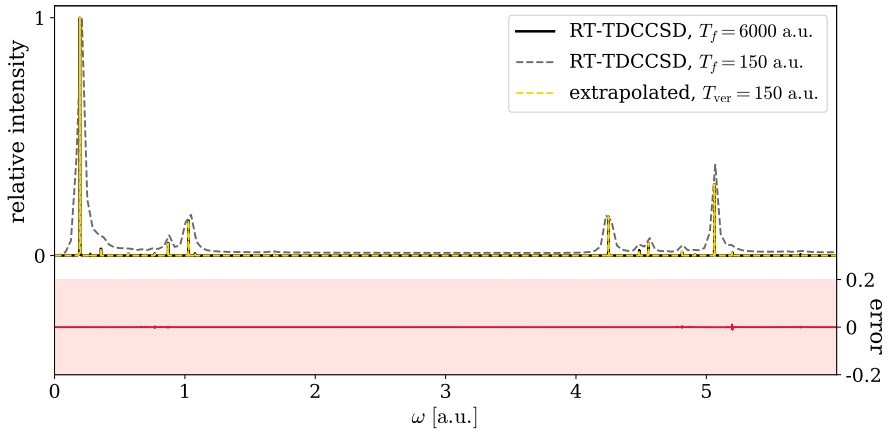

Figure 11.29: Evaluation of the extrapolation of $\mu^z(t)$ of Be from 150 a.u. to 6000 a.u. using LASSO. The spectrum of the extrapolation $\tilde{I}_z(\omega)$ is shown in yellow, the spectrum of the short trajectory is gray and long trajectory spectrum $I_z(\omega)$ is shown in black. The red area shows the error $\tilde{I}_z(\omega) - I_z(\omega)$.

Fig. 11.30 can also be seen in Fig. 11.13. The spectrum using OLS has an additional error, where the spectrum seems to *oscillate* around $\omega \approx 4.8$ a.u., as well as two narrowly spaced peaks with opposite sign at $\omega \approx 0.9$ a.u.. These errors are eliminated when forcing all coefficients to be positive. In this case, the extrapolation spectrum obtained using LASSO to enforce positive coefficients gave a better approximation to the true high resolution spectrum.

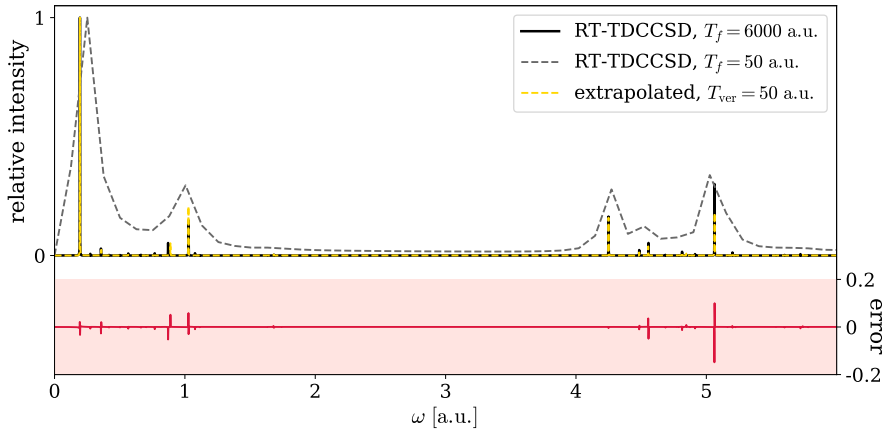

Figure 11.30: Evaluation of the extrapolation of $\mu^z(t)$ of Be from 50 a.u. to 6000 a.u. using LASSO. The spectrum of the extrapolation $\tilde{I}_z(\omega)$ is shown in yellow, the spectrum of the short trajectory is gray and long trajectory spectrum $I_z(\omega)$ is shown in black. The red area shows the error $\tilde{I}_z(\omega) - I_z(\omega)$.

11.2.4 Lithium Hydride

The lithium hydride calculations using aug-cc-pVDZ sampled the z-component of the dipole moment up to $T_{\text{full}} = 8000$ a.u.. The error in the fitting of μ^z using LASSO is found in Table 11.9. The extrapolation error is either exactly

Table 11.9: Coefficient of determination when fitting $\mu^z(t)$ of LiH using LASSO.

T_{ver} [a.u.]	E_{fit}	E_{ver}	E_{full}	$E_{\text{ver}}/E_{\text{fit}}$
10	$7 \cdot 10^{-1}$	3	3	5
20	$5 \cdot 10^{-2}$	$6 \cdot 10^{-1}$	2	$1 \cdot 10$
50	$6 \cdot 10^{-1}$	$1 \cdot 10$	1	$2 \cdot 10$
75	$2 \cdot 10^{-2}$	$8 \cdot 10^{-1}$	2	$3 \cdot 10$
100	$1 \cdot 10^{-2}$	$6 \cdot 10^{-1}$	2	$5 \cdot 10$
150	$2 \cdot 10^{-2}$	$2 \cdot 10^{-1}$	1	$1 \cdot 10$
200	$5 \cdot 10^{-4}$	$2 \cdot 10^{-3}$	$3 \cdot 10^{-1}$	5
300	$2 \cdot 10^{-5}$	$2 \cdot 10^{-4}$	$6 \cdot 10^{-3}$	$1 \cdot 10$
400	$1 \cdot 10^{-5}$	$3 \cdot 10^{-5}$	$4 \cdot 10^{-4}$	3
500	$5 \cdot 10^{-6}$	$7 \cdot 10^{-5}$	$3 \cdot 10^{-4}$	$1 \cdot 10$
600	$7 \cdot 10^{-6}$	$2 \cdot 10^{-5}$	$3 \cdot 10^{-4}$	3
750	$7 \cdot 10^{-6}$	$7 \cdot 10^{-5}$	$3 \cdot 10^{-4}$	$1 \cdot 10$
1000	$3 \cdot 10^{-7}$	$2 \cdot 10^{-6}$	$2 \cdot 10^{-5}$	8
1250	$3 \cdot 10^{-8}$	$3 \cdot 10^{-7}$	$3 \cdot 10^{-6}$	8
1500	$2 \cdot 10^{-8}$	$7 \cdot 10^{-8}$	$3 \cdot 10^{-7}$	4
1750	$1 \cdot 10^{-8}$	$9 \cdot 10^{-8}$	$1 \cdot 10^{-7}$	8

the same or marginally lower compared to the error of OLS fitting found in Table 11.4. The jump in error $E_{\text{ver}}/E_{\text{fit}}$ is consistently lower for the LASSO

method, often by a factor of 10.

The extrapolation using $T_{\text{ver}} = 1250$ a.u. gives a spectrum indistinguishable from the true high resolution spectrum, as seen in Fig. 11.31. This was also the case when using OLS, as is shown in Fig. 11.16.

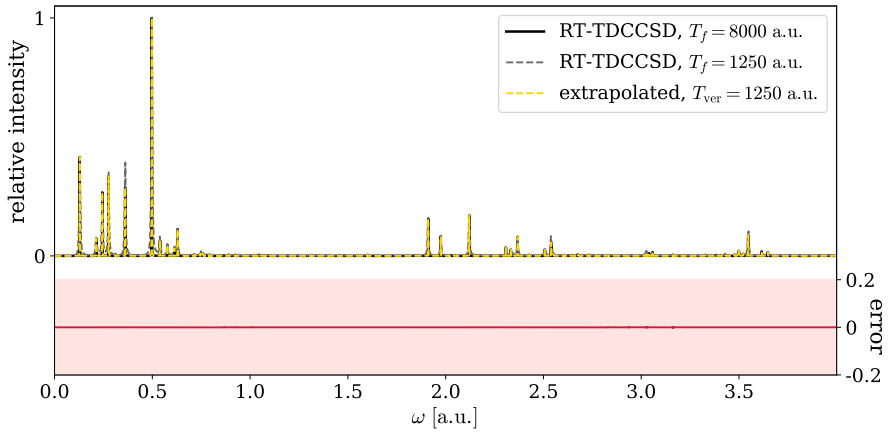

Figure 11.31: Evaluation of the extrapolation of $\mu^z(t)$ of LiH from 1250 a.u. to 8000 a.u. using LASSO. The spectrum of the extrapolation $\tilde{I}_z(\omega)$ is shown in yellow, the spectrum of the short trajectory is gray and long trajectory spectrum $I_z(\omega)$ is shown in black. The red area shows the error $\tilde{I}_z(\omega) - I_z(\omega)$.

The extrapolation spectrum using the $T_{\text{ver}} = 400$ a.u. trajectory is shown in Fig. 11.32. By comparing the error of the extrapolation OLS method and the

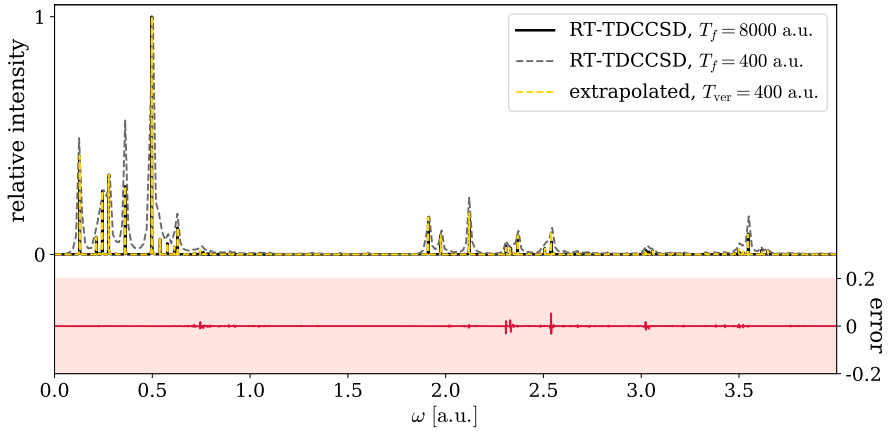

Figure 11.32: Evaluation of the extrapolation of $\mu^z(t)$ of LiH from 400 a.u. to 8000 a.u. using LASSO. The spectrum of the extrapolation $\tilde{I}_z(\omega)$ is shown in yellow, the spectrum of the short trajectory is gray and long trajectory spectrum $I_z(\omega)$ is shown in black. The red area shows the error $\tilde{I}_z(\omega) - I_z(\omega)$.

LASSO method when looking at the error tables for $T_{\text{ver}} = 400$ a.u., the results seem very similar. The extrapolation error of the OLS method ($E_{\text{full}} = 7 \cdot 10^{-4}$) is only slightly higher than that of LASSO ($E_{\text{full}} = 4 \cdot 10^{-4}$). The verification error was the same for both ($E_{\text{ver}} = 3 \cdot 10^{-5}$), while the jump in error was only twice as large for OLS ($E_{\text{ver}}/E_{\text{fit}} = 6$) compared to LASSO ($E_{\text{ver}}/E_{\text{fit}} = 3$). The spectra of the two methods are, however, quite different. The spectrum obtained by LASSO in Fig. 11.32, shows only small inaccuracies in the spectrum. The OLS spectrum in Fig. 11.18 has all the same minor errors as the LASSO-spectrum, as well as a clear error at $\omega \approx 3.1$ a.u.. This is the only easily visible error in the spectrum. In this case, the LASSO method outperforms the OLS method.

11.2.5 The Water Molecule

The z-component of the dipole moment was sampled up to $T_{\text{full}} = 8000$ a.u. when simulating absorption spectrum of the water molecule using the aug-cc-pVDZ basis set. The error in the approximated dipole moment $\tilde{\mu}^z(t)$ is shown in Table 11.10. Comparing the table to Table 11.5 using OLS reveals the same

Table 11.10: Coefficient of determination when fitting $\mu^z(t)$ of H_2O using LASSO.

$\boldsymbol{T}_{\text{ver}}$ [a.u.]	$\boldsymbol{E}_{\text{fit}}$	$\boldsymbol{E}_{\text{ver}}$	$\boldsymbol{E}_{\text{full}}$	$\boldsymbol{E}_{\text{ver}}/\boldsymbol{E}_{\text{fit}}$
10	$6 \cdot 10^{-3}$	$1 \cdot 10^{-1}$	4	$2 \cdot 10$
20	$1 \cdot 10^{-1}$	$8 \cdot 10^{-1}$	5	8
50	$1 \cdot 10^{-2}$	$7 \cdot 10^{-2}$	3	6
75	$5 \cdot 10^{-3}$	$2 \cdot 10^{-1}$	2	$3 \cdot 10$
100	$8 \cdot 10^{-3}$	$1 \cdot 10^{-1}$	2	$1 \cdot 10$
150	$8 \cdot 10^{-3}$	$3 \cdot 10^{-1}$	2	$4 \cdot 10$
200	$4 \cdot 10^{-3}$	$1 \cdot 10^{-1}$	1	$3 \cdot 10$
300	$5 \cdot 10^{-3}$	$1 \cdot 10^{-1}$	$7 \cdot 10^{-1}$	$2 \cdot 10$
400	$4 \cdot 10^{-3}$	$1 \cdot 10^{-1}$	$6 \cdot 10^{-1}$	$3 \cdot 10$
500	$2 \cdot 10^{-3}$	$1 \cdot 10^{-1}$	$5 \cdot 10^{-1}$	$6 \cdot 10$
600	$4 \cdot 10^{-3}$	$3 \cdot 10^{-2}$	$4 \cdot 10^{-1}$	7
750	$4 \cdot 10^{-3}$	$2 \cdot 10^{-2}$	$5 \cdot 10^{-1}$	4
1000	$5 \cdot 10^{-3}$	$3 \cdot 10^{-2}$	$4 \cdot 10^{-1}$	5
1250	$2 \cdot 10^{-4}$	$1 \cdot 10^{-3}$	$2 \cdot 10^{-2}$	8
1500	$2 \cdot 10^{-4}$	$2 \cdot 10^{-3}$	$1 \cdot 10^{-2}$	$1 \cdot 10$
1750	$1 \cdot 10^{-3}$	$6 \cdot 10^{-3}$	$8 \cdot 10^{-3}$	5

pattern as seen for lithium hydride. The extrapolation error E_{full} is slightly lower when using LASSO, and the ratio $E_{\text{ver}}/E_{\text{fit}}$ is consistently a higher when using OLS.

The approximated spectrum in Fig. 11.33 shows the result of the extrapolation using $T_{\text{ver}} = 1250$ a.u.. The error in the approximated spectrum is very similar to that in Fig. 11.20, using OLS.

The extrapolation spectrum using $T_{\text{ver}} = 400$ a.u. shown in Fig. 11.34 is an improvement over the OLS-spectrum shown in Fig. 11.22. There are several unwanted negative peaks in the OLS-spectrum which are not present in the LASSO-spectrum.

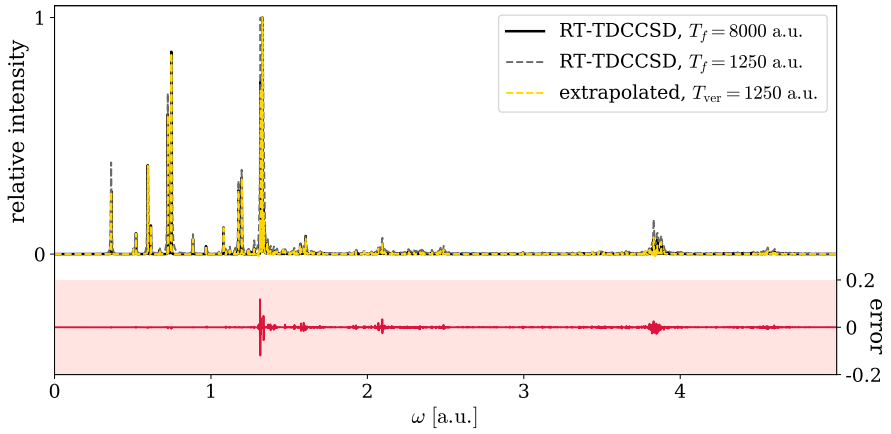

Figure 11.33: Evaluation of the extrapolation of $\mu^z(t)$ of H_2O from 1250 a.u. to 8000 a.u. using LASSO. The spectrum of the extrapolation $\tilde{I}_z(\omega)$ is shown in yellow, the spectrum of the short trajectory is gray and long trajectory spectrum $I_z(\omega)$ is shown in black. The red area shows the error $\tilde{I}_z(\omega) - I_z(\omega)$.

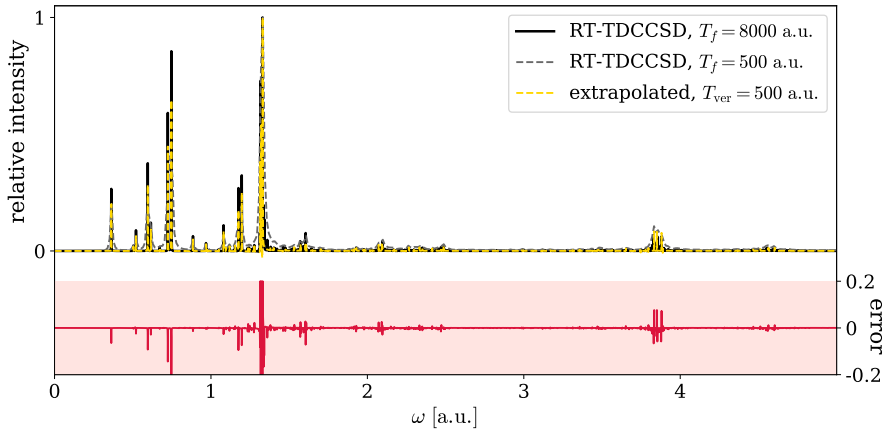

Figure 11.34: Evaluation of the extrapolation of $\mu^z(t)$ of H_2O from 500 a.u. to 8000 a.u. using LASSO. The spectrum of the extrapolation $\tilde{I}_z(\omega)$ is shown in yellow, the spectrum of the short trajectory is gray and long trajectory spectrum $I_z(\omega)$ is shown in black. The red area shows the error $\tilde{I}_z(\omega) - I_z(\omega)$.

There seems to be no clear way to correlate the verification error to the more qualitative assessment of the approximated spectra. The verification error when $T_{\text{ver}} < 600$ a.u. is $E_{\text{ver}} \sim 10^{-1}$. The extrapolation spectra using $T_{\text{ver}} < 600$ a.u. were all greatly improved by using LASSO compared to the OLS method. Using the LASSO method, the extrapolation spectrum using $T_{\text{ver}} = 10$ a.u. is very inaccurate. The accuracy increases steadily when increasing the trajectory

length. The approximated spectrum is significantly better by $T_{\text{ver}} = 200$ a.u., as shown in Fig. 11.35. The observed trend of stable improvement in the

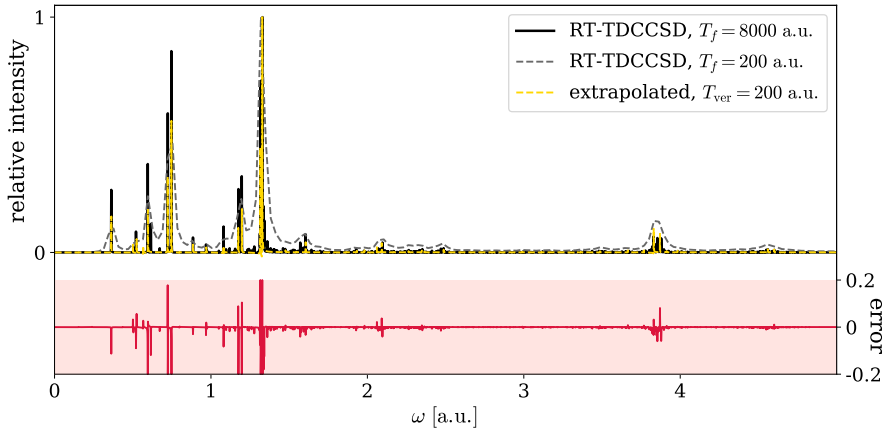

Figure 11.35: Evaluation of the extrapolation of $\mu^z(t)$ of H_2O from 200 a.u. to 8000 a.u. using LASSO. The spectrum of the extrapolation $\tilde{I}_z(\omega)$ is shown in yellow, the spectrum of the short trajectory is gray and long trajectory spectrum $I_z(\omega)$ is shown in black. The red area shows the error $\tilde{I}_z(\omega) - I_z(\omega)$.

extrapolation spectra when increasing the trajectory length up to $T_{\text{ver}} = 500$ a.u. is not visible in the error measure in Table 11.10.

In general, the LASSO method provides a small improvement to OLS when fitting the dipole moment. The extrapolation error is consistently somewhat lower, and the method is slightly less prone to over-fitting. The computational cost of the iterative LASSO method is higher than the OLS method, which has a closed form solution. The computational cost of the LASSO method is still negligible compared to the actual RT-TDCCSD calculations.

Restricting the sign of the linear coefficients to follow the form in Eq. (4.25) obtained by linear response theory seems to be a correct assumption, based on the few systems used in this study. The restriction proved useful, as it prevents the unphysical oscillations of narrowly spaced redundant roots seen in some of the OLS spectra.

11.3 Comparison with Fourier-Padé Spectra

A Fourier-Padé approximant is created when fitting the dipole moment, $\mu^z(t)$. This section will compare the spectra obtained by extrapolating the dipole moment, as presented in Sections 11.1 and 11.2, with the spectra one may obtain by simply using the Fourier-Padé approximant created when estimating the frequencies. The Fourier-Padé approximant used in the frequency estimation is the same regardless of the choice of method of linear regression for optimizing the linear coefficients in $\tilde{\mu}^z(t)$. The Fourier-Padé approximant offers no quantitative measure of error, and the comparison between the fitting model and the Fourier-Padé relies on the qualitative evaluation of the absorption spectra.

Each figure in this section correspond to extrapolation spectra shown for both the OLS and LASSO method in Sections 11.1 and 11.2, respectively. The Fourier-Padé approximant in each figure is evaluated on the same discrete frequency grid as the high resolution absorption spectrum obtained by the long RT-TDCCSD simulation. The Fourier-Padé spectra use the same lifetime parameter as their corresponding high resolution spectra.

11.3.1 The Helium Atom

Starting with the helium atom using the aug-cc-pVTZ basis set. The Fourier-Padé spectrum coincides well with the high resolution spectrum when using $T_{\text{ver}} = 20$ a.u. and $\Delta t = 0.01$ a.u., as seen in Fig. 11.36. The relative intensities

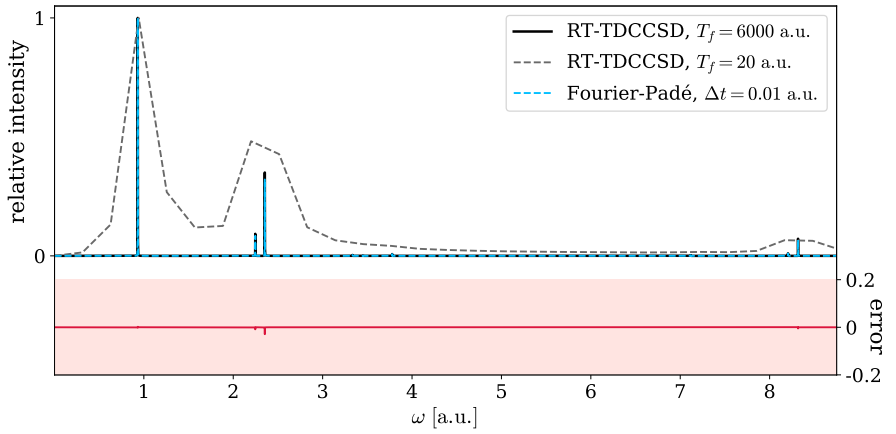

Figure 11.36: Evaluation of the Fourier-Padé approximant created from a 20 a.u. dipole trajectory of He. The high resolution spectrum $I_z(\omega)$ is shown in black, the spectrum of the short trajectory is gray, and the spectrum using the Fourier-Pade $\tilde{I}_z^{M/M}(\omega)$ is blue. The red area shows the error $\tilde{I}_z^{M/M}(\omega) - I_z(\omega)$.

of the peaks of the Fourier-Padé are only slightly wrong. Although the error in the Fourier-Padé spectrum should not be deemed significant, the approximated spectrum was in this case a little improved by using the fitting model. As shown in Figs. 11.1 and 11.25, the spectra using the fitting model were indistinguishable from the true high resolution spectrum independent of the linear regression method.

The Fourier-Padé approximant fails to reproduce the spectrum when using $T_{\text{ver}} = 10$ a.u. and $\Delta t = 0.01$ a.u., as seen in Fig. 11.37. In this case, only the most prominent peak is present in the spectrum. The extrapolation of the approximated function $\tilde{\mu}^z(t)$ is an improvement compared to the Fourier-Padé in this case. Both the spectra using approximations to the dipole moment shown in Figs. 11.3 and 11.26 contain all the peaks. The intensities are not completely correct, and all but the most prominent peak are slightly shifted. The fitting model, independent of method of linear regression, outperforms the Fourier-Padé in this case.

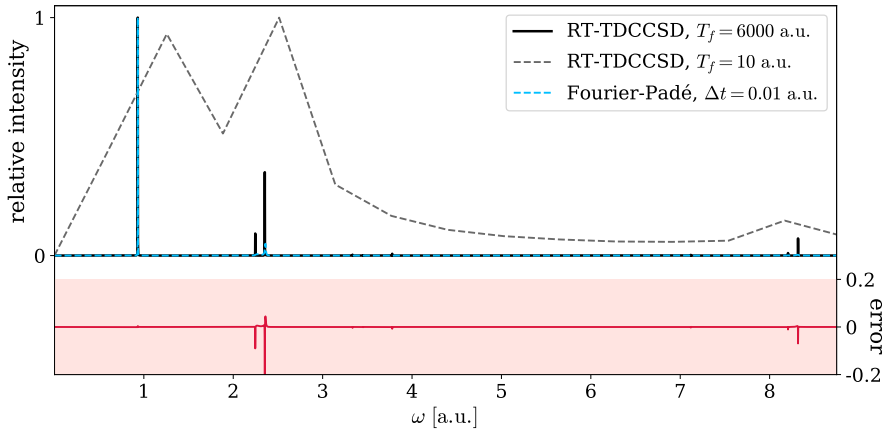

Figure 11.37: Evaluation of the Fourier-Padé approximant created from a 10 a.u. dipole trajectory of He. The high resolution spectrum $I_z(\omega)$ is shown in black, the spectrum of the short trajectory is gray, and the spectrum using the Fourier-Pade $\tilde{I}_z^{M/M}(\omega)$ is blue. The red area shows the error $\tilde{I}_z^{M/M}(\omega) - I_z(\omega)$.

11.3.2 The Hydrogen Molecule

Moving on to the hydrogen molecule, calculated using the aug-cc-pVTZ basis set. The spectrum of the Fourier-Padé using $T_{\text{ver}} = 100$ a.u. and $\Delta t = 0.02$ a.u. is shown in Fig. 11.38. The Padé spectrum is very close to the true high

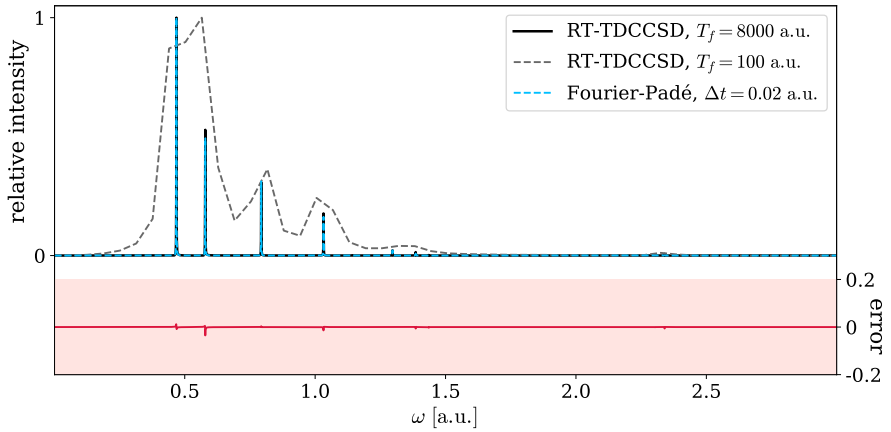

Figure 11.38: Evaluation of the Fourier-Padé approximant created from a 100 a.u. dipole trajectory of H_2. The high resolution spectrum $I_z(\omega)$ is shown in black, the spectrum of the short trajectory is gray, and the spectrum using the Fourier-Pade $\tilde{I}_z^{M/M}(\omega)$ is blue. The red area shows the error $\tilde{I}_z^{M/M}(\omega) - I_z(\omega)$.

resolution spectrum, but several minor errors in the intensities can be seen in

the error area under the spectra. In this case, the fitting model created spectra nearly indistinguishable from the true spectrum. This can be seen in Figs. 11.5 and 11.27, using OLS and LASSO respectively to optimize the linear coefficients. The fitting gave in this case a slightly better result than the Fourier-Padé.

When using a shorter trajectory, $T_{\text{ver}} = 20$ a.u. and $\Delta t = 0.01$ a.u., the Padé spectrum, as seen in Fig. 11.39, fails to reproduce the absorption spectrum. The spectra obtained by using the fitting model were also poor approximations, as seen in Figs. 11.9 and 11.28.

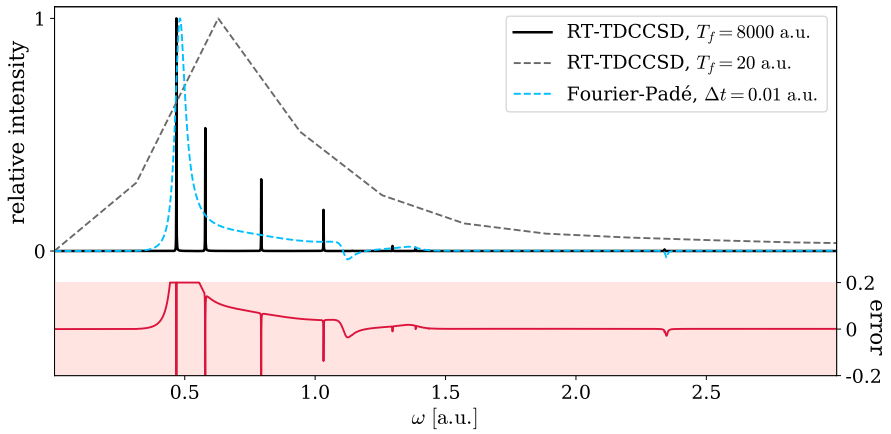

Figure 11.39: Evaluation of the Fourier-Padé approximant created from a 20 a.u. dipole trajectory of H_2. The high resolution spectrum $I_z(\omega)$ is shown in black, the spectrum of the short trajectory is gray, and the spectrum using the Fourier-Pade $\tilde{I}_z^{M/M}(\omega)$ is blue. The red area shows the error $\tilde{I}_z^{M/M}(\omega) - I_z(\omega)$.

11.3.3 The Beryllium Atom

When using the $T_{\text{ver}} = 150$ a.u. and $\Delta t = 0.02$ a.u. dipole trajectory of the beryllium atom using the aug-cc-pVTZ basis set, both the Fourier-Padé and the fitting model yield spectra which are almost indistinguishable from the true high resolution spectrum. This can be seen in Figs. 11.11, 11.29 and 11.40. Only minor inaccuracies may be spotted in the error area under the spectra in all three cases.

Both the Fourier-Padé and the extrapolated dipole moment using OLS fail to reproduce the absorption spectrum when using $T_{\text{ver}} = 50$ a.u. and $\Delta t = 0.01$ a.u.. The Padé spectrum in Fig. 11.41 is missing several peaks, and the peak at $\omega \approx 5.1$ a.u. is flipped. The spectrum of the approximated function, as also seen in Fig. 11.13, replicates the existing peaks in the true spectrum better than the Padé spectrum. On the other hand, the spectrum of the extrapolated dipole moment $\tilde{\mu}^z$ using OLS contains several additional peaks, closely placed with alternating sign. Neither of the approximated spectra are satisfactory. The extrapolation using LASSO provides the best spectrum in this case, as seen in Fig. 11.30. This extrapolation results in the same spectrum as the OLS extrapolation, but without the nonphysical oscillations.

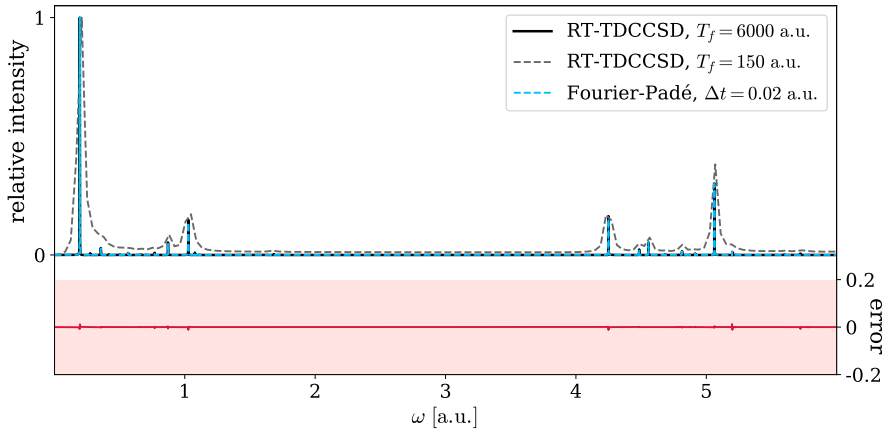

Figure 11.40: Evaluation of the Fourier-Padé approximant created from a 150 a.u. dipole trajectory of Be. The high resolution spectrum $I_z(\omega)$ is shown in black, the spectrum of the short trajectory is gray, and the spectrum using the Fourier-Pade $\tilde{I}_z^{M/M}(\omega)$ is blue. The red area shows the error $\tilde{I}_z^{M/M}(\omega) - I_z(\omega)$.

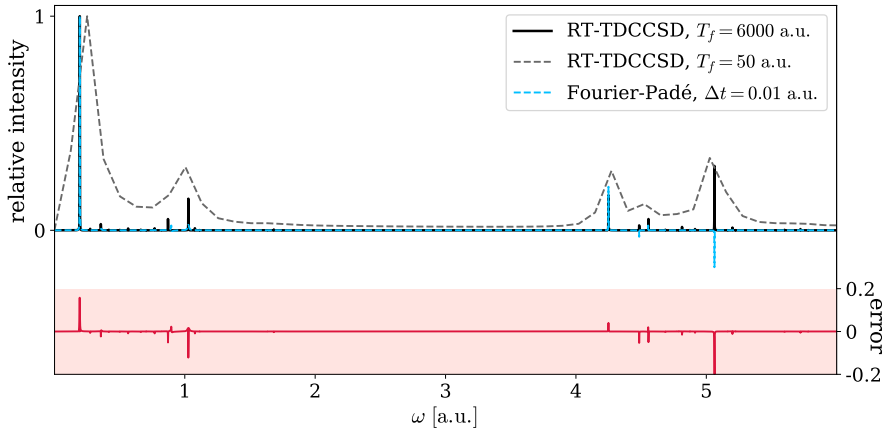

Figure 11.41: Evaluation of the Fourier-Padé approximant created from a 50 a.u. dipole trajectory of Be. The high resolution spectrum $I_z(\omega)$ is shown in black, the spectrum of the short trajectory is gray, and the spectrum using the Fourier-Pade $\tilde{I}_z^{M/M}(\omega)$ is blue. The red area shows the error $\tilde{I}_z^{M/M}(\omega) - I_z(\omega)$.

11.3.4 Lithium Hydride

The dipole moment of lithium hydride was calculated using the aug-cc-pVDZ basis set. The Padé spectrum using $T_{\text{ver}} = 1250$ a.u. and $\Delta t = 0.17$ a.u. is shown in Fig. 11.42. While the spectra from the extrapolations in Figs. 11.16 and 11.31 are both a perfect fit, the Padé spectrum shows small errors in the

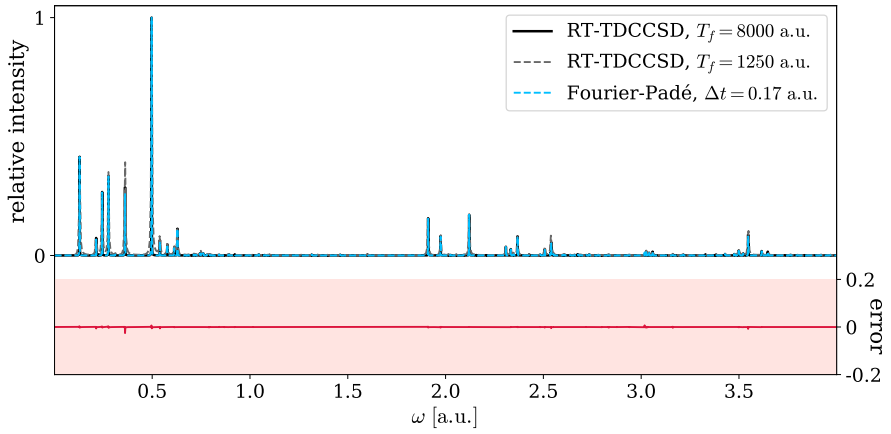

Figure 11.42: Evaluation of the Fourier-Padé approximant created from a 1250 a.u. dipole trajectory of LiH. The high resolution spectrum $I_z(\omega)$ is shown in black, the spectrum of the short trajectory is gray, and the spectrum using the Fourier-Pade $\tilde{I}_z^{M/M}(\omega)$ is blue. The red area shows the error $\tilde{I}_z^{M/M}(\omega) - I_z(\omega)$.

peak intensities. This size in error is insignificant, and the Fourier-Padé has the advantage of being less computationally demanding.

When reducing the dipole trajectory to $T_{\text{ver}} = 400$ a.u. using $\Delta t = 0.06$ a.u., the Padé spectrum still provides an adequate approximation to the true high resolution spectrum, as seen in Fig. 11.43. As seen in Figs. 11.18 and 11.32, the

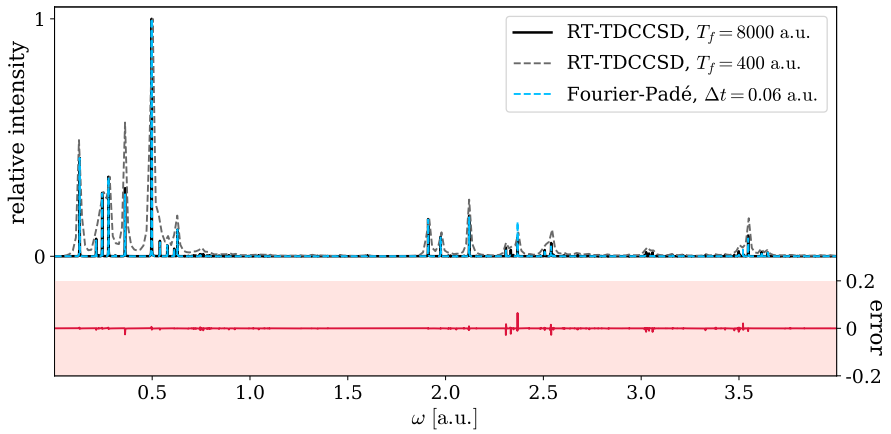

Figure 11.43: Evaluation of the Fourier-Padé approximant created from a 400 a.u. dipole trajectory of LiH. The high resolution spectrum $I_z(\omega)$ is shown in black, the spectrum of the short trajectory is gray, and the spectrum using the Fourier-Pade $\tilde{I}_z^{M/M}(\omega)$ is blue. The red area shows the error $\tilde{I}_z^{M/M}(\omega) - I_z(\omega)$.

error is generally similar for the Padé spectrum and the extrapolation spectra. The exception is the large error at $\omega \approx 3.1$ a.u. in the extrapolated spectrum of OLS. In this case, the Padé approximant provides a more correct spectrum than the OLS extrapolation, while the Fourier-Padé and the LASSO extrapolation give even results.

11.3.5 The Water Molecule

Lastly, looking at the water molecule using the aug-cc-pVDZ basis set, the differences are small between the Padé spectrum using $T_{\text{ver}} = 1250$ a.u. and $\Delta t = 0.17$ a.u. in Fig. 11.44 and the corresponding extrapolation spectra in Figs. 11.20 and 11.33. They all have small but visible inaccuracies, and all three

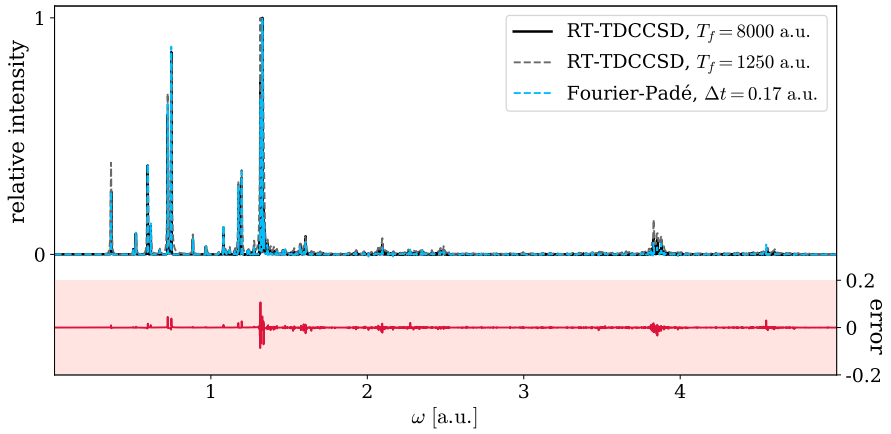

Figure 11.44: Evaluation of the Fourier-Padé approximant created from a 1250 a.u. dipole trajectory of H_2O. The high resolution spectrum $I_z(\omega)$ is shown in black, the spectrum of the short trajectory is gray, and the spectrum using the Fourier-Pade $\tilde{I}_z^{M/M}(\omega)$ is blue. The red area shows the error $\tilde{I}_z^{M/M}(\omega) - I_z(\omega)$.

provide decent approximations to the real-time absorption spectrum.

The H_2O Fourier-Padé spectrum using $T_{\text{ver}} = 500$ a.u. and $\Delta t = 0.07$ a.u. is shown in Fig. 11.45. Much like the extrapolation spectra in Figs. 11.22 and 11.34, the spectrum at $\omega < 1.1$ a.u. seems to be correct, only scaled wrong because the most intense peak at $\omega \approx 1.4$ a.u. is incorrect. The peak at $\omega \approx 1.4$ a.u. Padé spectrum seems to have the wrong sign. The extrapolation using LASSO for the linear optimization gave the best result in this case.

As a general observation, the Fourier-Padé approximant seems to provide a very good approximation to the true high resolution spectrum in the cases where the fitting model gave nearly perfect approximations. The extrapolation spectra using LASSO are consistently equally good or better approximations to the absorption spectrum in all the cases presented in this comparison study. The extrapolation spectra using OLS mostly compare favorably to the Fourier-Padé spectra in this study, with the exception of the cases where the OLS spectra contain nonphysical oscillations.

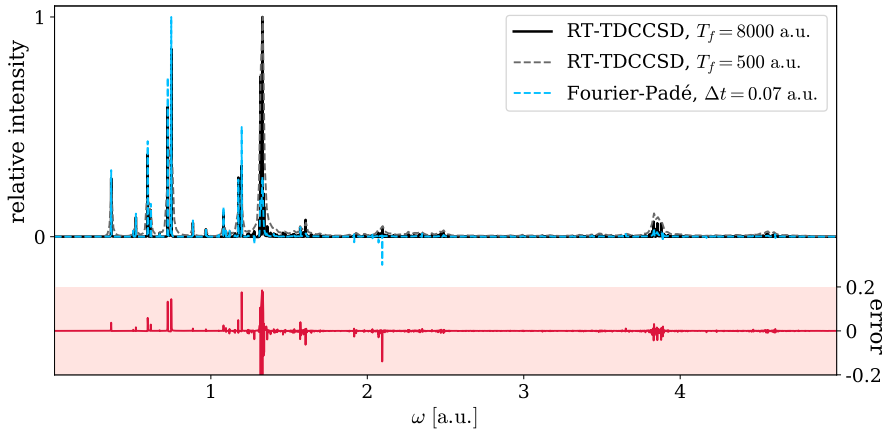

Figure 11.45: Evaluation of the Fourier-Padé approximant created from a 500 a.u. dipole trajectory of H_2O. The high resolution spectrum $I_z(\omega)$ is shown in black, the spectrum of the short trajectory is gray, and the spectrum using the Fourier-Pade $\tilde{I}_z^{M/M}(\omega)$ is blue. The red area shows the error $\tilde{I}_z^{M/M}(\omega) - I_z(\omega)$.

CHAPTER 12

Molecular Orbital Decomposition

This chapter contains a study of the MO decomposition of the dipole moment in RT-TDCCSD theory. The first section shows a study of similarity between the components $\mu^z_{pq}(t)$, made in order to investigate alternative decomposition criteria. The significance of the occupied to virtual transitions is also studied. Lastly, the MO decomposition will be used in the fitting model, using LiH as example system.

12.1 Degeneracy and Similarity in the Molecular Orbitals

This section shows a study of the correlation between components in the electric dipole moment, using the algorithm described in Section 9.2.

The MO components of the dipole moment can be thought of as elements of an upper triangular matrix, as is used to visualize the similarity clustering of the dipole moment components in Figs. 12.1, 12.3, 12.5, 12.7 and 12.9. Each square in the figures represents one matrix element, where the lower (inconsequential) triangle is colored gray. The elements of the upper triangle are color coded following three rules:

- **white square**: Forbidden transition, $|P^z_{pq}| < 10^{-10}$. The component was not stored, as it should be zero.
- **black square**: Dissimilar component μ^z_{pq}. The component is not sufficiently correlated, i.e. $r_{pq,rs} < (1 - \epsilon)$ for all other μ^z_{rs}.
- **colored square**: The color itself is unimportant, but all components sharing color are similar. If μ^z_{pq} is a given color, then it is similar to at least one other component μ^z_{rs} with the same color, i.e. $r_{pq,rs} \geq (1 - \epsilon)$.

Each dipole clustering figure contains the clustering using $\epsilon = 10^{-10}$ to the left and $\epsilon = 10^{-1}$ to the right. The left clustering contains groups with components that are similar to almost numerical precision. The gray lines separates the degenerate from the non-degenerate orbitals. The MO energies are found in Table A.1.

The clustering of the MO decomposition of the helium atom is shown in Fig. 12.1. There are two things to note. Firstly, there is a large number of white squares corresponding to forbidden transitions. This is the case for all the studied systems, which greatly reduces the memory load of the MO decomposition. Secondly, by looking at the left plot showing the groups formed

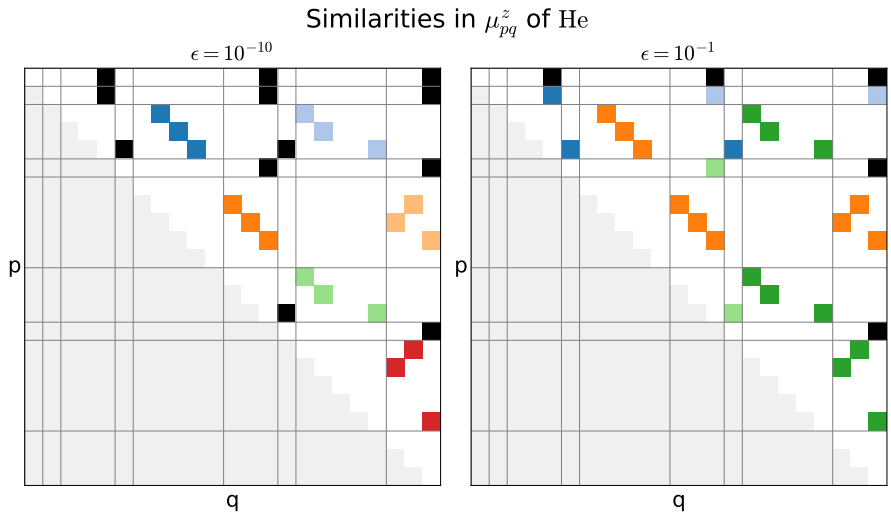

Figure 12.1: Groups of dipole moment components of He formed by similarity. Each square in the upper triangle corresponds to a component μ^z_{pq}, and is color coded according to the explanation in the beginning of this section.

with the strict criterion for similarity ($\epsilon = 10^{-10}$), one can observe all groups are formed by degenerate orbital combinations. Atoms belong to the *kugel* symmetry group K_h and the orbitals are therefore expected to exhibit symmetry. Both the helium atom and the beryllium atom have high levels of degeneracy among their orbitals. The symmetry was not imposed on the calculations of the RHF reference states for any of the systems, but well converged calculations are expected to have correct spatial symmetry. An example of degenerate orbital combinations could be the dark blue group in the left plot in Fig. 12.1, consisting

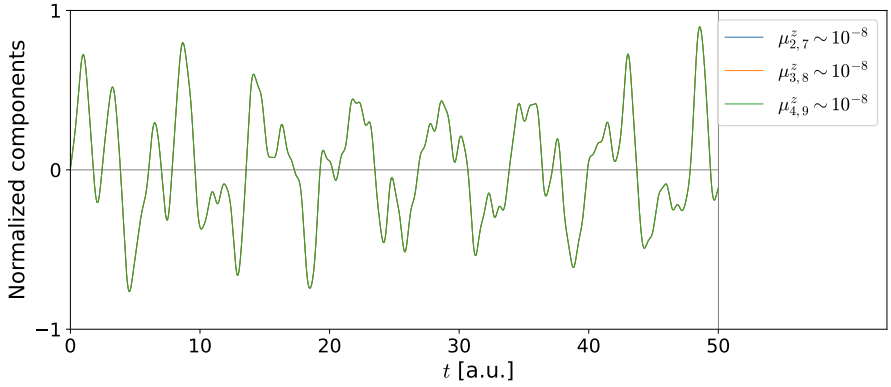

Figure 12.2: Dipole components of degenerate MOs of helium. The three components correspond to the dark blue group on the left plot in Fig. 12.1.

of $\mu^z_{2,7}$, $\mu^z_{3,8}$ and $\mu^z_{4,9}$. As can be seen in Table A.1, the orbitals ψ_2, ψ_3 and ψ_4, and ψ_7, ψ_8 and ψ_9 are degenerate. The three dipole moment components are indistinguishable, as seen in Fig. 12.2.

There is an exception to the rule of identical dipole components for the degenerate orbital combinations, only seen in the dipole moment of the hydrogen molecule. In the left plot in Fig. 12.3, there are two places where there are four degenerate combinations of MOs, but only two of them form a group. One

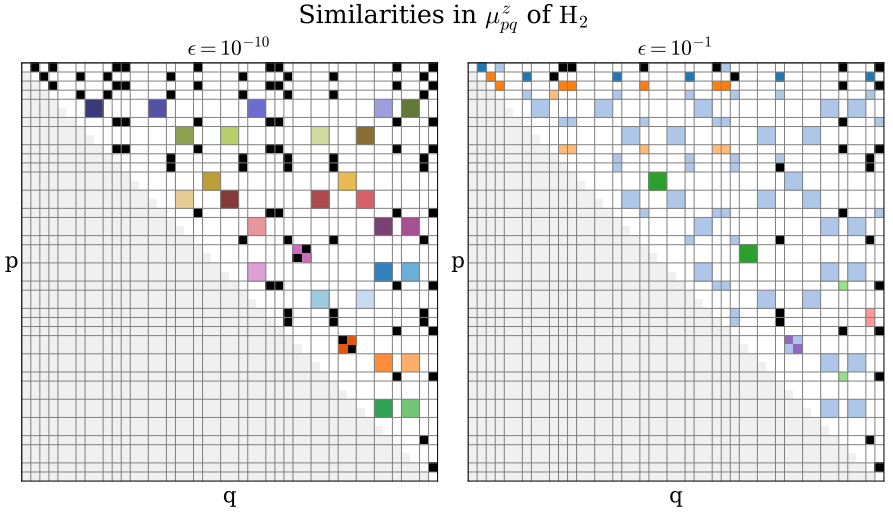

Figure 12.3: Groups of dipole moment components of H_2 formed by similarity. Each square in the upper triangle corresponds to a component μ^z_{pq}, and is color coded according to the explanation in the beginning of this section.

example is the four components $\mu^z_{20,30}$, $\mu^z_{20,31}$, $\mu^z_{21,30}$ and $\mu^z_{21,31}$. In this case, the orbitals ψ_{20} and ψ_{21} are degenerate, and ψ_{30} and ψ_{31} are degenerate. In the left plot in Fig. 12.3, $\mu^z_{20,30}$, $\mu^z_{21,31}$ are light purple, while $\mu^z_{20,31}$, $\mu^z_{21,30}$ are black. The explanation may be found in numerical instability. As may be seen in Fig. 12.4, the components are actually very similar, but have vastly different scaling. While $\mu^z_{20,30}$ and $\mu^z_{21,31}$ are of size $\sim 10^{-10}$, the two other components $\mu^z_{20,31}$ and $\mu^z_{21,30}$ are $\sim 10^{-18}$. In the other example, the black squares $\mu^z_{30,35}$ and $\mu^z_{31,36}$ are of size $\sim 10^{-19}$. These components are all *numerically zero*, and can be speculated to correspond to forbidden transitions. Calculations with numbers this small are numerically unstable. Two-fold degeneracy among the orbitals is expected, as the point group $D_{\infty h}$ of H_2 consists of both one and two-dimensional irreducible representations. The dipole components of degenerate orbital combinations for all the systems shown in Figs. 12.1, 12.3, 12.5, 12.7 and 12.9 clearly contain the same frequencies and the same relative intensities. Treating them separately in a dipole fitting would therefore be repeating the same work multiple times. In a MO decomposition, degenerate orbital combinations should therefore be treated as one.

The number of groups is reduced when using the more relaxed similarity criterion ($\epsilon = 10^{-1}$) for all the systems in Figs. 12.1, 12.3, 12.5, 12.7 and 12.9.

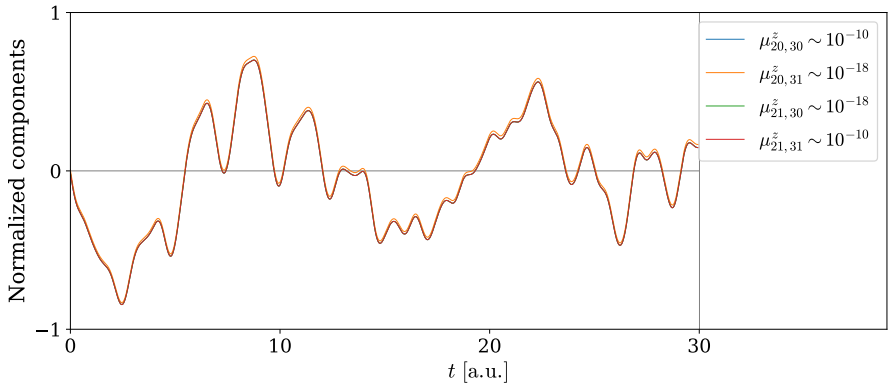

Figure 12.4: Dipole components of degenerate MOs of H_2 . These components are one of two degenerate sets of MOs which did not form a group in the left plot in Fig. 12.3.

There is no obvious pattern in the grouping using the relaxed similarity criterion. However, as seen for the similarity clustering of the beryllium atom in Fig. 12.5, the groups often contain components sharing an orbital. For example, the

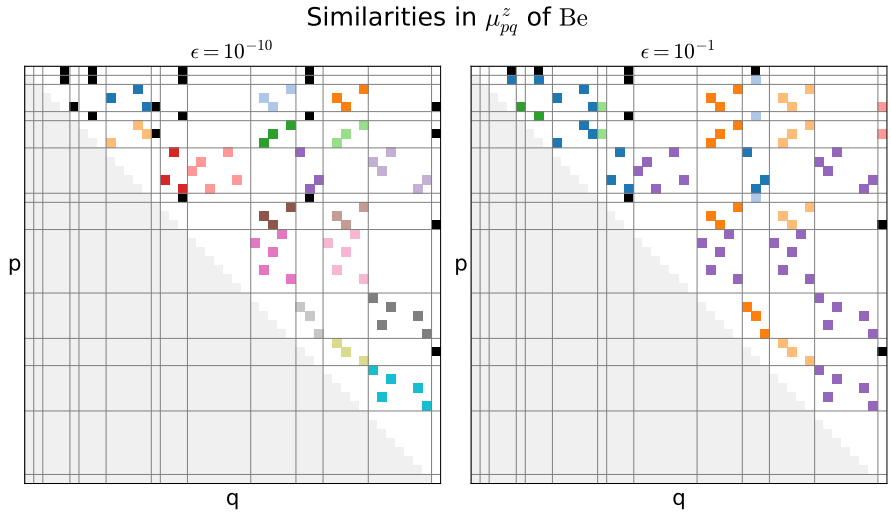

Figure 12.5: Groups of dipole moment components of Be formed by similarity. Each square in the upper triangle corresponds to a component μ^z_{pq}, and is color coded according to the explanation in the beginning of this section.

light blue group in the right plot in Fig. 12.5 contains the components $\mu^z_{1,31}$, $\mu^z_{5,31}$ and $\mu^z_{14,31}$. Although the same color is often repeated in a column or row, there seems to be no clear pattern that can be used to foresee which MO

components will be similar. The relaxed similarity criterion ($\epsilon = 10^{-1}$) still yields groups with visibly similar components, as illustrated in Fig. 12.6. The

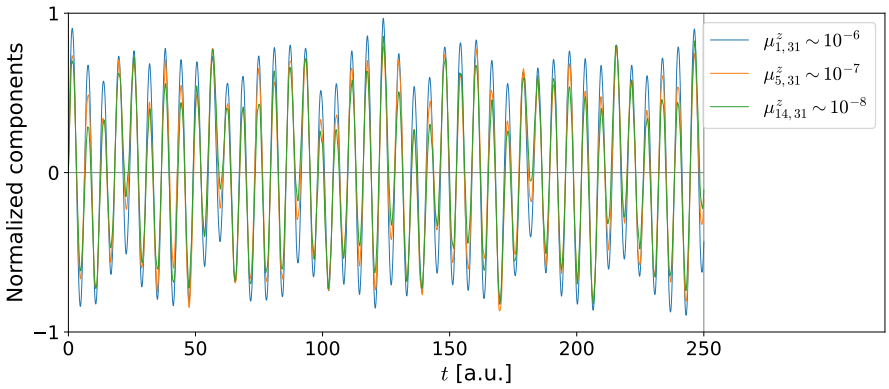

Figure 12.6: Three similar dipole components of the beryllium atom. The three components correspond to the light blue group in the right plot in Fig. 12.5.

three components $\mu^z_{1,31}$, $\mu^z_{5,31}$ and $\mu^z_{14,31}$, shown in light blue in the right plot in Fig. 12.5, are dominated by the same frequency. The similarity measure does not mind the difference in magnitude.

The clustering of components of $\mu^z(t)$ of LiH is shown in Fig. 12.7. The

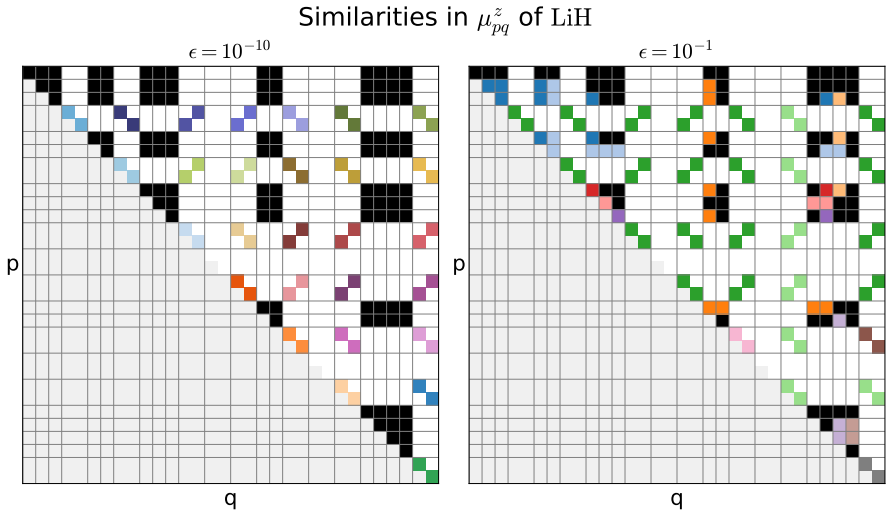

Figure 12.7: Groups of dipole moment components of LiH formed by similarity. Each square in the upper triangle corresponds to a component μ^z_{pq}, and is color coded according to the explanation in the beginning of this section.

molecular orbitals are either non-degenerate or degenerate to the second degree.

This is expected, as the point group $C_{\infty v}$ of LiH consists of one and two-dimensional irreducible representations. When using the relaxed similarity criterion ($\epsilon = 10^{-1}$), a large number of components form a group, assigned with the color dark green. The components $\mu^z_{pq}(t)$ in large dark green group in the right plot in Fig. 12.7 are shown in Fig. 12.8. The group contains 36 different components, but the group is still clearly dominated by the same frequency. An important thing to note, is that the components are both parallel

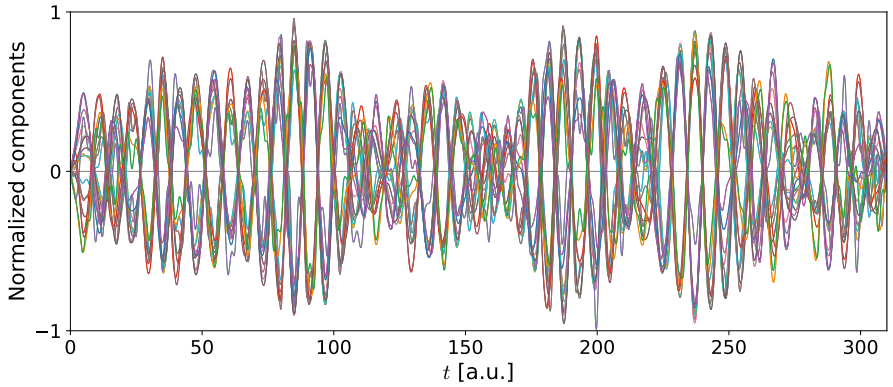

Figure 12.8: The 36 similar dipole components of the lithium hydride, corresponding to the dark green group in the right plot in Fig. 12.7.

and anti-parallel with respect to the dominant frequency. The components in Fig. 12.8 are normalized, so the figure does not show the correct magnitude, but the anti-parallel components will still cancel each other out to some degree.

The similarity clusters of the dipole components of the water molecule are shown in Fig. 12.9. Unlike the other systems, the water molecule has no degenerate orbitals. The molecule belongs to the C_{2v} point group, which only contains one-dimensional irreducible representations. The similarity clustering with the relaxed criterion $\epsilon = 10^{-1}$ also shows little similarity between the components compared to the other systems.

From the limited examples shown in this section, only degeneracy in the molecular orbitals offers guaranteed strong similarity between the MO components of the dipole moment. There is no conclusive result on how best to determine a reduced orbital space among non-degenerate orbitals when storing the decomposed dipole moment. Creating groups based on similarity clustering of the dipole moment can alleviate the computational cost of the post-processing, such as the dipole moment fitting or when simply using a Fourier-Padé approximant, but will not reduce the memory load of the real-time simulations.

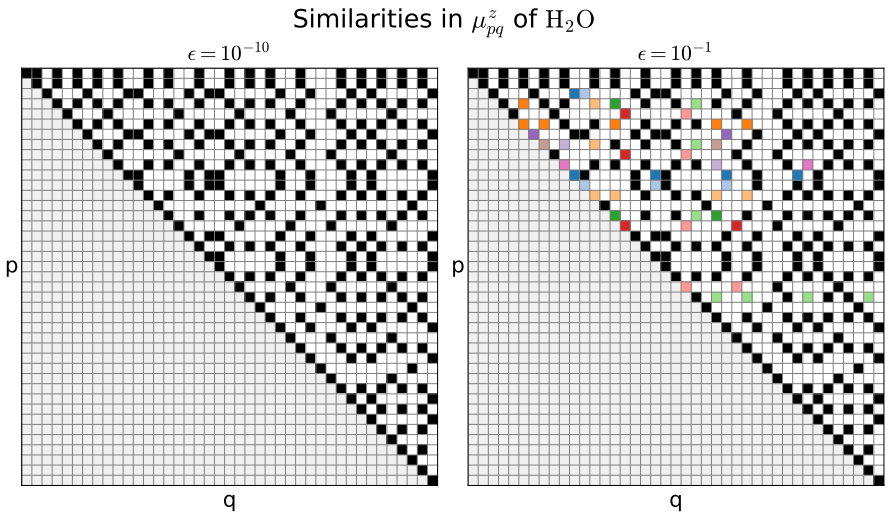

Figure 12.9: Groups of dipole moment components of H_2O formed by similarity. Each square in the upper triangle corresponds to a component μ^z_{pq}, and is color coded according to the explanation in the beginning of this section.

12.2 Transitions from Occupied to Virtual Orbitals

The MO decomposition of the dipole moment in RT-TDDFT often only includes the transitions from occupied to virtual orbitals.[13] This section investigates whether or not only including the occupied-virtual transitions makes a reasonable approximation in CCSD-theory.

The plots in Figs. 12.10, 12.12, 12.14, 12.16 and 12.18 all compare the spectra $S_z(\omega)$ from the full z-component $\mu^z(t)$ to the spectra obtained by only including the occupied to virtual transitions:

$$\mu^z(t) \approx \sum_{ia} \mu_{ia}(t), \tag{12.1}$$

where i denotes occupied orbitals and a denotes virtual orbitals. The Fourier transform of the dipole moment will use the lifetime parameter $\gamma = \frac{\pi}{N_t \Delta t}$, where $\Delta t = 0.01$ a.u..

The occupied-virtual transitions make up for almost all the peaks in the absorption spectrum of the helium atom using the aug-cc-pVTZ basis, as seen in Fig. 12.10. Only a small part of the two most prominent peaks are missing in the occupied-virtual spectrum. The helium atom only has three non-zero dipole components μ^z_{ia}. The spectrum of each component is shown on a short interval in Fig. 12.11. The component $\mu^z_{0,4}$ is almost the sole contributor to the largest peak around $\omega \approx 0.9$ a.u.. Both peaks around $\omega \approx 2.3$ a.u. have the same component $\mu^z_{0,18}$ as their most significant contributor. The spectrum shows a small negative peak at $\omega \approx 2.4$ a.u.. Although the full spectrum should only contain positive peaks, the separate components may have negative contributions. This is also the case for the RT-TDDFT decomposition.[12]

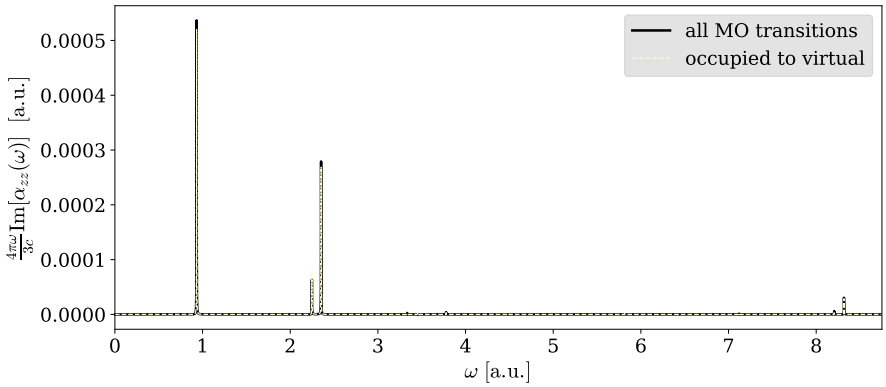

Figure 12.10: Evaluating the absorption spectrum $S_z(\omega)$ of He when only including occupied-virtual MO transitions. The FFT used $t_n \in [t_0, 3000 \text{ a.u.})$.

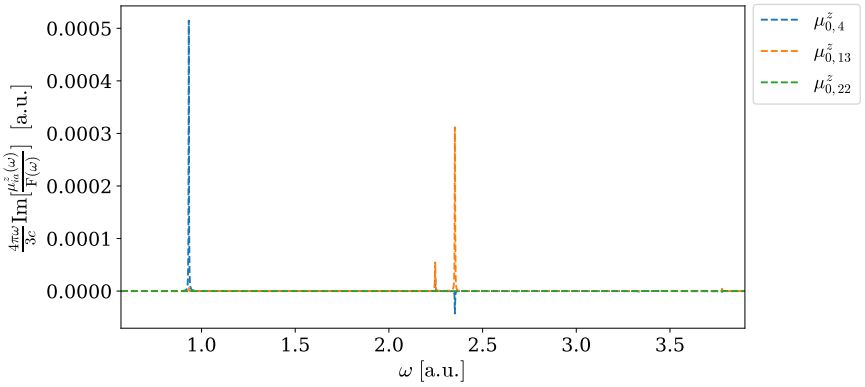

Figure 12.11: Absorption spectra of the individual components μ^z_{ia} of He.

The occupied-virtual spectrum of the hydrogen molecule using the aug-cc-pVTZ basis set shown in Fig. 12.12 is also very similar to the spectrum of the full z-component. Some of the intensities in the occupied-virtual spectrum are slightly lower, and a small peak at $\omega \approx 1.4$ a.u. is missing. There are nine μ^z_{ia} components for the hydrogen molecule. These are shown on a short interval in Fig. 12.13. One could hope that the MO decomposition of the dipole moment could enable assignment of the peaks in the absorption spectrum to specific molecular orbital transitions. There seems to be no clear way to assign the peaks, as both μ^z_{01} and μ^z_{03} give significant contributions to the largest peak, at $\omega \approx 0.47$ a.u.. The same orbital transition μ^z_{01} is also the largest contributor to both visible peaks in Fig. 12.13.

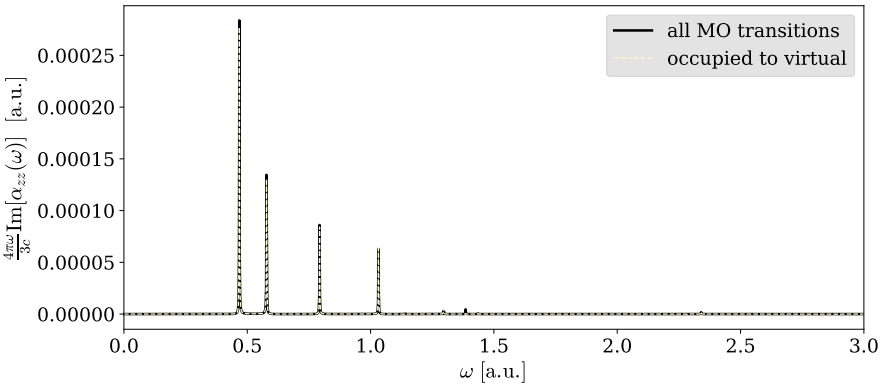

Figure 12.12: Evaluating the absorption spectrum $S_z(\omega)$ of H_2 when only including occupied-virtual MO transitions. The FFT used $t_n \in [t_0, 4000 \text{ a.u.})$.

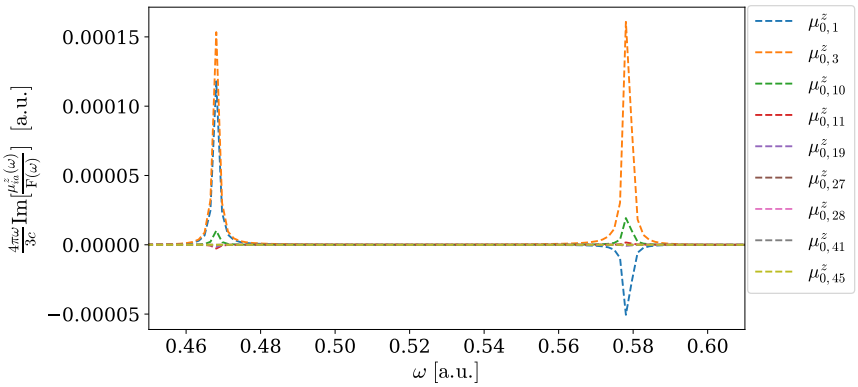

Figure 12.13: Absorption spectra of the individual components μ^z_{ia} of H_2.

The spectrum only containing the dipole components μ^z_{ia} of the beryllium atom using the aug-cc-pVTZ basis set is shown in Fig. 12.14. The occupied-virtual spectrum is missing a small peak at $\omega \approx 0.9$ a.u., but otherwise the intensities are only marginally smaller than those of the full spectrum, $S_z(\omega)$. The beryllium atom with the aug-cc-pVTZ basis set has eight non-zero occupied-virtual dipole components, which are shown on a short interval of high energy transitions in Fig. 12.15. The high energy transitions $\omega > 4$ a.u. correspond to core excitations, $\psi_0 \to \psi_a$. While the peak at $\omega \approx 5.1$ a.u. has $\mu^z_{0,31}$ as a clear dominant contributor, the peak at $\omega \approx 4.2$ a.u. has several contributors which add up to a significant peak in the spectrum.

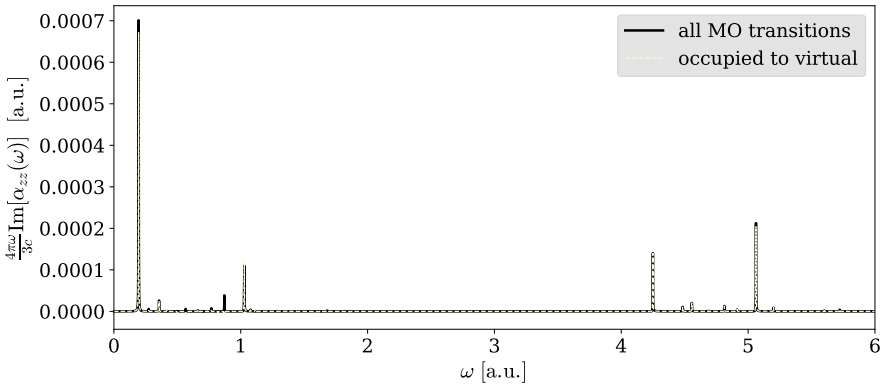

Figure 12.14: Evaluating the absorption spectrum $S_z(\omega)$ of Be when only including occupied-virtual MO transitions. The FFT used $t_n \in [t_0, 3000 \text{ a.u.})$.

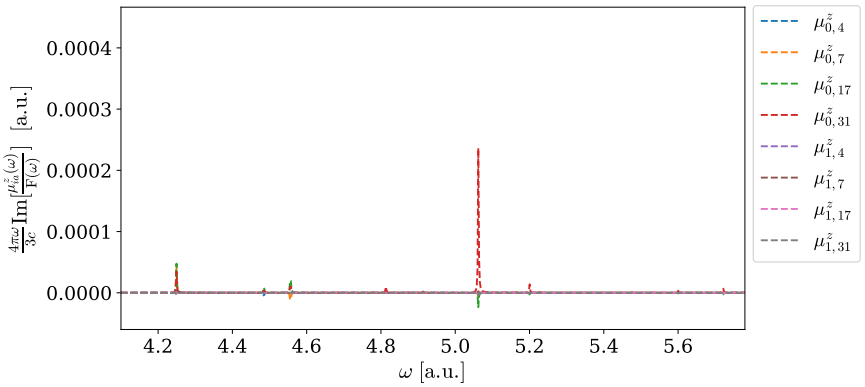

Figure 12.15: Absorption spectra of the individual components μ^z_{ia} of Be.

As seen in Fig. 12.16, the spectrum of lithium hydride using the aug-cc-pVDZ basis set only containing the dipole components corresponding to transitions from occupied to virtual MOs deviates somewhat more from the spectrum using the full dipole $\mu^z(t)$ compared to the previous cases. This is maybe not surprising, as the lowest unoccupied orbital ψ_2 has a negative eigenvalue ($\varepsilon = -0.0080780$ a.u.). There are 24 occupied-virtual dipole components. The occupied to virtual transitions make up for most of the spectrum $\omega < 4$ a.u., but do not include the low intensity peaks around $\omega = 7$ a.u.. These high energy transitions with low intensities are not significant to reproduce the absorption spectrum. The spectra of the μ^z_{ia} components are shown in Fig. 12.17. For the lower energy transitions $\omega < 0.5$ a.u., the most significant components are transitions from the valence orbital ψ_1 to the virtual orbitals.

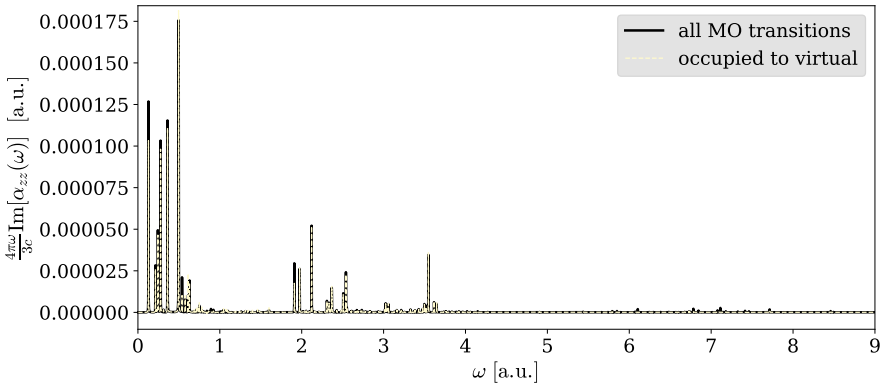

Figure 12.16: Evaluating the absorption spectrum $S_z(\omega)$ of LiH when only including occupied-virtual MO transitions. The FFT used $t_n \in [t_0, 4000 \text{ a.u.})$.

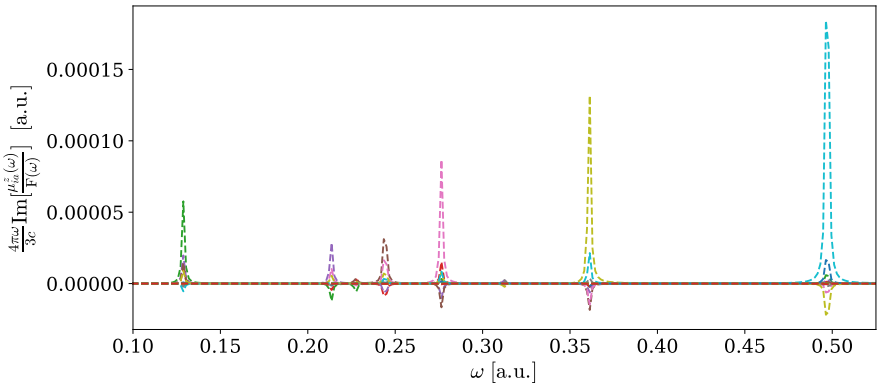

Figure 12.17: Absorption spectra of the individual components μ^z_{ia} of LiH. Showing a total of 24 components. The most visible are $\mu^z_{1,19}$ (light blue), $\mu^z_{1,18}$ (light green), $\mu^z_{1,10}$ (pink) and $\mu^z_{1,2}$ (green).

The occupied-virtual spectrum of the water molecule using the aug-cc-pVDZ basis is shown in Fig. 12.18. The spectrum contains 62 μ^z_{ia} components. The part of the spectrum shown in Fig. 12.19 shows a lot of noise among the components. The two most prominent components in this figure are $\mu^z_{3,37}$ (purple line) and $\mu^z_{4,36}$ (orange line). Although the intensity of this area is low, the spectral density is high. This makes it difficult to estimate the frequencies in this area. The very high energy transitions $\omega \approx 20$ a.u. are shown in Fig. 12.20. All of the visible peaks correspond to transitions from the core orbital ψ_0. These high energy parts of the spectrum are usually not of interest. Limiting the dipole components to only include transitions from valence orbitals to the virtual orbitals with lower orbital energies might simplify the fitting of the dipole moment.

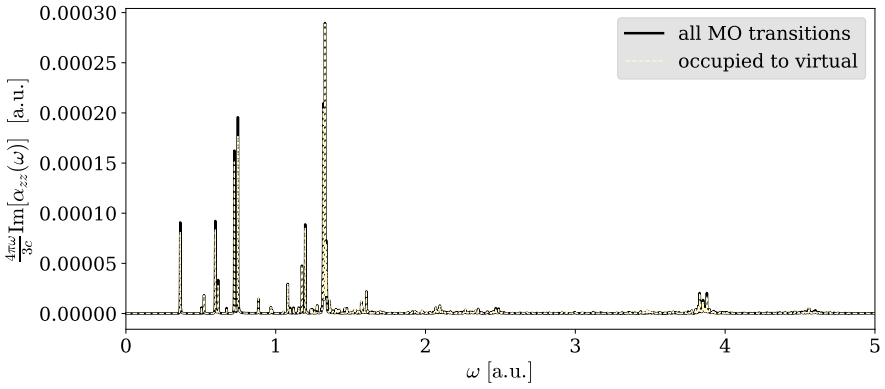

Figure 12.18: Evaluating the absorption spectrum $S_z(\omega)$ of H_2O when only including occupied-virtual MO transitions. The FFT used $t_n \in [t_0, 4000 \text{ a.u.})$.

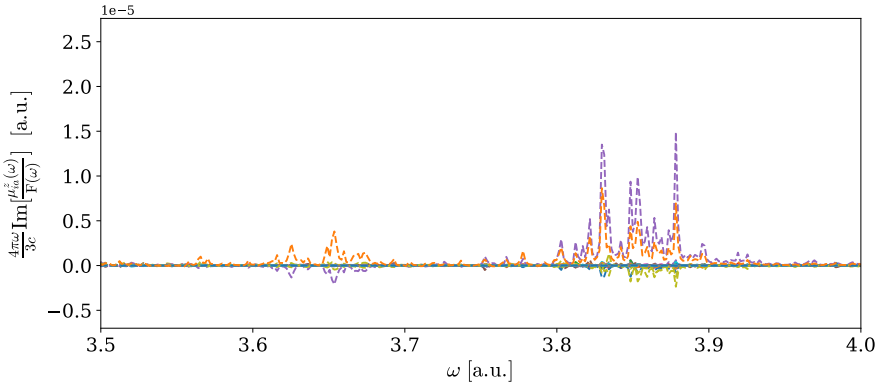

Figure 12.19: Absorption spectra of the individual components μ^z_{ia} of H_2O. The figure contains 62 components, but the two most visible are $\mu^z_{3,37}$ (purple) and $\mu^z_{4,36}$ (orange)

From the small set of systems included in this study, the spectra containing exclusively the transitions from occupied to virtual orbitals are very similar to the full spectrum, $S_z(\omega)$. The intensities in the spectra are either the same or slightly lower when only including the occupied-virtual components, μ^z_{ia}.

The RT-TDCCSD spectra are approximations to the FCI spectra. A more rigorous approach to determine if the occupied-virtual transitions are sufficient for a decent approximation would be to compare them to the FCI spectra and spectra from less computationally heavy methods or smaller basis sets. For the occupied-virtual transition spectrum to be useful, it should provide a significantly better approximation to the FCI spectrum compared to cheaper methods. The field strength must be sufficiently weak for the RHF reference state to maintain a good approximation to the time-dependent CC state throughout the simulation.

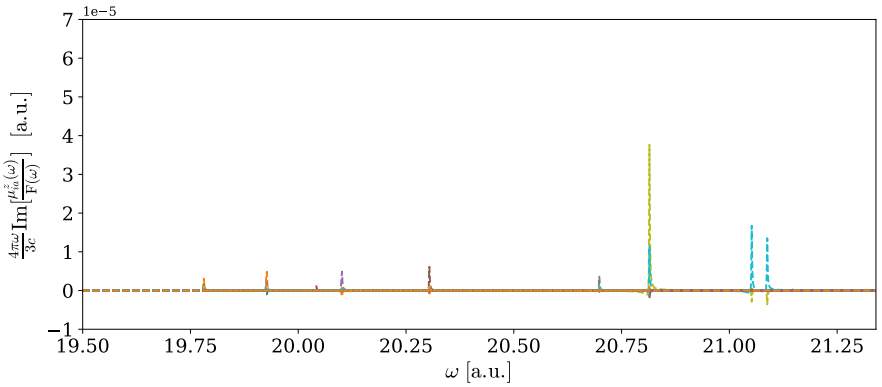

Figure 12.20: Absorption spectra of the individual components μ^z_{ia} of H_2O. The figure contains 62 components, but all the visible components include the core orbital, $\mu^z_{0,a}$. The two most visible are $\mu^z_{0,27}$ (light blue) and $\mu^z_{0,24}$ (light green).

The RT-TDCCSD spectra of He and H_2 are equivalent to the FCI spectra, and in these cases the occupied-virtual transitions yield almost the same spectra.

12.3 Fitting the Decomposed Dipole Moment

The following study explores the fitting of the decomposed dipole moment, using lithium hydride with the aug-cc-pVDZ basis set as example system. The fitted function is given by

$$\tilde{\mu}^z(t) = \sum_{p \leq q} \tilde{\mu}^z_{pq}(t), \tag{12.2}$$

where $\tilde{\mu}^z_{pq}(t)$ is the approximation of $\mu^z_{pq}(t)$. The details of the fitting are otherwise the same as in Section 11.1, using OLS to determine the linear coefficients. The MO components of the dipole moment showed negative interference in the previous section. The sign of the coefficients of the components $\mu^z_{pq}(t)$ will therefore be unknown.

The MO decomposition of the dipole moment $\mu^z(t)$ of LiH was sampled up to $T_{\text{full}} = 4000$ a.u., which will be used to calculate the extrapolation error, E_{full}. The first section will show the fitting using all MO components, while the latter two sections will limit the spectra to only include transitions from occupied to virtual orbitals and valence to virtual orbitals, respectively.

12.3.1 The Full z-Component

The extrapolation error E_{full} in Table 12.1 is given for the approximation of the full dipole moment $\mu^z(t)$, as well as two approximations using MO decomposition. The first decomposition groups degenerate components together and all other components are treated separately. This means that the components sharing

color in the left plot Fig. 12.7 are summed up and approximated by one function, while all components which are colored black are treated separately. The second decomposition uses similarity clustering with $\delta = 10^{-1}$. Similarly to the degeneracy decomposition, the black components shown in the right plot in Fig. 12.7 are then treated separately, while the components sharing color are summed up and approximated by a single function.

Table 12.1: Coefficient of determination when fitting $\mu^z(t)$ of LiH, using MO decomposition.

	$\boldsymbol{E}_{\text{full}}$		
$\boldsymbol{T}_{\text{ver}}$ [a.u.]	**decomposed**	**similarity clusters**	**not decomposed**
10	2	2	3
20	2	2	3
50	2	2	4
75	2	2	2
100	1	$9 \cdot 10^{-1}$	2
150	$7 \cdot 10^{-1}$	$5 \cdot 10^{-1}$	$8 \cdot 10^{-1}$
200	$1 \cdot 10^{-1}$	$1 \cdot 10^{-1}$	$3 \cdot 10^{-1}$
300	$2 \cdot 10^{-2}$	$1 \cdot 10^{-2}$	$4 \cdot 10^{-3}$
400	$2 \cdot 10^{-3}$	$1 \cdot 10^{-3}$	$5 \cdot 10^{-4}$
500	$6 \cdot 10^{-3}$	$7 \cdot 10^{-3}$	$2 \cdot 10^{-4}$
600	$1 \cdot 10^{-3}$	$1 \cdot 10^{-3}$	$2 \cdot 10^{-4}$
750	$8 \cdot 10^{-4}$	$4 \cdot 10^{-4}$	$3 \cdot 10^{-4}$
1000	$4 \cdot 10^{-4}$	$5 \cdot 10^{-4}$	$3 \cdot 10^{-5}$
1250	$7 \cdot 10^{-6}$	$1 \cdot 10^{-5}$	$1 \cdot 10^{-6}$
1500	$8 \cdot 10^{-7}$	$2 \cdot 10^{-6}$	$3 \cdot 10^{-7}$
1750	$2 \cdot 10^{-7}$	$2 \cdot 10^{-7}$	$1 \cdot 10^{-7}$

The extrapolation error E_{full} was calculated using $T_{\text{full}} = 4000$ a.u., even though the full dipole $\mu^z(t)$ was sampled up to $T_{\text{full}} = 8000$ a.u.. This choice was made to simplify comparison with the results in the upcoming sections.

The extrapolation error is not significantly reduced when using the MO decomposition. In most cases, the extrapolation error is lowest without the decomposition. The MO decomposition using degeneracy consists of 133 components, and is therefore 133 times more expensive than simply fitting the entire z-component of the dipole moment, $\mu^z(t)$. Using similarity clustering reduces the number of components to 77, which is still a large increase in computational cost. For the MO decomposition to be useful, there should be a significant improvement to justify the extra computational cost.

The error in the approximated spectrum when using MO decomposition by degeneracy in Fig. 12.21 is very similar to that using MO decomposition based on similarity clustering in Fig. 12.22. There is generally several more small inaccuracies in both of the extrapolated spectra using decomposition compared to the spectrum in Fig. 11.18 not using decomposition. The extrapolation on the full dipole moment $\tilde{\mu}^z(t)$ in Fig. 11.18 has a large error at $\omega \approx 3.1$ a.u. which is not seen in the extrapolation spectra using decomposition. This is however not a general trend, as such phantom oscillations were observed for some of the other trajectory lengths T_{ver} when fitting the decomposed dipole moment. This type of pollution in the extrapolation spectrum may be eliminated by using the

LASSO method and requiring all coefficients to be positive for the full dipole moment $\mu^z(t)$. The individual MO components are not guaranteed to have positive peaks in their absorption spectra, and one can therefore not restrict the coefficients to be positive when fitting the components separately.

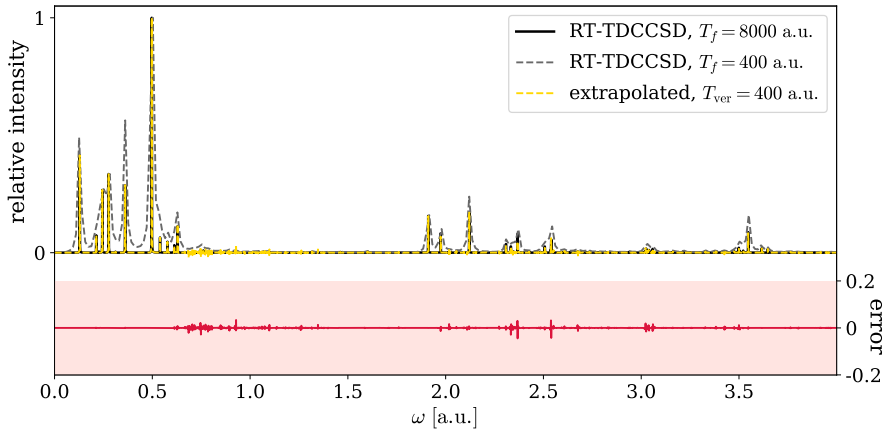

Figure 12.21: Evaluation of the extrapolation of $\mu^z(t)$ of LiH from 400 a.u. to 8000 a.u., using MO decomposition by degeneracy. The spectrum of the extrapolation $\tilde{I}_z(\omega)$ is shown in yellow, the spectrum of the short trajectory is gray and long trajectory spectrum $I_z(\omega)$ is shown in black. The red area shows the error $\tilde{I}_z(\omega) - I_z(\omega)$.

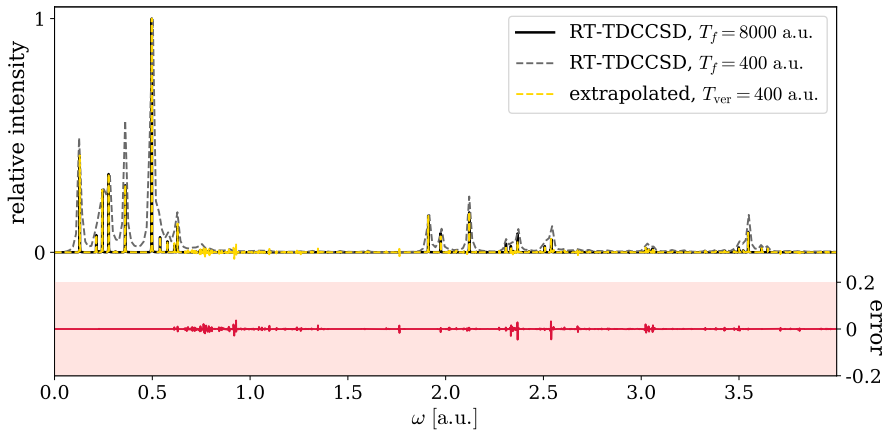

Figure 12.22: Evaluation of the extrapolation of $\mu^z(t)$ of LiH from 400 a.u. to 8000 a.u., using MO decomposition by similarity clustering. The spectrum of the extrapolation $\tilde{I}_z(\omega)$ is shown in yellow, the spectrum of the short trajectory is gray and long trajectory spectrum $I_z(\omega)$ is shown in black. The red area shows the error $\tilde{I}_z(\omega) - I_z(\omega)$.

12.3.2 Occupied to Virtual Transitions

In this section, the dipole moment will be given by

$$\mu^z(t) \approx \sum_{ia} \mu^z_{ia}(t), \tag{12.3}$$

only including the MO components corresponding to transitions from occupied orbitals $\psi_i \in \{\psi_0, \psi_1\}$ to virtual orbitals $\psi_a \in \{\psi_2, \ldots, \psi_{31}\}$. The MO decomposition treats all components $\mu^z_{ia}(t)$ separately. The extrapolation error of the dipole moment only consisting of transitions from occupied to virtual orbitals is given in Table 12.2.

Table 12.2: Coefficient of determination when fitting $\mu^z(t)$ of LiH, using MO decomposition. Only using transitions from occupied to virtual orbitals.

	$\boldsymbol{E}_{\text{full}}$	
$\boldsymbol{T}_{\text{ver}}$ [a.u.]	**decomposed**	**not decomposed**
10	2	4
20	2	6
50	2	2
75	2	2
100	1	1
150	$4 \cdot 10^{-1}$	$4 \cdot 10^{-1}$
200	$7 \cdot 10^{-2}$	$3 \cdot 10^{-1}$
300	$8 \cdot 10^{-3}$	$6 \cdot 10^{-3}$
400	$6 \cdot 10^{-4}$	$6 \cdot 10^{-4}$
500	$6 \cdot 10^{-4}$	$3 \cdot 10^{-4}$
600	$4 \cdot 10^{-4}$	$4 \cdot 10^{-4}$
750	$6 \cdot 10^{-4}$	$3 \cdot 10^{-4}$
1000	$2 \cdot 10^{-4}$	$1 \cdot 10^{-5}$
1250	$7 \cdot 10^{-6}$	$1 \cdot 10^{-6}$
1500	$3 \cdot 10^{-7}$	$8 \cdot 10^{-7}$
1750	$2 \cdot 10^{-7}$	$2 \cdot 10^{-7}$

The fitting of the dipole moment without decomposition has very similar extrapolation error when only using transitions from the occupied to virtual orbitals to when all transitions are included.

Using the MO decomposition in the fitting model seems to have no clear advantage, but the fitting of the decomposed dipole moment using occupied to virtual transitions is improved compared to Table 12.1. The extrapolation error when only including occupied to virtual transitions in Table 12.2 is very similar with and without the decomposition, while the error was slightly larger for the decomposed dipole moment in Table 12.2, including all dipole components.

The error in the extrapolation spectra using $T_{\text{ver}} = 400$ a.u. with and without using the MO decomposing is very similar, as can be seen in Figs. 12.23 and 12.24. The extrapolation spectrum in Fig. 12.23 using MO decomposition is an improvement to the extrapolation spectra using decomposition including all transitions in Figs. 12.21 and 12.22.

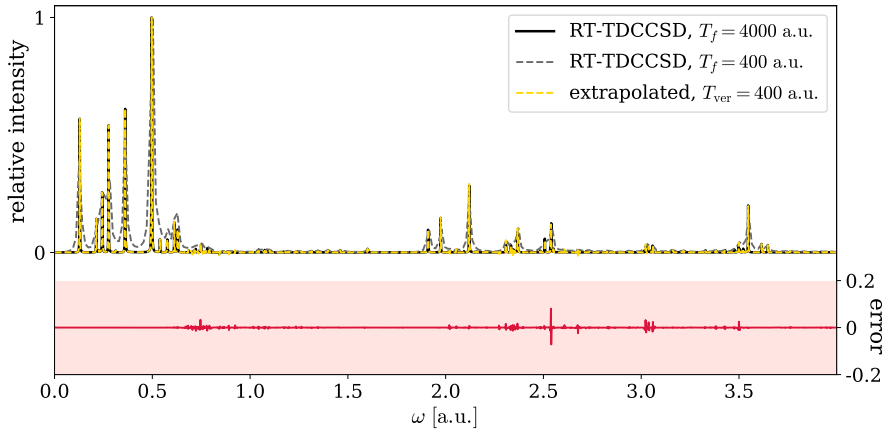

Figure 12.23: Evaluation of the extrapolation of $\mu^z(t) \approx \sum_{ia} \tilde{\mu}^z_{ia}(t)$ of LiH from 400 a.u. to 4000 a.u., using MO decomposition. The spectrum of the extrapolation $\tilde{I}_z(\omega)$ is shown in yellow, the spectrum of the short trajectory is gray and long trajectory spectrum $I_z(\omega)$ is shown in black. The red area shows the error $\tilde{I}_z(\omega) - I_z(\omega)$.

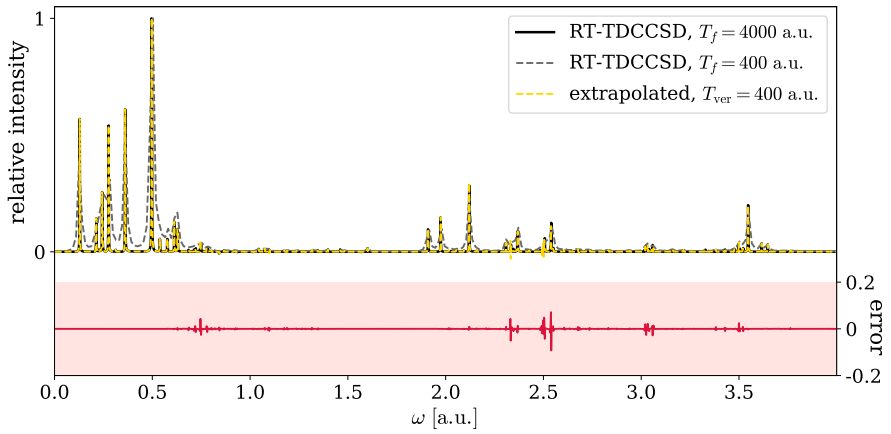

Figure 12.24: Evaluation of the extrapolation of $\mu^z(t) \approx \sum_{ia} \tilde{\mu}^z_{ia}(t)$ of LiH from 400 a.u. to 4000 a.u.. The spectrum of the extrapolation $\tilde{I}_z(\omega)$ is shown in yellow, the spectrum of the short trajectory is gray and long trajectory spectrum $I_z(\omega)$ is shown in black. The red area shows the error $\tilde{I}_z(\omega) - I_z(\omega)$.

12.3.3 Valence to Virtual Transitions

In this section, the transitions from the core orbital ψ_0 will also be omitted. The dipole moment will be given by

$$\mu^z(t) \approx \sum_a \mu^z_{1a}(t) \tag{12.4}$$

only including the MO components corresponding to transitions from the valence orbital ψ_1 to virtual orbitals $\psi_a \in \{\psi_2, \ldots, \psi_{31}\}$. The MO decomposition treats all components $\mu^z_{1a}(t)$ separately. The extrapolation error of the dipole moment only consists of transitions from the valence orbital to virtual orbitals is given in Table 12.3.

Table 12.3: Coefficient of determination when fitting $\mu^z(t)$ of LiH, using MO decomposition. Only using transitions from the valence orbitals to the virtual orbitals.

	$\boldsymbol{E}_{\text{full}}$	
$\boldsymbol{T}_{\text{ver}}$ [a.u.]	**decomposed**	**not decomposed**
10	2	3
20	2	7
50	2	$1 \cdot 10$
75	2	2
100	1	2
150	$4 \cdot 10^{-1}$	$4 \cdot 10^{-1}$
200	$7 \cdot 10^{-2}$	$5 \cdot 10^{-1}$
300	$7 \cdot 10^{-3}$	$6 \cdot 10^{-3}$
400	$3 \cdot 10^{-4}$	$3 \cdot 10^{-4}$
500	$4 \cdot 10^{-4}$	$5 \cdot 10^{-4}$
600	$3 \cdot 10^{-4}$	$2 \cdot 10^{-4}$
750	$6 \cdot 10^{-4}$	$3 \cdot 10^{-4}$
1000	$2 \cdot 10^{-4}$	$2 \cdot 10^{-5}$
1250	$3 \cdot 10^{-6}$	$5 \cdot 10^{-7}$
1500	$2 \cdot 10^{-7}$	$8 \cdot 10^{-8}$
1750	$3 \cdot 10^{-8}$	$4 \cdot 10^{-8}$

Fitting of the valence-virtual dipole moment without decomposition shows slightly lower extrapolation error compared to the fitting of the full z-component and the valence-virtual dipole in Tables 12.1 and 12.2, respectively. Not including the core orbitals might have somewhat simplified the fitting of the dipole moment. There seems to be no clear trend in Table 12.3 of the extrapolation error being either improved nor worsened by using MO decomposition.

The spectra only including the dipole components corresponding to transitions from the valence orbital to the virtual orbitals are shown in Figs. 12.25 and 12.26. As in the previous cases, the error in the extrapolation spectra using $T_{\text{ver}} = 400$ a.u. with and without using the MO decomposing is very similar.

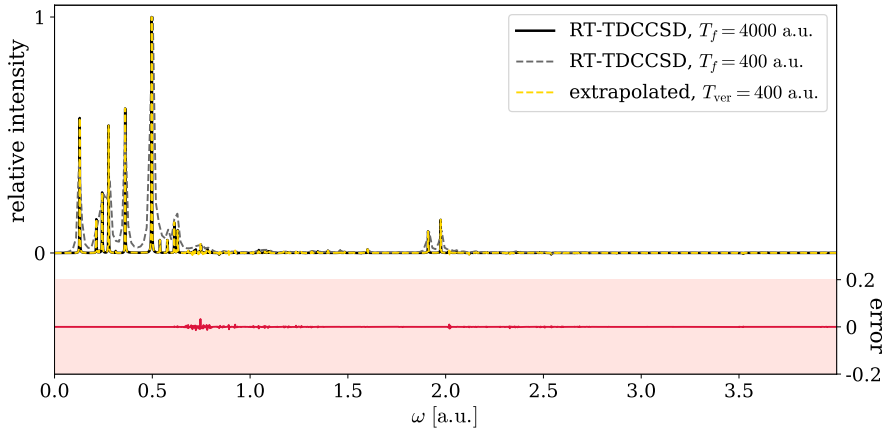

Figure 12.25: Evaluation of the extrapolation of $\mu^z(t) \approx \sum_a \tilde{\mu}^z_{1a}(t)$ of LiH from 400 a.u. to 4000 a.u., using MO decomposition. The spectrum of the extrapolation $\tilde{I}_z(\omega)$ is shown in yellow, the spectrum of the short trajectory is gray and long trajectory spectrum $I_z(\omega)$ is shown in black. The red area shows the error $\tilde{I}_z(\omega) - I_z(\omega)$.

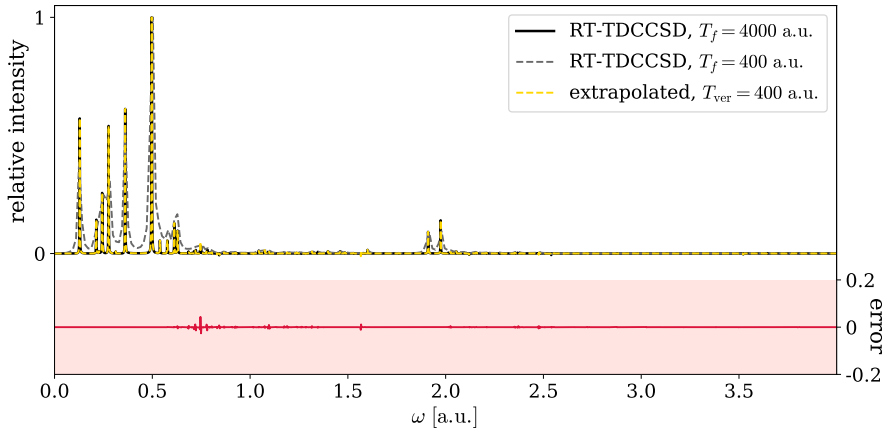

Figure 12.26: Evaluation of the extrapolation of $\mu^z(t) \approx \sum_a \tilde{\mu}^z_{1a}(t)$ of LiH from 400 a.u. to 4000 a.u., using MO decomposition. The spectrum of the extrapolation $\tilde{I}_z(\omega)$ is shown in yellow, the spectrum of the short trajectory is gray and long trajectory spectrum $I_z(\omega)$ is shown in black. The red area shows the error $\tilde{I}_z(\omega) - I_z(\omega)$.

CHAPTER 13

Summary and Conclusion

This final chapter concludes this master thesis. Staring with a summary of the discussions of the results of the studies made in this project, the chapter will move on to reflect on future development of the fitting model. Lastly, the conclusion of this mater project is presented.

13.1 Overview of the Discussion

This section provides a summary of the discussions given when presenting the results. The summary focuses on a broader view compared to the more detailed discussions in the previous chapters.

13.1.1 Evaluation of the Fitting Model

The error in the fitted dipole moment $\tilde{\mu}^z(t)$ decreased when increasing the trajectory length used in the fitting. This trend was observed for all the studied systems regardless of the method of regression, as seen in Tables 11.1 to 11.10. The error of the fitted dipole moment $\tilde{\mu}^z(t)$ using LASSO was very similar to the error when using OLS. The LASSO method constrained the sign of the coefficients, using the form of the first order perturbation correction of the dipole moment shown in Eq. (4.25). The LASSO method gave marginally, but consistently, lower error compared to the OLS method.

The parameter study in Section 10.2.2 indicates that the error in the fitting model is dominated by the frequency estimation. When the frequencies were estimated using trajectory length T_f, the error remained almost unchanged when using $\geq 100\%$, 100% or 75% of the trajectory for the fitting of the linear coefficients. This can be seen in Figs. 10.3 to 10.5. These figures also show the same trend as in the Fourier-Padé study of Mattiat and Luber[17]. The error is determined by the trajectory length T_f, and not by the step length Δt. Looking at Figs. 10.3 to 10.5 showing the error along with Fig. 10.7 even suggests that increasing the step length might be beneficial when the trajectory is longer. The number of estimated frequencies was seen to increase when the time step was decreased, without significant improvement in the fitting.

In general, the fitting method gave equally good or slightly better approximations to the true high resolution spectra compared to the Fourier-Padé approximant. The difference was very small in the cases where the fitting model produced spectra indistinguishable from the true high resolution spectra. These

examples are shown in Figs. 11.1, 11.5, 11.11 and 11.16, where the OLS method was used, and the cases using LASSO are shown in Figs. 11.25, 11.27, 11.29 and 11.31. In these cases, the error in the Fourier-Padé shown in Figs. 11.36, 11.38, 11.40 and 11.42 was negligible, giving the Fourier-Padé an advantage as it is cheaper.

When neither method produced perfect spectra, the fitting model generally produced better approximations to the true spectra. The helium atom (using the aug-cc-pVTZ basis) serves as an example. The spectrum in Fig. 11.37 shows that the Fourier-Padé approximant failed to provide all but the most prominent peak. The spectra obtained from the extrapolations using the same trajectory length account for all the peaks in the spectrum, although the peaks were slightly shifted. These spectra from the extrapolation using OLS and LASSO are shown in Figs. 11.3 and 11.26, respectively.

In some cases, the spectrum of the extrapolated dipole moment contained unwanted peaks when using OLS to determine the coefficients. These unwanted peaks consisted of two or more narrowly spaced peaks with alternating sign. An illustrative example is the beryllium atom (using the aug-cc-pVTZ basis). The failed OLS fitting is shown on Fig. 11.13. In this case, the Fourier-Padé approximant shown in Fig. 11.41 also failed, where one of the prominent peaks was flipped. Only the spectrum obtained from the LASSO fitting shown in Fig. 11.30 gave a decent approximation to the true high resolution spectrum. In other cases where the OLS fitting showed unwanted peaks, the Fourier-Padé approximant and the LASSO fitting achieved similar accuracy in the approximation of the spectrum. The OLS fitting of the dipole moment of lithium hydride (using the aug-cc-pVDZ basis) seen in Fig. 11.18 also contained such a pollution in the spectrum. The corresponding spectra obtained by the Fourier-Padé in Fig. 11.43 and the LASSO fitting in Fig. 11.32 both provided fairly accurate approximations to the absorption spectrum.

13.1.2 The Convergence Criterion

The convergence criterion must be based on the available data, meaning that only E_{ver} and E_{fit} from Eq. (11.2) may be used in such a criterion. The most important observation will therefore be the correlation between the error in the verification window E_{ver} and the accuracy of the approximated absorption spectrum. This self-evaluation gives the fitting model an advantage to the methods of harmonic inversion. No final convergence criterion was found for the fitting model in this project, but several observations were made.

When the verification error of the fitted function $\tilde{\mu}^z(t)$ was around $E_{\text{ver}} \sim 10^{-5}$, the corresponding spectra were mostly decent approximations. A verification error of $E_{\text{ver}} \sim 10^{-6}$ gave very good approximations, while $E_{\text{ver}} \sim 10^{-7}$ mostly corresponded to an almost perfect approximation to the absorption spectrum. The approximated spectra were indistinguishable from the true high resolution spectra when the verification error was even smaller, $E_{\text{ver}} < 10^{-7}$.

A verification error of $E_{\text{ver}} \geq 1$ gave in all cases very bad approximations to the absorption spectrum. A verification error of $E_{\text{ver}} \sim 10^{-4}$ meant visible inaccuracies in the extrapolation spectra, but in several cases still gave quite decent approximations. The same was true for $E_{\text{ver}} \sim 10^{-3}$, and even cases with a verification error of $E_{\text{ver}} \sim 10^{-2}$ gave acceptable spectra. In these cases, the

success of the extrapolation was also determined by the measure of over-fitting, $E_{\text{ver}}/E_{\text{fit}}$. For the fitted functions $\tilde{\mu}^z(t)$ using OLS to optimize the coefficients, the extrapolation would only be stable enough if $E_{\text{ver}}/E_{\text{fit}} < 10^3$. The LASSO method was moderately less prone to over-fitting. When using LASSO to determine the linear coefficients, the extrapolation spectra were decent only if $E_{\text{ver}}/E_{\text{fit}} < 10^2$. A verification error of $E_{\text{ver}} \sim 10^{-1}$ could be anything from a poor approximation to a relatively decent spectrum with visible error.

From analyzing the limited number of systems in this study, it appears that the convergence criterion should not only include the verification error E_{ver}, but also consider the ratio between the verification error and the fitting error, E_{fit}. A high ratio $E_{\text{ver}}/E_{\text{fit}}$ is a sign of over-fitting, and was shown to be a sign of unstable extrapolation. A larger scale study is needed in order to determine the correlation between the measured error in the time domain and the observed accuracy of the approximated spectrum. It is clear that there is a trade-off between the accuracy of the extrapolation and the length of the dipole trajectory.

13.1.3 Molecular Orbital Decomposition

The spectra were seen to be dominated by contributions of the dipole components μ_{ia}^z corresponding to transitions between an occupied and a virtual orbital, as seen in Figs. 12.10, 12.12, 12.14, 12.16 and 12.18. The MO decomposition was not found to be suited for assigning molecular orbital transitions to the peaks in the spectrum. As seen in Figs. 12.11, 12.13, 12.15, 12.17 and 12.19, each of the components μ_{ia}^z contributed to several peaks, and a single component was seen to be the largest contributor to several peaks in the spectrum. Assigning the same orbital transition to several peaks would not make sense.

The MO decomposition in RT-TDCCSD seems to be less helpful compared to the MO decomposition for the Fourier-Padé approximant using RT-TDDFT simulations.[12] The extrapolation error in Tables 12.1 to 12.3 did not decrease when using the fitting model on the decomposed dipole moment of lithium hydride (using the aug-cc-pVDZ basis set). Limiting the fitting of the dipole moment to only include the transitions from the valence orbitals to the virtual orbitals was seen to slightly improve the approximated dipole moment $\tilde{\mu}^z(t)$ for lithium hydride. For larger systems, it may simplify the fitting of the dipole moment to use the frozen core approximation. This would avoid the high energy core excitations. Further testing is needed for a conclusive result.

13.2 Future Work

The fitting model was developed in the limited time of a master thesis, and there are naturally many studies to be done and alternative approaches worth exploring. The newly developed model therefore has a lot of potential for improvement. This section reflects on some prospective changes.

13.3 Improving Frequency Estimation

The result of the extrapolation of the dipole moment relies heavily on the frequency estimation. The method for estimating the frequencies has several

areas which have potential for improvement.

Finding the roots of of the polynomial $Q(z)$ in the Fourier-Padé approximant was observed to be the most computationally demanding part in the fitting model. Finding a faster algorithm to obtain the roots of $Q(z)$ would improve the usability of the fitting model.

The fitting model could be stabilized by finding a better way to separate out the roots of $Q(z)$ corresponding to actual frequencies from the vast number of redundant roots.

The estimated frequencies suffer from imprecision when shorter dipole trajectories are used. Further development of the fitting model could include non-linear optimization methods to improve the estimated frequencies, such as various versions of gradient decent. This could potentially significantly decrease the necessary dipole trajectory length for a satisfactory extrapolation.

Other methods for frequency estimation should also be explored. Only the Fourier-Padé approximant was tested for estimating the frequencies of the methods of harmonic inversion. The filter-diagonalization method[6] could be a potential alternative for estimating frequencies.

Another alternative could be to use an estimate of the fundamental frequency, as is common in the four-parameter sine fitting[48]. The dipole moment would then be a truncated Fourier series using the estimated fundamental frequency.

13.3.1 Larger Scale Testing

Testing the fitting model on more systems may reveal trends and weaknesses which may be used to further develop the model. This should include larger molecules than the small systems included in this thesis, to see how the fitting model handles denser spectra.

It would also be interesting to see if the fitting model is more successful when using the *frozen core* approximation. This should effectively limit the range of frequencies by removing the high energy core excitations.

The fitting model has only been tried out on dipole data obtained by RT-TDCC theory. A natural next step would therefore be to test the model obtained by other electronic structure models, like for example RT-TDCI theory or RT-TDDFT. The Fourier-Padé approximant was improved when using MO decomposition for RT-TDDFT dipole data.[12] The MO decomposition could potentially work better when using the fitting model on RT-TDDFT dipole data.

The correlation between the fitting error in the time domain and the more qualitative assessment of the resulting spectra should be tested extensively. This is needed in order to conclusively find a reliable convergence criterion such that automatic termination of the real-time simulations may be enabled.

13.4 Restrictive Models

Restricting the fitting model based on knowledge about the physical properties of the electric dipole moment is key to avoid over-fitting on short trajectories. The induced dipole moment of the few systems included in this study was successfully approximated using the form of the first order correction in Eq. (4.25), obtained through linear response theory. The form of the induced dipole moment was

derived using the delta-pulse specifically, and it is therefore unknown if the assumption will hold when using other types of laser fields. In order to exclude many-photon transitions, the upper limit of the field strength could also be investigated. The limit might vary for different molecules.

Restricting the fitting model has potential to greatly stabilize the extrapolation of the dipole moment. Adding assumptions which restrict the form of the dipole moment is therefore encouraged, but mathematical proof is needed to survey the limitations this could enforce on the use case of the fitting model.

Tailoring the fitting model with additional knowledge of the dipole moment function form might require a more flexible method than the methods for linear regression used in this thesis. Artificial neural networks could be an alternative, given that the physics would guide the architecture of the neural network.

13.5 Conclusion

In this master thesis, a fitting model was developed for creating a function $\tilde{\mu}(t)$ to approximate the electric dipole moment $\mu(t)$ obtained from real-time time-dependent coupled cluster simulations. The approximated function $\tilde{\mu}(t)$ was used to extrapolate the dipole moment in order to achieve high resolution absorption spectra.

The extrapolation of the full z-component of the dipole moment of He, H_2 and Be obtained by RT-TDCCSD calculations using the aug-cc-pVTZ basis set was highly successful. The extrapolations gave completely accurate spectra from short trajectories of $\mu^z(t)$. The fitting model required only dipole trajectories up to $T_v = 20$ a.u. for the helium atom, $T_v = 100$ a.u. for the hydrogen molecule and $T_v = 150$ a.u. for the beryllium atom. The spectra from the extrapolated functions $\tilde{\mu}^z$ were then indistinguishable from that obtained by long simulations (up to $T_f = 6000$ a.u. for He and Be and up to $T_f = 8000$ a.u. for H_2).

When extrapolating the z-component of the dipole moment of LiH from RT-TDCCSD calculations using the aug-cc-pVDZ basis set, the fitting model needed a dipole trajectory computed up to $T_v = 1250$ a.u. in order to obtain a perfect match with the true high resolution spectrum obtained by sampling the dipole moment up to $T_f = 8000$ a.u. from the real-time simulations. The spectrum was well approximated when using dipole trajectories $T_v \geq 300$ a.u., except for the occasional presence of two or more narrowly spaced additional peaks with alternating sign. This kind of pollution in the approximated spectrum was eliminated by enforcing the expected sign of the coefficients, found using linear response theory. This more restricted form of the dipole moment worked well for all the systems included in this study, improving the stability and accuracy of the extrapolations.

The difficulty of extrapolating the dipole moment was seen to increase with the spectral density. The fitting model was unable to perfectly reproduce the high resolution spectrum ($T_f = 8000$ a.u.) for the water molecule using the aug-cc-pVDZ basis. Enforcing the form of the dipole moment from linear response theory greatly improved the accuracy of the approximated spectra of the water molecule, giving decent approximations, though with visible errors in the spectrum when using $T_v \geq 300$ a.u. for the dipole fitting.

Combining the fitting model with molecular orbital decomposition was not seen to improve the accuracy of the dipole extrapolation. The extrapolation of

$\mu^z(t)$ of lithium hydride was slightly improved when only including the dipole components corresponding to transitions from valence to virtual orbitals.

A convergence criterion for the fitting model was investigated, using the coefficient of determination for the measure of error. The short dipole trajectory used for the extrapolation was divided into fitting data, used in the linear regression, and verification data. A perfectly approximated dipole moment gave errors which conclusively indicated the success of the fitting. A decent, but not perfect approximation to the spectrum gave more unreliable errors to interpret. Although the convergence criterion is not yet conclusively determined, the self-evaluation of the fitting model provides an advantage over the methods of harmonic inversion, like the Fourier-Padé approximant.

The initial investigations of the fitting model show great potential. The current model already successfully extrapolated the dipole moment from shorter dipole trajectories of atoms and small molecules. The next step in developing the fitting model will be to test the model on dipole data from real-time time-dependent density functional theory. A larger scale study of the convergence criterion should also be conducted.

Appendices

APPENDIX A

Molecular Orbital Energies

The molecular orbital decomposition used in the fitting of the electric dipole moment in Section 12.3 exploited degeneracy among the molecular orbitals. The discussion regarding similarity clustering of the decomposed dipole moment in Chapter 12 also used information about the molecular orbital degeneracy.

The molecular orbital energies of all the systems included in this study are therefore listed in Table A.1.

The reference states in the coupled cluster calculations used in this project were closed-shell restricted Hartree-Fock states. The orbital energies are the eigenvalues of the Fock operator:

$$\hat{f}\,|\psi_p\rangle = \varepsilon_p\,|\psi_p\rangle\,. \tag{A.1}$$

The helium atom, the hydrogen molecule and the beryllium atom all used aug-cc-pVTZ basis sets. The water molecule and lithium hydride both used aug-cc-pVDZ basis sets. Further details on the simulation are found in Section 10.1.

Table A.1: Molecular orbital energies in atomic units.

	He	**H_2**	**Be**	**LiH**	**H_2O**
ε_0	−0.91787	−0.59440	−4.7327	−2.4564	−20.577
ε_1	0.11054	0.052563	−0.30928	−0.29938	−1.3568
ε_2	0.42677	0.053105	0.017885	−0.0080780	−0.71940
ε_3	0.42677	0.19037	0.017885	0.012335	−0.58571
ε_4	0.42677	0.20889	0.017885	0.012335	−0.50946
ε_5	0.83911	0.20889	0.034539	0.019264	0.035441
ε_6	1.5201	0.28471	0.064448	0.031096	0.057930
ε_7	1.5201	0.29744	0.064448	0.051086	0.17397
ε_8	1.5201	0.29744	0.064448	0.051086	0.19666
ε_9	1.5201	0.41741	0.17787	0.081115	0.22267
ε_{10}	1.5201	0.42050	0.17787	0.14356	0.23143
ε_{11}	1.9621	0.73736	0.17787	0.17807	0.29087
ε_{12}	1.9621	0.79136	0.17787	0.18624	0.33151
ε_{13}	1.9621	0.79136	0.17787	0.18624	0.38583
ε_{14}	4.8165	0.88394	0.26528	0.19283	0.40412
ε_{15}	7.1084	0.88394	0.27149	0.19283	0.43385
ε_{16}	7.1084	0.90320	0.27149	0.19782	0.53926
ε_{17}	7.1084	0.93145	0.27149	0.19782	0.64873
ε_{18}	7.1084	0.93145	0.49113	0.23697	0.65824
ε_{19}	7.1084	1.0473	0.49113	0.42346	0.81202
ε_{20}	8.2211	1.0482	0.49113	0.52531	0.92994
ε_{21}	8.2211	1.0482	0.49113	0.52531	1.1009
ε_{22}	8.2211	1.0670	0.49113	0.53574	1.1152
ε_{23}	-	1.0670	0.49113	0.53574	1.1489
ε_{24}	-	1.5233	0.49113	0.54491	1.3080
ε_{25}	-	1.9386	0.58448	0.54491	1.4672
ε_{26}	-	1.9386	0.58448	0.54770	1.4833
ε_{27}	-	2.1250	0.58448	0.96545	1.5839
ε_{28}	-	2.5965	0.58448	1.5500	2.0039
ε_{29}	-	2.9360	0.58448	2.0260	2.0118
ε_{30}	-	3.6156	1.0165	2.0332	2.1093
ε_{31}	-	3.6156	1.0165	2.0332	2.3685
ε_{32}	-	3.6339	1.0165	-	2.4831
ε_{33}	-	3.6339	1.4756	-	2.6290
ε_{34}	-	4.1566	1.4756	-	2.7155
ε_{35}	-	4.4063	1.4756	-	2.9667
ε_{36}	-	4.4063	1.4756	-	3.6730
ε_{37}	-	4.4311	1.4756	-	3.6905
ε_{38}	-	4.4311	1.5873	-	3.7031
ε_{39}	-	4.4883	1.5873	-	4.0276
ε_{40}	-	4.4883	1.5873	-	4.3098
ε_{41}	-	5.1907	1.5873	-	-
ε_{42}	-	5.7854	1.5873	-	-
ε_{43}	-	5.7854	1.5873	-	-
ε_{44}	-	5.9920	1.5873	-	-
ε_{45}	-	7.1222	1.7082	-	-

Bibliography

1. Mandelshtam, V. A. & Taylor, H. S. Harmonic inversion of time signals and its applications. *The Journal of Chemical Physics* **107,** 6756–6769. doi:10.1063/1.475324 (1997).
2. Schmidt, R. Multiple emitter location and signal parameter estimation. *IEEE Transactions on Antennas and Propagation* **34,** 276–280. doi:10.1109/TAP.1986.1143830 (1986).
3. Roy, R. & Kailath, T. ESPRIT-estimation of signal parameters via rotational invariance techniques. *IEEE Transactions on Acoustics, Speech, and Signal Processing* **37,** 984–995. doi:10.1109/29.32276 (1989).
4. Roy, R., Sumpter, B. G., Noid, D. W. & Wunderlich, B. Estimation of dispersion relations from short-duration molecular dynamics simulations. *The Journal of Physical Chemistry* **94,** 5720–5729. doi:10.1021/j100378a023 (1990).
5. Roy, R., Sumpter, B., Pfeffer, G., Gray, S. & Noid, D. Novel methods for spectral analysis. *Physics Reports* **205,** 109–152. doi:10.1016/0370-1573(91)90044-M (1991).
6. Neuhauser, D. Bound state eigenfunctions from wave packets: Time→energy resolution. *The Journal of Chemical Physics* **93,** 2611–2616. doi:10.1063/1.458900 (1990).
7. Wall, M. R. & Neuhauser, D. Extraction, through filter-diagonalization, of general quantum eigenvalues or classical normal mode frequencies from a small number of residues or a short-time segment of a signal. I. Theory and application to a quantum-dynamics model. *The Journal of Chemical Physics* **102,** 8011–8022. doi:10.1063/1.468999 (1995).
8. Mandelshtam, V. FDM: the filter diagonalization method for data processing in NMR experiments. *Progress in Nuclear Magnetic Resonance Spectroscopy* **38,** 159–196. doi:10.1016/S0079-6565(00)00032-7 (2001).
9. Mandelshtam, V. A. & Taylor, H. S. A low-storage filter diagonalization method for quantum eigenenergy calculation or for spectral analysis of time signals. *The Journal of Chemical Physics* **106,** 5085–5090. doi:10.1063/1.473554 (1997).

10. Beck, M. H. & Meyer, H.-D. Extracting accurate bound-state spectra from approximate wave packet propagation using the filter-diagonalization method. *The Journal of Chemical Physics* **109,** 3730–3741. doi:10.1063/1.476974 (1998).

11. Martini, B. R., Aizikov, K. & Mandelshtam, V. A. The filter diagonalization method and its assessment for Fourier transform mass spectrometry. *International Journal of Mass Spectrometry* **373,** 1–14. ISSN: 1387-3806. doi:10.1016/j.ijms.2014.08.010 (2014).

12. Bruner, A., LaMaster, D. & Lopata, K. Accelerated Broadband Spectra Using Transition Dipole Decomposition and Padé Approximants. *Journal of Chemical Theory and Computation* **12,** 3741–3750. doi:10.1021/acs.jctc.6b00511 (2016).

13. Repisky, M., Konecny, L., Kadek, M., Komorovsky, S., Malkin, O. L., Malkin, V. G. & Ruud, K. Excitation Energies from Real-Time Propagation of the Four-Component Dirac–Kohn–Sham Equation. *Journal of Chemical Theory and Computation* **11,** 980–991. doi:10.1021/ct501078d (2015).

14. Kadek, M., Konecny, L., Gao, B., Repisky, M. & Ruud, K. X-ray absorption resonances near L2,3-edges from real-time propagation of the Dirac–Kohn–Sham density matrix. *Phys. Chem. Chem. Phys.* **17,** 22566–22570. doi:10.1039/C5CP03712C (2015).

15. Nascimento, D. R. & DePrince, A. E. Simulation of Near-Edge X-ray Absorption Fine Structure with Time-Dependent Equation-of-Motion Coupled-Cluster Theory. *The Journal of Physical Chemistry Letters* **8,** 2951–2957. doi:10.1021/acs.jpclett.7b01206 (2017).

16. Ghosh, S., Asher, J. C., Gagliardi, L., Cramer, C. J. & Govind, N. A semiempirical effective Hamiltonian based approach for analyzing excited state wave functions and computing excited state absorption spectra using real-time dynamics. *The Journal of Chemical Physics* **150,** 104103. doi:10.1063/1.5061746 (2019).

17. Mattiat, J. & Luber, S. Efficient calculation of (resonance) Raman spectra and excitation profiles with real-time propagation. *The Journal of Chemical Physics* **149,** 174108. doi:10.1063/1.5051250 (2018).

18. Li, X., Govind, N., Isborn, C., DePrince, A. E. & Lopata, K. Real-Time Time-Dependent Electronic Structure Theory. *Chemical Reviews* **120,** 9951–9993. doi:10.1021/acs.chemrev.0c00223 (2020).

19. Szabo, A. *Modern quantum chemistry : introduction to advanced electronic structure theory* ISBN: 0029497108 (Macmillam, New York, 1982).

20. Helgaker, T., Jørgensen, P. & Olsen, J. *Second Quantization* in *Molecular Electronic-Structure Theory* 1–33 (John Wiley & Sons, Ltd, 2000). ISBN: 9781119019572. doi:10.1002/9781119019572.ch1.

21. Helgaker, T., Jørgensen, P. & Olsen, J. *Spin in Second Quantization* in *Molecular Electronic-Structure Theory* 34–79 (John Wiley & Sons, Ltd, 2000). ISBN: 9781119019572. doi:10.1002/9781119019572.ch2.

22. Born, M. & Oppenheimer, R. Zur Quantentheorie der Molekeln. *Annalen der Physik* **389,** 457–484. doi:10.1002/andp.19273892002 (1927).

23. Pedersen, T. B., Kristiansen, H. E., Bodenstein, T., Kvaal, S. & Schøyen, Ø. S. Interpretation of Coupled-Cluster Many-Electron Dynamics in Terms of Stationary States. *Journal of Chemical Theory and Computation* **17,** 388–404. doi:10.1021/acs.jctc.0c00977 (2021).

24. Helgaker, T., Jørgensen, P. & Olsen, J. *The Standard Models* in *Molecular Electronic-Structure Theory* 142–200 (John Wiley & Sons, Ltd, 2000). ISBN: 9781119019572. doi:10.1002/9781119019572.ch5.

25. Griffiths, D. J. *Introduction to quantum mechanics* 2nd ed. ISBN: 9781107179868 (Cambridge University Press, Cambridge, 2017).

26. Kvaal, S. Ab initio quantum dynamics using coupled-cluster. *The Journal of Chemical Physics* **136,** 194109. doi:10.1063/1.4718427 (2012).

27. Madsen, N. K., Hansen, M. B., Christiansen, O. & Zoccante, A. Time-dependent vibrational coupled cluster with variationally optimized time-dependent basis sets. *The Journal of Chemical Physics* **153,** 174108. doi:10.1063/5.0024428 (2020).

28. Helgaker, T., Jørgensen, P. & Olsen, J. *Hartree-Fock Theory* in *Molecular Electronic-Structure Theory* 433–522 (John Wiley & Sons, Ltd, 2000). ISBN: 9781119019572. doi:10.1002/9781119019572.ch10.

29. Helgaker, T., Jørgensen, P. & Olsen, J. *Coupled-Cluster Theory* in *Molecular Electronic-Structure Theory* 648–723 (John Wiley & Sons, Ltd, 2000). ISBN: 9781119019572. doi:10.1002/9781119019572.ch13.

30. Helgaker, T., Jørgensen, P. & Olsen, J. *Gaussian Basis Sets* in *Molecular Electronic-Structure Theory* 287–335 (John Wiley & Sons, Ltd, 2000). ISBN: 9781119019572. doi:10.1002/9781119019572.ch8.

31. Feynman, R. P. Forces in Molecules. *Phys. Rev.* **56,** 340–343. doi:10.1103/PhysRev.56.340 (1939).

32. Koch, H. & Jørgensen, P. Coupled cluster response functions. *The Journal of Chemical Physics* **93,** 3333–3344. doi:10.1063/1.458814 (1990).

33. Pedersen, T. B. & Kvaal, S. Symplectic integration and physical interpretation of time-dependent coupled-cluster theory. *The Journal of Chemical Physics* **150,** 144106. doi:10.1063/1.5085390. (2021) (2019).

34. Huber, C. & Klamroth, T. Explicitly time-dependent coupled cluster singles doubles calculations of laser-driven many-electron dynamics. *The Journal of Chemical Physics* **134,** 054113. doi:10.1063/1.3530807 (2011).

35. Goings, J. J., Lestrange, P. J. & Li, X. Real-time time-dependent electronic structure theory. *WIREs Computational Molecular Science* **8,** e1341. doi:10.1002/wcms.1341 (2018).

36. Olsen, J. & Jørgensen, P. Linear and nonlinear response functions for an exact state and for an MCSCF state. *The Journal of Chemical Physics* **82,** 3235–3264. doi:10.1063/1.448223 (1985).

37. Pedersen, T. B. *Introduction to Response Theory* in *Handbook of Computational Chemistry* (eds Leszczynski, J., Kaczmarek-Kedziera, A., Puzyn, T., G. Papadopoulos, M., Reis, H. & K. Shukla, M.) 269–294 (Springer International Publishing, Cham, 2017). ISBN: 978-3-319-27282-5. doi:10.1007/978-3-319-27282-5_5.

38. Ehrenfest, P. Bemerkung über die angenäherte Gültigkeit der klassischen Mechanik innerhalb der Quantenmechanik. *Zeitschrift für Physik* **45,** 455–457. ISSN: 0044-3328. doi:10.1007/BF01329203 (1927).

39. Kristensen, K., Kauczor, J., Kjærgaard, T. & Jørgensen, P. Quasienergy formulation of damped response theory. *The Journal of Chemical Physics* **131,** 044112. doi:10.1063/1.3173828 (2009).

40. Hastie, T., Tibshirani, R. & Friedman, J. *Neural Networks* in *The Elements of Statistical Learning: Data Mining, Inference, and Prediction* 389–416 (Springer New York, New York, NY, 2009). ISBN: 978-0-387-84858-7. doi:10.1007/978-0-387-84858-7_11.

41. Dral, P. O. Quantum Chemistry in the Age of Machine Learning. *The Journal of Physical Chemistry Letters* **11,** 2336–2347. doi:10.1021/acs.jpclett.9b03664 (2020).

42. Häse, F., Fdez. Galván, I., Aspuru-Guzik, A., Lindh, R. & Vacher, M. How machine learning can assist the interpretation of ab initio molecular dynamics simulations and conceptual understanding of chemistry. *Chem. Sci.* **10,** 2298–2307. doi:10.1039/C8SC04516J (8 2019).

43. Friederich, P., dos Passos Gomes, G., De Bin, R., Aspuru-Guzik, A. & Balcells, D. Machine learning dihydrogen activation in the chemical space surrounding Vaska's complex. *Chem. Sci.* **11,** 4584–4601. doi:10.1039/D0SC00445F (2020).

44. Butler, K. T., Davies, D. W., Cartwright, H., Isayev, O. & Walsh, A. Machine learning for molecular and materials science. *Nature* **559,** 547–555. ISSN: 1476-4687. doi:10.1038/s41586-018-0337-2 (2018).

45. Kitchin, J. R. Machine learning in catalysis. *Nat Catal* **1,** 230–232. ISSN: 2520-1158. doi:10.1038/s41929-018-0056-y (2018).

46. Xu, K., Zhang, M., Li, J., Du, S. S., Kawarabayashi, K.-i. & Jegelka, S. *How Neural Networks Extrapolate: From Feedforward to Graph Neural Networks* https://arxiv.org/abs/2009.11848.

47. Oleinik, A. What are neural networks not good at? On artificial creativity. *Big Data & Society* **6,** 2053951719839433. doi:10.1177/2053951719839433 (2019).

48. Ramos, P., Fonseca da Silva, M., Martins, R. & Serra, A. Simulation and experimental results of multiharmonic least-squares fitting algorithms applied to periodic signals. *IEEE Transactions on Instrumentation and Measurement* **55,** 646–651. doi:10.1109/TIM.2006.864260 (2006).

49. Schoukens, J., Pintelon, R. & Van Hamme, H. The interpolated fast Fourier transform: a comparative study. *IEEE Transactions on Instrumentation and Measurement* **41,** 226–232. doi:10.1109/19.137352 (1992).

50. Fonseca da Silva, M., Ramos, P. M. & Serra, A. A new four parameter sine fitting technique. *Measurement* **35,** 131–137. ISSN: 0263-2241. doi:10.1016/j.measurement.2003.08.006 (2004).

51. Chen, J., Ren, Y. & Zeng, G. An improved Multi-harmonic Sine Fitting Algorithm based on Tabu Search. *Measurement* **59,** 258–267. ISSN: 0263-2241. doi:10.1016/j.measurement.2014.09.035 (2015).

52. Salinas, J., Garcia-Lagos, F., Joya, G. & Sandoval, F. Sine-fitting multiharmonic algorithms implemented by artificial neural networks. *Neurocomputing* **72,** 3640–3648. ISSN: 0925-2312. doi:10.1016/j.neucom.2009.01.017 (2009).

53. Xu, L. & Ding, F. Recursive Least Squares and Multi-innovation Stochastic Gradient Parameter Estimation Methods for Signal Modeling. *Circuits Syst Signal Process* **36,** 1735–1753. ISSN: 1531-5878. doi:10.1007/s00034-016-0378-4 (2017).

54. Langtangen, H. P. & Mardal, K.-A. *Function Approximation by Global Functions* in *Introduction to Numerical Methods for Variational Problems* 7–68 (Springer International Publishing, Cham, 2019). ISBN: 978-3-030-23788-2. doi:10.1007/978-3-030-23788-2_2.

55. Guo, W.-H., Li, W.-J. & Huang, Y.-Z. Computation of resonant frequencies and quality factors of cavities by FDTD technique and Pade approximation. *IEEE Microwave and Wireless Components Letters* **11,** 223–225. doi:10.1109/7260.923035 (2001).

56. Dey, S. & Mittra, R. Efficient computation of resonant frequencies and quality factors of cavities via a combination of the finite-difference time-domain technique and the Pade approximation. *IEEE Microwave and Guided Wave Letters* **8,** 415–417. doi:10.1109/75.746760 (1998).

57. Harris, C. R., Millman, K. J., van der Walt, S. J., Gommers, R., Virtanen, P., Cournapeau, D., Wieser, E., Taylor, J., Berg, S., Smith, N. J., Kern, R., Picus, M., Hoyer, S., van Kerkwijk, M. H., Brett, M., Haldane, A., del Río, J. F., Wiebe, M., Peterson, P., Gérard-Marchant, P., Sheppard, K., Reddy, T., Weckesser, W., Abbasi, H., Gohlke, C. & Oliphant, T. E. Array programming with NumPy. *Nature* **585,** 357–362. doi:10.1038/s41586-020-2649-2 (2020).

58. Hunter, J. D. Matplotlib: A 2D graphics environment. *Computing in Science & Engineering* **9,** 90–95. doi:10.1109/MCSE.2007.55 (2007).

59. Baker, G. A. & Graves-Morris, P. *Padé approximants and numerical methods* 2nd ed., 67–121. doi:10.1017/CBO9780511530074.005 (Cambridge University Press, 1996).

60. Virtanen, P., Gommers, R., Oliphant, T. E., Haberland, M., Reddy, T., Cournapeau, D., Burovski, E., Peterson, P., Weckesser, W., Bright, J., van der Walt, S. J., Brett, M., Wilson, J., Millman, K. J., Mayorov, N., Nelson, A. R. J., Jones, E., Kern, R., Larson, E., Carey, C. J., Polat, İ., Feng, Y., Moore, E. W., VanderPlas, J., Laxalde, D., Perktold, J., Cimrman, R., Henriksen, I., Quintero, E. A., Harris, C. R., Archibald, A. M., Ribeiro, A. H., Pedregosa, F., van Mulbregt, P. & SciPy 1.0 Contributors. SciPy 1.0: Fundamental Algorithms for Scientific Computing in Python. *Nature Methods* **17,** 261–272. doi:10.1038/s41592-019-0686-2 (2020).

61. Horn, R. A. & Johnson, C. R. *Norms for vectors and matrices* in *Matrix Analysis* 257–342 (Cambridge University Press, 1985). doi:10.1017/CBO9780511810817.007.

62. Hastie, T., Tibshirani, R. & Friedman, J. *Unsupervised Learning* in *The Elements of Statistical Learning: Data Mining, Inference, and Prediction* 485–585 (Springer New York, New York, NY, 2009). ISBN: 978-0-387-84858-7. doi:10.1007/978-0-387-84858-7_14.

63. Guttag, J. *Lecture 12: Clustering | Introduction to Computational Thinking and Data Science* Massachusetts Institute of Technology: MIT OpenCourseWare. 2016. https://ocw.mit.edu.

64. Hastie, T., Tibshirani, R. & Friedman, J. *Overview of Supervised Learning* in *The Elements of Statistical Learning: Data Mining, Inference, and Prediction* 9–41 (Springer New York, New York, NY, 2009). ISBN: 978-0-387-84858-7. doi:10.1007/978-0-387-84858-7_2.

65. Hastie, T., Tibshirani, R. & Friedman, J. *Linear Methods for Regression* in *The Elements of Statistical Learning: Data Mining, Inference, and Prediction* 43–99 (Springer New York, New York, NY, 2009). ISBN: 978-0-387-84858-7. doi:10.1007/978-0-387-84858-7_3.

66. Géron, A. *Hands-On Machine Learning with Scikit-Learn and TensorFlow: Concepts, Tools, and Techniques to Build Intelligent Systems* ISBN: 9781491962299 (O'Reilly Media, Incorporated, Sebastopol, 2017).

67. Heumann, C., Schomaker, M. & Shalabh. *Linear Regression* in *Introduction to Statistics and Data Analysis : With Exercises, Solutions and Applications in R* 249–295 (Springer International Publishing, Cham, 2016). ISBN: 978-3-319-46162-5. doi:10.1007/978-3-319-46162-5_11.

68. Pedregosa, F., Varoquaux, G., Gramfort, A., Michel, V., Thirion, B., Grisel, O., Blondel, M., Prettenhofer, P., Weiss, R., Dubourg, V., Vanderplas, J., Passos, A., Cournapeau, D., Brucher, M., Perrot, M. & Duchesnay, E. Scikit-learn: Machine Learning in Python. *Journal of Machine Learning Research* **12,** 2825–2830. https://dl.acm.org/doi/10.5555/1953048.2078195 (2011).

69. Gonzalez, R. C. *Digital image processing* 4th ed., 915–916. ISBN: 9781292223049 (Pearson, New York, 2018).

70. Kristiansen, H. E., Schøyen, Ø. S., Kvaal, S. & Pedersen, T. B. Numerical stability of time-dependent coupled-cluster methods for many-electron dynamics in intense laser pulses. *The Journal of Chemical Physics* **152,** 071102. doi:10.1063/1.5142276 (2020).

71. Dunning, T. H. Gaussian basis sets for use in correlated molecular calculations. I. The atoms boron through neon and hydrogen. *The Journal of Chemical Physics* **90,** 1007–1023. doi:10.1063/1.456153 (1989).

72. Sun, Q., Berkelbach, T. C., Blunt, N. S., Booth, G. H., Guo, S., Li, Z., Liu, J., McClain, J. D., Sayfutyarova, E. R., Sharma, S., Wouters, S. & Chan, G. K.-L. PySCF: the Python-based simulations of chemistry framework. *WIREs Computational Molecular Science* **8,** e1340. doi:10.1002/wcms.1340 (2018).

73. Aidas, K., Angeli, C., Bak, K. L., Bakken, V., Bast, R., Boman, L., Christiansen, O., Cimiraglia, R., Coriani, S., Dahle, P., Dalskov, E. K., Ekström, U., Enevoldsen, T., Eriksen, J. J., Ettenhuber, P., Fernández, B., Ferrighi, L., Fliegl, H., Frediani, L., Hald, K., Halkier, A., Hättig, C., Heiberg, H., Helgaker, T., Hennum, A. C., Hettema, H., Hjertenæs, E., Høst, S., Høyvik, I.-M., Iozzi, M. F., Jansík, B., Jensen, H. J. A., Jonsson, D., Jørgensen, P., Kauczor, J., Kirpekar, S., Kjærgaard, T., Klopper, W., Knecht, S., Kobayashi, R., Koch, H., Kongsted, J., Krapp, A., Kristensen, K., Ligabue, A., Lutnæs, O. B., Melo, J. I., Mikkelsen, K. V., Myhre, R. H., Neiss, C., Nielsen, C. B., Norman, P., Olsen, J., Olsen, J. M. H., Osted, A., Packer, M. J., Pawlowski, F., Pedersen, T. B., Provasi, P. F., Reine, S., Rinkevicius, Z., Ruden, T. A., Ruud, K., Rybkin, V. V., Sałek, P., Samson, C. C. M., de Merás, A. S., Saue, T., Sauer, S. P. A., Schimmelpfennig, B., Sneskov, K., Steindal, A. H., Sylvester-Hvid, K. O., Taylor, P. R., Teale, A. M., Tellgren, E. I., Tew, D. P., Thorvaldsen, A. J., Thøgersen, L., Vahtras, O., Watson, M. A., Wilson, D. J. D., Ziolkowski, M. & Ågren, H. The Dalton quantum chemistry program system. *WIREs Computational Molecular Science* **4,** 269–284. doi:10.1002/wcms.1172 (2014).